Coherent state of a chain of Josephson tunnel junctions

A. V. Arzumanov, V. K. Kornev, G. A. Ovsyannikov, and A. D. Mashtakov

M. V. Lomonosov State University, Moscow; Institute of Radio Engineering and Electronics, Russian Academy of Sciences, Moscow
(Submitted December 22, 1997)
Pis'ma Zh. Tekh. Fiz. **24**, 1–7 (August 12, 1998)

The regions of stability of coherent Josephson oscillation in a chain of Josephson tunnel junctions with nonlocal electrodynamic coupling were studied by means of a numerical simulation of the dynamics of this structure using the Wertheimer macroscopic theory of Josephson junctions. The possibility of using these systems to develop generators of narrow-band electromagnetic radiation at frequencies of 1 THz is discussed. © *1998 American Institute of Physics.* [S1063-7850(98)00108-6]

INTRODUCTION

The use of synchronous multi-element Josephson structures instead of single Josephson elements offers great promise for the development of phased generators of narrow-band electromagnetic radiation in the submillimeter and near-infrared wavelength ranges.

Two main requirements can now be formulated for promising types of Josephson multi-element synchronous structures from the practical viewpoint: a) strong interaction between the Josephson elements which would ensure maximum stability of the coherent state over any spread of element parameters, and b) high-frequency coherent oscillations (of order 1 THz or higher). Theoretical analyses of multi-element Josephson structures are extremely involved, so analytic estimates have been obtained for single cells of these structures only in the limit of weak electrodynamic coupling between Josephson elements and in the absence of any intrinsic capacitance.[1] However, various numerical calculations[2] have indicated that if the Josephson elements have a finite intrinsic capacitance, where the McCumber parameter $\beta \equiv (2e/\hbar) I_c R_N^2 C$ has values close to 1 (I_C is the critical current, R_N is the normal-state resistance, and C is the capacitance), stronger interaction takes place between these elements. Rejecting these data, the authors of Ref. 3 analyzed cells with strong electrodynamic coupling between Josephson elements with $\beta \sim 1$ by means of a numerical simulation of their dynamics using an extremely simple resistive model of the Josephson elements. A subsequent, more detailed study of these structures revealed that in chains with nonlocal electrodynamic coupling between the Josephson elements (Fig. 1) stronger interaction may take place at displacement currents $I < I_C$ (return branch of the hysteresis part of the current–voltage characteristic) for values of the McCumber parameter $\beta \sim 10$. These conditions can be achieved in nonshunted niobium Josephson tunnel elements with a critical current density $j_c \approx 3-5$ kA/cm^2 for which the area of the Josephson junction is $S \approx 10\ \mu$m^2. This motivated us to make a numerical simulation of the dynamics of a similar chain of Josephson tunnel elements using a more accurate model based on the Wertheimer theory.[4] The results of an investigation of the stability of the coherent Josephson oscillation in this type of one-dimensional structure are presented here.

REGION OF STABILITY OF THE COHERENT STATE

Analytic results obtained for weak electrodynamic coupling between Josephson elements in the cell of a one-dimensional structure indicate that in-phase oscillation occurs only when the imaginary part of the conductance Y of the coupling circuit is inductive and the region of stability of the coherent state with respect to differences in the critical currents is proportional to Im Y at the oscillation frequency.[1] In cases of strong coupling, i.e., when the impedance of the electrodynamic coupling circuit is low, the impedance of the Josephson element itself must also be taken into account. Thus, numerical simulations of the dynamics of this one-dimensional structure showed that the maximum region of

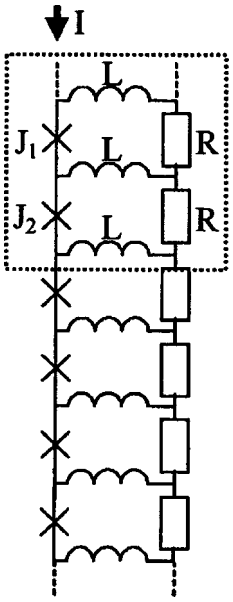

FIG. 1. Series chain of Josephson tunnel elements with an *RL* nonlocal electrodynamic coupling circuit. The dotted line encloses a single cell of the structure.

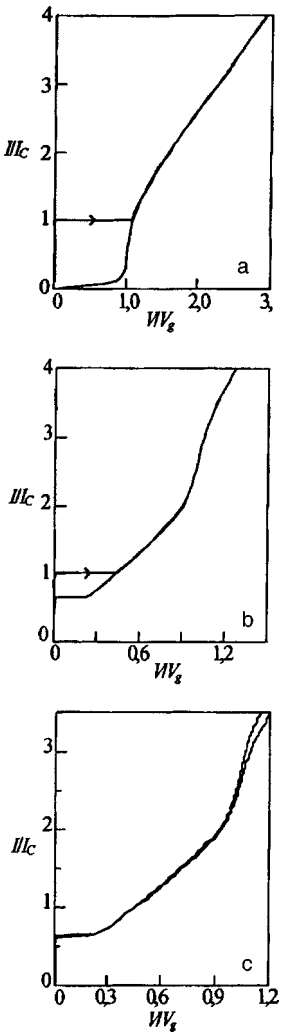

FIG. 2. Current–voltage characteristics of a single tunnel element (a), a tunnel element shunted by an RL circuit with $r=0.7$, $l=0.5$ (b), and of elements in a single cell of a chain with $r=0.7$, $l=0.5$ and the critical current difference $\Delta I_c=30\%$ (c). The voltage V is normalized to the gap voltage V_g.

stability of the coherent state for a finite impedance of the coupling circuit comparable with the impedance of the Josephson element occurs for $r\equiv R/R_N\approx 0.7$, $l\equiv L/L_j\approx 0.5$, where $L_j=[(2e/\hbar)I_C]^{-1}$ is the characteristic inductance of the Josephson junction.[3] In this case, the Josephson elements undergo fairly strong frequency-dependent shunting by the circuit impedance $z_s\equiv ZR_N=r+j\omega l$, where ω is the frequency Ω normalized to the characteristic frequency of the Josephson junction $\Omega_c=(2e/\hbar)I_CR_N$, and this shows up most clearly at dc current (see the current–voltage characteristics of the Josephson elements in Fig. 2).

The regions of existence of coherent Josephson oscillation in a single cell formed by two Josephson elements as a function of ω and $\Delta i_C\equiv(I_{C1}-I_{C2})/(I_{C1}+I_{C2})$ are shown in Fig. 3 for $\beta=10$ and various parameters of the coupling circuit r and t. The coherent state shows maximum stability against the spread of critical currents between the Josephson elements in the plasma frequency range $\omega_p\equiv\beta^{1/2}\approx 0.3$. In this range, even for large differences Δi_C, the interaction of the Josephson junctions is characterized by large-amplitude

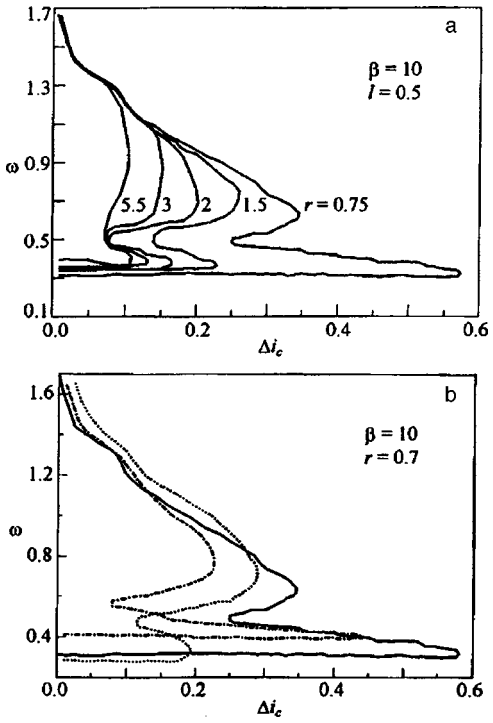

FIG. 3. Regions of existence of coherent states in a single cell of this one-dimensional structure for fixed values of l and β and various values of r (a), and also for fixed r and β and various l (b), where the dashed curve corresponds to $l=0.1$, the solid curve to $l=0.5$, and the dot-dash curve to $l=4$.

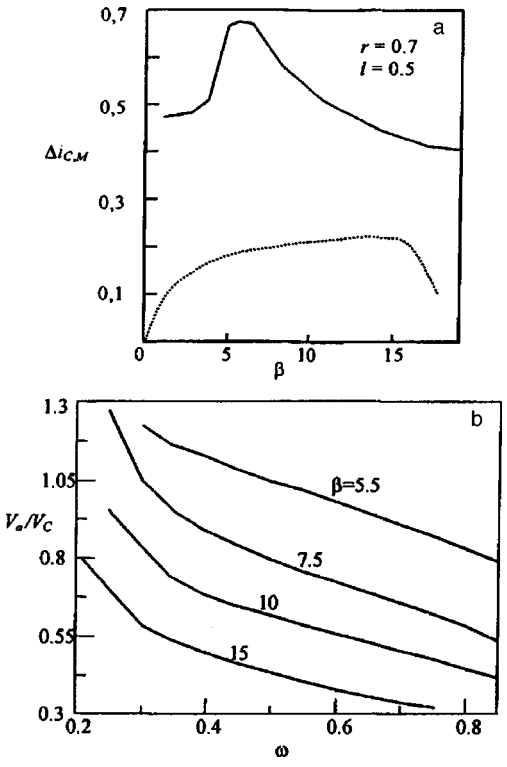

FIG. 4. a — Maximum permissible difference in the critical currents of the Josephson elements $\Delta i_c\equiv(I_{C1}-I_{C2})/(I_{C1}+I_{C2})$ for the coherent state of a two-junction cell as a function of the parameter β for $r=0.7$ and $l=0.5$, calculated using the Wertheimer model (solid curve) and the resistive model (dashed curve); b — amplitude of the cell voltage oscillations as a function of frequency for $r=0.7$, $l=0.5$, and various values of the parameter β.

currents through the outermost inductances of the coupling circuit and a relatively small-amplitude current through the central inductance. For the chain as a whole, this situation corresponds to nonlocal interaction between the Josephson elements. At higher frequencies, local interaction between the Josephson elements predominates, this being characterized by a substantially larger-amplitude current through the central inductance for the same values of Δi_C. In this range, the coherent state exhibits maximum stability to the critical current spread at oscillation frequencies $\omega \approx 2-3\omega_p$.

In the resistive model the dependence of the maximum permissible critical current difference Δi_C of the Josephson junctions in a cell on the McCumber parameter has a gently sloping maximum at $\beta \approx 5-16$. The microscopic Wertheimer model gives a narrower extremum at $\beta \approx 5-7$ (Fig. 4a). Although for $\beta > 10-15$ the difference Δi_C may be some tens of percent in this last case, the amplitude of the synchronous oscillation within the region of synchronization decreases rapidly with increasing β and oscillation frequency ω (Fig. 4b). It should also be noted that the phase difference of the Josephson oscillation within the synchronization range depends on Δi_C and varies between 0 for $\Delta i_C = 0$ and $\pi/3$ at the boundary of this range. In this case, the amplitude summation factor varies between 1 and 0.5.

The fabrication technology for niobium Josephson tunnel functions has now reached the stage where we can produce junctions with $\beta \approx 6-10$ ($S \approx 10\ \mu m^2$) with a technological spread of critical currents and critical current density $j_C \approx 3-5$ A/cm^2 ($V_C \approx 0.5-1$ mV) within a single substrate in a fairly narrow range $\Delta I_C \approx 6-10\%$ (Ref. 5). It is thus quite realistic to use this type of one-dimensional Josephson structure to develop a generator of narrow-band electromagnetic radiation tunable by a factor of three or four at frequencies up to 1 THz.

This work was partly financed under the State Program ''Topical Trends in the Physics of Condensed Media'' (Project No. 98051) and the ''Integration'' Scientific-Educational Center (Project No. 461).

[1] A. K. Jain, K. K. Likharev, J. E. Lukens, and J. E. Sauvageau, Phys. Rep. **109**, 309 (1984).
[2] H.-G. Meyer and W. Krech, J. Appl. Phys. **68**, 2868 (1990).
[3] A. D. Mashtakova, V. K. Kornev, and G. A. Ovsyannikov, Radiotekh. Elektron. **40**, 1735 (1995).
[4] K. K. Likharev, *Dynamics of Josephson Junctions and Circuits* (Gordon and Breach, New York, 1986; Nauka, Moscow, 1985).
[5] S. Han, A. H. Worsham, and J. E. Lukens, IEEE Trans. Appl. Supercond. **3**, 2489 (1993).

Translated by R. M. Durham

Modeling of the kinetics of plastic deformation of polycrystals using Markov chains

V. V. Ostashev and O. D. Shevchenko

Pskov Polytechnic Institute
(Submitted January 23, 1998)
Pis'ma Zh. Tekh. Fiz. **24**, 8–11 (August 12, 1998)

Discrete Markov chains are used to model the kinetics of microplastic deformations in polycrystalline copper as a multilevel hierarchical process. The quantitative contribution of each structural level to the average deformation is determined. © *1998 American Institute of Physics.* [S1063-7850(98)00208-0]

The present paper develops the concepts of polycrystal deformation processes using a statistical multilevel interpretation. The deformable material being studied (MO copper) is considered as a multilevel hierarchical system.[1] The task of the investigations is as follows:

— to determine the boundaries of the ranges of work of the material on the structural level being analyzed;
— to determine the quantitative contribution of each structural level to the average deformation;
— establish a correlation between the statistical and physical models.

Following the procedure used in Ref. 2, the microplastic deformations over the length X (translational ε_{xx}, γ_{xy}, and rotational ω_z) may be described as a function of the average macroscopic deformation of the sample e_j by certain random functions $f_{i,j}(x/e_j)$; $i=1,2,3$ and analyzed on three structural levels:

$i=2$ — cooperative processes at the level of an ensemble of grains;
$i=3$ — intergranular plastic deformations;
$i=4$ — intragranular plastic deformations.

The index 1 denotes the structural level associated with the evolution of the average macroscopic deformation of the sample as a whole.

The idea of describing the kinetics of plastic deformations in terms of Markov processes is based on the assumption that the microplastic deformation increments at each structural level are statistically independent. An investigation of the autocorrelation functions for ε_{xx}, γ_{xy}, and ω_z confirms that the process is Markovian to varying degrees.[2]

In accordance with the classification of Markov chains, the state of the material at level 1 can be defined as absorbing, while that at levels 2, 3, and 4 is defined as self-avoiding.[3] The work of the material during the deformation process may be described by a Markov chain with four states and is represented by a signal graph of the states (see Fig. 1).

The transition matrix for the four-state model is given by:

$$\mathbf{P}=\left(\begin{array}{c|ccc} 1 & 0 & 0 & 0 \\ \hline P_{21} & P_{22} & 0 & 0 \\ P_{31} & P_{32} & P_{33} & 0 \\ P_{41} & P_{42} & P_{43} & P_{44} \end{array}\right),$$

where we have $P_{11}=1$, $P_{12}=P_{13}=P_{14}=0$, $P_{23}=P_{24}=P_{34}=0$ from the definition of the self-avoiding and absorbing states.[3]

We give the transition matrix in the canonical form

$$\mathbf{P}=\begin{pmatrix} I & 0 \\ R & Q \end{pmatrix}.$$

The submatrix Q describes the behavior of the material in a set of self-avoiding states. The submatrix R only includes elements characterizing the transition from self-avoiding states to the absorbing state. The variation of the elements of the submatrix Q as a function of the conditions of a factor experiment allows us to determine the characteristics of the absorbing chain directly in terms of the fundamental matrix:[3]

$$N=(I-Q)^{-1}.$$

Each element of the fundamental matrix implies an average number of times the process reaches a given self-avoiding state, and the sum of the values along the rows

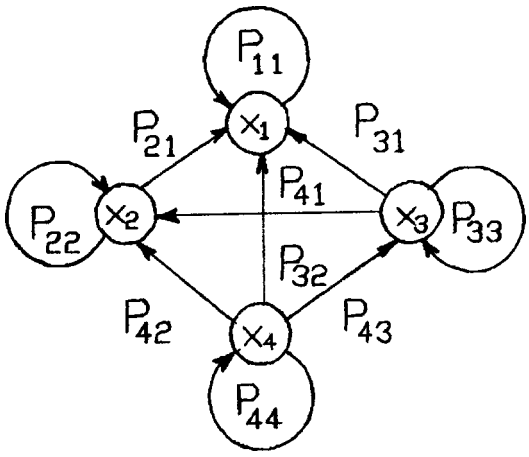

FIG. 1. Signal graph of states of a deformed polycrystalline material.

TABLE I.

Deformation	Matrix N			Σ_i
	1.154	0	0	1.154
0.073	0.588	1.063	0	1.651
	0.425	0.049	1.01	1.475
	1.266	0	0	1.266
0.054	0.202	1.016	0	1.218
	0.466	0.113	1.016	1.595

characterizes the entire contribution of each level to the average deformation of the material. Table I gives an example of the calculations of the fundamental matrices for a sample with maximum plasticity for the rotational and shear components.

All the samples, particularly at the stage of strong deformations, show various anomalies in the calculations of the contribution of the scale levels to the macroscopic deformation. The coefficient denoted by Σ_i may be regarded as the degree of inclusion of the physical mechanisms of plastic deformation in the appropriate modes on the different scale levels. Comparing, for example, the coefficients $1.266 > 1.218$ for the rotational modes, we can say that the rotational mechanism comes into operation at the grain group level, which agrees well with studies of superplasticity[4] where it was shown that one of the mechanisms responsible for superplasticity is a system of displacement of nonadjacent grains. The inequality $1.651 > 1.475$ of the coefficients for shear deformations suggests the preferential evolution of noncrystallographic slip embracing several grains.

[1] V. E. Panin, Yu. V. Grinyaev, V. I. Danilov, *Structural Levels of Plastic Deformation and Damage* [in Russian], Nauka, Novosibirsk (1990), 255 pp.
[2] V. V. Ostashev, and O. D. Shevchenko, Abstracts of Papers presented at the 32nd Seminar on Topical Strength Problems, St. Petersburg, 1996 [in Russian], pp. 35–36.
[3] J. G. Kemeny and J. L. Snell, *Finite Markov Chains* (Van Nostrand, Princeton, N.J., 1960, reprinted Springer-Verlag, New York, 1976; Nauka, Moscow, 1970, 346 pp).
[4] O. A. Kaĭbyshev, *Plasticity and Superplasticity of Metals* [in Russian], Metallurgiya, Moscow (1975), 279 pp.

Translated by R. M. Durham

Phase synchronization of switching processes in stochastic bistable systems

A. N. Sil'chenko, A. B. Neĭman, and V. S. Anishchenko

N. G. Chernyshevskiĭ State University, Saratov
(Submitted January 8, 1998)
Pis'ma Zh. Tekh. Fiz. **24**, 12–19 (August 12, 1998)

The concept of an analytic signal is used to show that the stochastic synchronization of bistable systems corresponds to locking of the instantaneous phase of the oscillations in complete agreement with the classical theory of phase synchronization. © *1998 American Institute of Physics.* [S1063-7850(98)00308-5]

The fundamental phenomenon of forced and mutual synchronization of self-oscillatory systems[1] was observed quite recently and has been studied in systems with deterministic chaos[2,3,9] and time-scale-controlled noise.[4–8] If the phase space of a chaotic system has a direction in which one of the Lyapunov exponents is zero, the concept of instantaneous phase[9] can be introduced and the frequency locking effect can be investigated using methods of phase synchronization theory. Another class is represented by nonlinear systems which in principle cannot possess natural deterministic frequencies. Their dynamics depends strongly on the noise intensity which controls the characteristic time scales of the system.

A typical model in this class is a stochastic bistable system which describes the motion of a Brownian particle in a two-well potential. The characteristic time scale for this model is represented by the average time to escape from the potential well (the Cramers time[10]). Stochastic bistable systems perturbed by a weak periodic system have recently attracted close attention in connection with studies of the stochastic resonance effect.[11,12] The response of the system to a weak periodic perturbation is amplified substantially and reaches a maximum at an optimum noise level (in the stochastic resonance regime). In the limit of a small-amplitude periodic force, the spontaneous resonance is described using linear response theory.[13,14]

However, as the signal amplitude increases (but still remains low compared with the potential barrier), the spontaneous resonance acquires features of an external synchronization effect, which are recorded from the changes in the structure of the probability density of the residence times of the system in metastable states.[4] Moreover, the average switching frequency is locked in a wide range of noise intensity and regions of synchronization similar to Arnold tongues appear on the ''noise intensity–signal amplitude'' plane.[6] Synchronization under stochastic resonance conditions is accompanied by ordering of the output signal from the bistable system which is recorded from the decrease in the Shannon entropy.[7] In coupled stochastic bistable systems mutual synchronization of noise-induced switching processes is observed.[5,15] In this situation the system has absolutely no deterministic time scales. Unlike the classical synchronization of self-oscillatory systems having deterministic natural frequencies, global time scales, defined as moments of the distribution function, interact in stochastic synchronization.[5,8]

The aim of the present paper is to describe the synchronization of stochastic bistable systems under stochastic resonance conditions in terms of phase synchronization theory. The resulting complexity in the determination of the instantaneous phase of a stochastic signal can be overcome by using the concept of an analytic signal[16,17] which is widely used in radiophysics[18,19] and in signal processing theory.[20] This method was successfully used to study phase synchronization of chaotic systems.[9]

By an analytic signal $z(t)$ we understand the complex function $z(t)=s(t)+is_H(t)=a(t)e^{i\phi(t)}$, where the function $s_H(t)$ is the Hilbert transform of the initial signal $s(t)$: $s_H(t)=1/\pi\int_{-\infty}^{\infty}s(\tau)d\tau/(t-\tau)$ (the integral is taken in the sense of the Cauchy principal value). The instantaneous amplitude $a(t)$ and phase $\phi(t)$ of the signal $s(t)$ are uniquely determined using the expressions given above. We recall that for synchronizable noisy self-oscillatory systems, the dynamics of the phase difference $\Delta\phi$ is described by the universal stochastic differential equation

$$\Delta\dot{\phi}=\delta-\epsilon\ \sin(\Delta\phi)+\xi(t), \tag{1}$$

where the mismatch parameter δ is determined by the difference between the natural frequency of the self-excited oscillator and the frequency of the force (or the difference between the natural frequencies of the mutually synchronized oscillators), ϵ is the nonlinearity parameter, and $\xi(t)$ is the noise source.[21] This stochastic differential equation describes Brownian motion in the potential $V(\Delta\phi)=-\delta\Delta\phi-\epsilon\cos(\Delta\phi)$. In the absence of noise, synchronization occurs when $\delta<\epsilon$ holds: the phase difference tends to the fixed value $\Delta\phi_0=\arcsin(\delta\epsilon)+2\pi j$. However, when the noise is taken into account, the phase difference for $\delta<\epsilon$ will fluctuate for a long time in accordance with the motion inside the potential wells $V(\Delta\phi)$ and will occasionally jump between wells, changing abruptly by 2π (Ref. 21).

The base model to investigate stochastic resonance is an overdamped stochastic system perturbed by the periodic force:

$$\dot{x}=\alpha x-x^3+\sqrt{2D}\xi(t)+A\ \sin(\omega t), \tag{2}$$

where $\xi(t)$ is the Gaussian white noise, the parameter D determines the noise intensity, and the parameter α deter-

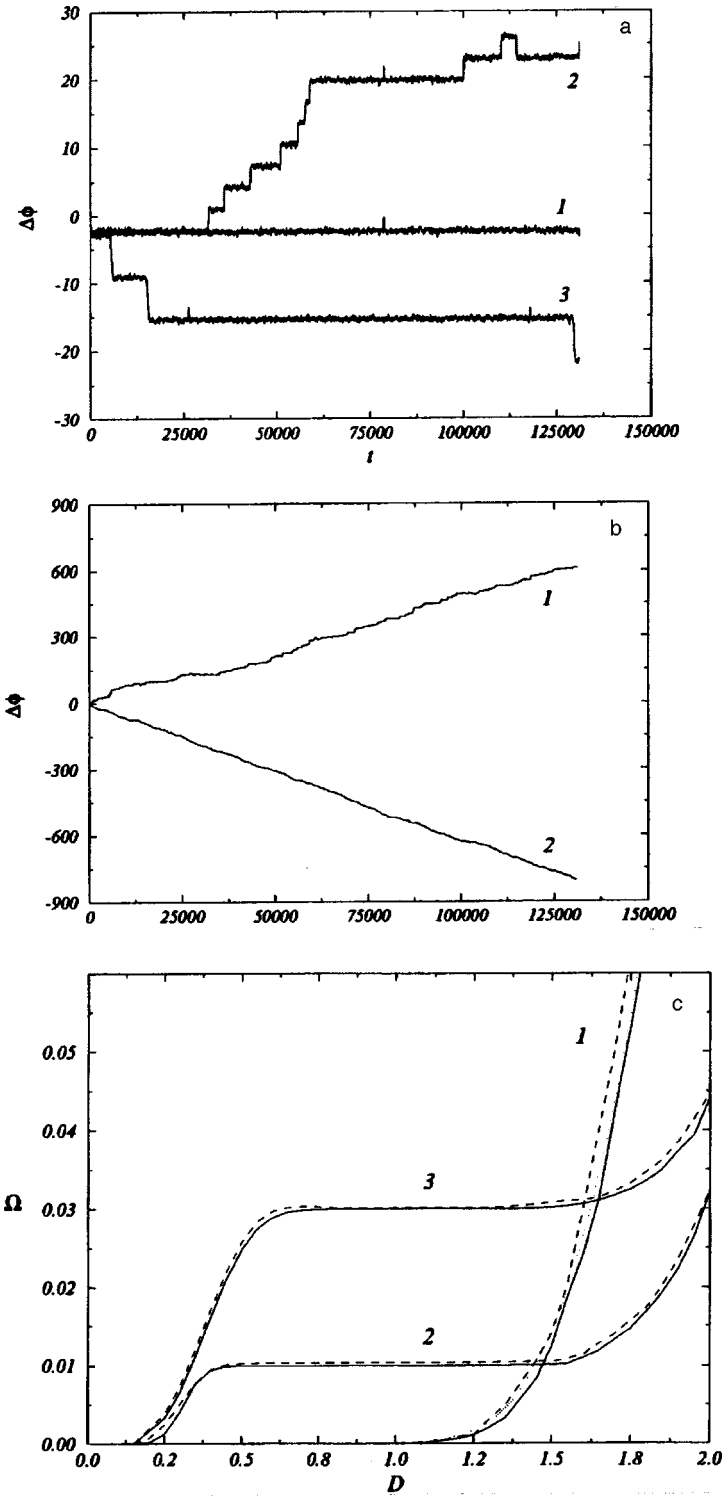

FIG. 1. a — Time dependence of the phase difference for complete (curve *1*, $D=0.9$) and partial (curves *2* and *3*, $D=1.15$ and $D=0.45$) phase synchronization of stochastic oscillations; b — time dependence of the phase difference in the absence of phase synchronization for intensities $D=0.3$ (curve *1*) and $D=1.7$ (curve *2*); c — dependence of the average frequency (solid curve) and mean switching frequency (dashed curve) on the noise intensity for $A=0$ (curve *1*), $A=4.0$, $\omega=0.01$ (curve *2*), $A=4.0$, $\omega=0.03$ (curve *3*).

mines the depth of the symmetric potential wells (in our case $\alpha=5$). In the absence of a periodic signal and with weak noise, the characteristic time scale of the system is determined by the Cramers velocity or the average frequency of departure from the metastable state:[10] $\Omega_0=(\alpha/\sqrt{2\pi})\times\exp(-\alpha^2/4D)$. In the course of a numerical simulation of the stochastic differential equation (2) calculations were made of the instantaneous phase difference of the bistable oscillator and the periodic signal $\Delta\phi(t)=\phi(t)-\omega t$, and the mean frequency $\Omega=\langle\dot{\phi}\rangle$ of the stochastic process $x(t)$ was determined. The mean switching frequency of the bistable system was also calculated.[6]

Figures 1a and 1b show the phase difference as a function of time for various noise intensities for the case $A=4.0$, $\omega=0.01$. These results demonstrate the fundamental difference between the dynamics of the phase difference for various noise intensities. Curve *1* in Fig. 1a corresponds to the case where the phases of the signal and the stochastic

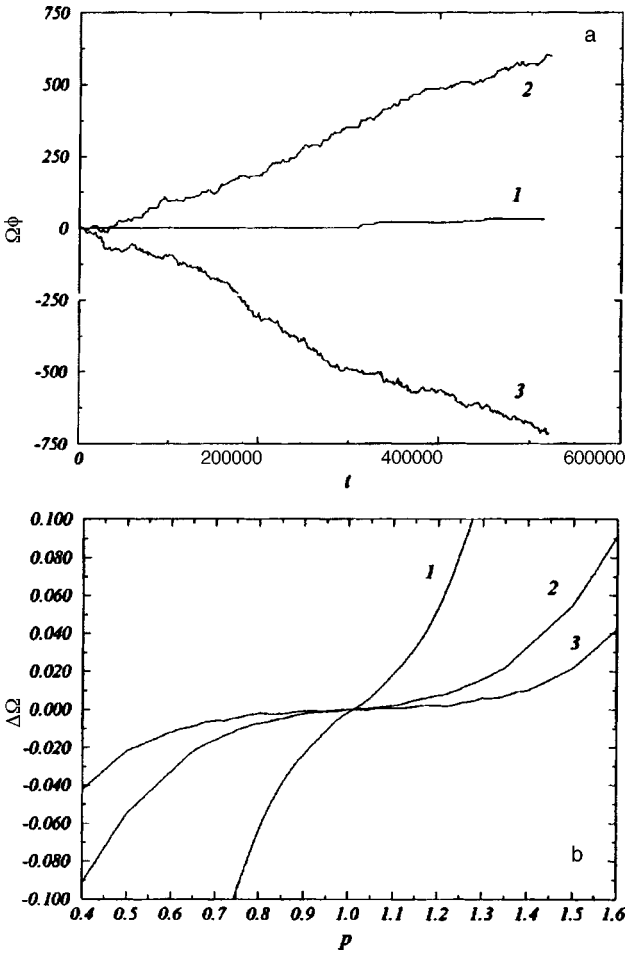

FIG. 2. a — Time dependence of the phase difference for various coupling parameters and mismatch parameters $\gamma=2.5$, $\Delta=0.96$ (curve *1*), $\gamma=1.5$, $\Delta=1.2$, $\Delta=0.8$ (curves *2* and *3*, respectively); b — dependence of the difference between the mean frequencies $\Delta\Omega$ on the mismatch parameter $p=\alpha_1/\alpha_2$ for various values of the coupling parameter between the subsystems: $\gamma=1$ (curve *1*), $\gamma=3$ (curve *2*), and $\gamma=4.2$ (curve *3*).

system are synchronized or locked: the phase difference fluctuates around a certain fixed value. In this case the mean frequency of the process $x(t)$ coincides with the signal frequency. Note that the time evolution of the phase difference may be described qualitatively using the stochastic differential equation (1). In the absence of synchronization (curves *2* and *3* in Figs. 1a and 1b), the phase difference increases without bound. Figure 1c gives the mean frequency Ω and the mean switching frequency determined neglecting the motion 4 within the well as a function of the noise intensity. It can be seen that the mean frequency Ω, determined in terms of the Hilbert transform, is almost the same as the mean switching frequency and demonstrates the locking effect, coinciding with the signal frequency in a certain range of noise intensities. The investigations showed that for the case of a weak signal when no stochastic resonance occurs, no phase synchronization and locking of the mean frequency is observed!

We shall now consider the case of mutual stochastic synchronization.[5,15] Using the base model (2), we shall analyze a system of two coupled bistable oscillators

$$\dot{y}_1 = p\alpha y_1 - y_1^3 + \gamma(y_2 - y_1) + \sqrt{2D}\xi_1(t),$$
$$\dot{y}_2 = \alpha y_2 - y_2^3 + \gamma(y_1 - y_2) + \sqrt{2D}\xi_2(t), \quad (3)$$

where ξ_1 and ξ_2 are statistically independent sources of white Gaussian noise of intensity D, p is the mismatch parameter, and γ is the coupling parameter. As the coupling parameter increases, locking of the switching frequencies is observed in the subsystems, i.e., synchronization of the switching between metastable states of the subsystem.[5] We shall show that mutual phase locking, i.e., locking of the instantaneous switching phases of the subsystems will occur in the system (3). Figure 2a gives the time dependence of the phase difference of the partial subsystems for various values of the coupling parameter and the mismatch parameter. It can be seen that two qualitatively different situations occur here: the phase difference is bounded in time when the switching processes are synchronized (curve *1*) and increases when no synchronization occurs (curves *2* and *3*). Figure 2b gives the difference between the average frequencies $\Delta\Omega=\Omega_1-\Omega_2$ as a function of the mismatch between the subsystems, confirming that a mutual stochastic synchronization effect occurs. As the coupling between the subsystems increases, regions of mismatch parameters appear for which the average frequencies of the subsystems are almost the same (curve *3*).

To conclude, these results convincingly demonstrate that external and mutual stochastic synchronization does occur in the switching of bistable systems and can be exhaustively described in terms of classical phase synchronization theory.

The authors would like to thank M. G. Rosenblum for discussions of the analytic signal method.

This work was partly supported by the Russian State Committee for Higher Education (Grant No. 95-0–8.3–66) and the Russo-German Grant DFG and RFFI 436 RUS 113/334/0(R).

[1] I. I. Blekhman, *Synchronization of Dynamic Systems* [in Russian], Nauka, Moscow (1971).
[2] V. S. Afraĭmovich, N. N. Verichev, and M. I. Rabinovich, Izv. Vyssh. Uchebn. Zaved. Radiofiz. **29**, 795 (1986).
[3] V. S. Anishchenko, T. E. Vadivasova, D. E. Postnov, and M. A. Safonova, Radiotekh. Elektron. **36**, 338 (1991).
[4] L. Gammaitoni, E. Marchesoni, and S. Santucci, Phys. Rev. Lett. **74**, 1052 (1995).
[5] A. B. Neiman, Phys. Rev. E **49**, 3484 (1994).
[6] B. V. Shulgin, A. B. Neiman, and V. S. Anishchenko, Phys. Rev. Lett. **75**, 4157 (1995).
[7] A. Neiman, B. Shulgin, V. Anishchenko, W. Ebeling, L. Schimansky-Geier, and J. Freund, Phys. Rev. Lett. **76**, 4299 (1996).
[8] V. Anishchenko and A. Neiman, in *Stochastic Dynamics*, edited by L. Schimansky-Geier and T. Pöschel (Springer-Verlag, Berlin, 1997), pp. 155–166.
[9] M. G. Rosenblum, A. S. Pikosky, and J. Kurths, Phys. Rev. Lett. **76**, 1804 (1996).
[10] P. Hänggi, P. Talkner, and M. Borkovec, Rev. Mod. Phys. **62**, 251 (1990).
[11] K. Weisenfeld and F. Moss, Nature (London) **373**, 33 (1995).
[12] A. R. Bulsara and L. Gammaitoni, Phys. Today **39**(3), 39 (1996).
[13] M. I. Dykman, P. V. E. McClintock, R. Mannella, and N. Stokes, JETP Lett. **52**, 141 (1990)].
[14] P. Lung and P. Hänggi, Phys. Rev. A **44**, 8032 (1991).
[15] A. Neiman and L. Schimansky-Geier, Phys. Lett. A **197**, 379 (1995).
[16] D. Gabor, J. Int. Elect. Eng. **93**, 429 (1946).
[17] P. Panter, *Modulation, Noise and Spectral Analysis* (McGraw-Hill, New York, 1965).

[18] S. M. Rytov, Yu. A. Kravtsov, and V. I. Tatarskiĭ, *Introduction to Statistical Radiophysics*, Vol. 1: *Random Processes*, Springer-Verlag, New York (1987); Russ. orig., Nauka, Moscow (1976).
[19] L. A. Vaĭnshteĭn and D. E. Vakman, *Frequency Separation in the Theory of Oscillations and Waves* [in Russian], Nauka, Moscow (1983).
[20] J. S. Bendat and A. G. Piersol, *Random Data: Analysis and Measurement Procedures* (Wiley, New York, 1986; Mir, Moscow 1989).
[21] R. L. Stratonovich, *Topics in the Theory of Random Noise*, Gordon and Breach, New York (1963-67); Russ. orig., Sovetskoe Radio, Moscow (1961).

Translated by R. M. Durham

Spontaneous long-wavelength interlevel emission in quantum-dot laser structures

L. E. Vorob'ev, D. A. Firsov, V. A. Shalygin, V. N. Tulupenko, Yu. M. Shernyakov, A. Yu. Egorov, A. E. Zhukov, A. R. Kovsh, P. S. Kop'ev, I. V. Kochnev, N. N. Ledentsov, M. V. Maksimov, V. M. Ustinov, and Zh. I. Alferov

St. Petersburg State Technical University
Donbass State Mechanical Engineering Academy, Kramatorsk, Ukraine
A. F. Ioffe Physicotechnical Institute, Russian Academy of Sciences, St. Petersburg
(Submitted January 6, 1998)
Pis'ma Zh. Tekh. Fiz. **24**, 20–26 (August 12, 1998)

Spontaneous emission has been observed for the first time as a result of interband transitions of holes and electrons between size-quantization levels in vertically coupled quantum dots and also as a result of transitions from quantum-well states to a quantum-dot level. The spectral range of the emission was in the far-infrared ($\lambda \cong 10-20\ \mu$m). The long-wavelength emission was only recorded simultaneously with short-wavelength interband emission ($\lambda \cong 0.94\ \mu$m) in InGaAs/AlGaAs quantum-dot laser structures at above-threshold currents.
 [S1063-7850(98)00408-X]

INTRODUCTION

Intersubband transitions of carriers in quantum wells have already been used to develop various devices such as far-infrared ($\lambda > 10\ \mu$m) detectors and modulators (Ref. 1), quantum cascade[2] and fountain[3] lasers. The development of methods of growing structures with self-organized quantum dots is opening up new possibilities for fabricating far-infrared devices. So far, however, optical interlevel transitions in quantum dots have not been studied, except for cases of photoinduced absorption of far-infrared radiation by interlevel transitions of holes and electrons in self-organized InAs/GaAs quantum dots.[4]

Here we report the first observations of spontaneous emission in InGaAs/AlGaAs quantum-dot laser structures as a result of ''level–level'' and ''quantum-well states–quantum-dot level'' transitions of holes and electrons in quantum dots. Far-infrared radiation was recorded only together with short-wavelength (near-infrared) interband emission ($h\nu \cong \varepsilon_g$, $\lambda \cong 0.94\ \mu$m) at currents near the lasing threshold ($I > I_m$). An investigation of the spontaneous emission is the first step in the development of a far-infrared laser utilizing interlevel transitions of holes (electrons) in quantum dots.

SAMPLES AND EXPERIMENTAL METHOD

The samples were laser structures with layers of vertically coupled quantum dots described in Ref. 5. The laser active region was formed by ten $Al_{0.15}Ga_{0.85}As$ layers with self-organized $In_{0.5}Ga_{0.5}As$ quantum dots. The layer thickness of 5 nm was comparable with the size (height) of the quantum dots perpendicular to the layers so that the quantum dots were vertically coupled. When the distance between the cavity mirrors was approximately 1100 μm, the threshold current density J_{th} at $T = 300$ K was approximately 290 A/cm^2 (threshold current $I_{th} \cong 0.6$ A). The lasing wavelength was around 0.94 μm.

The near-infrared stimulated emission was recorded using an FD8-K photodiode. The long-wavelength (far-infrared) emission was observed using Ge⟨Gu⟩ and Si⟨B⟩ photodetectors having an approximate range of sensitivity $\lambda = 5-29\ \mu$m at temperatures close to liquid helium temperature. The short-wavelength (near-infrared, $\lambda \cong 0.94\ \mu$m) radiation was cut out using InSb and Ge filters. The spectral range of the far-infrared radiation was determined more accurately using BaF_2, NaCl, and KBr filters. The radiation was observed in the pulsed mode with current and radiation pulse lengths of 200 ns.

RESULTS AND DISCUSSION

Figure 1 gives dependences of the photodetector signals for the near-infrared stimulated emission ($\lambda \cong 0.94\ \mu$m) and the far-infrared spontaneous emission from the quantum-dot laser structure. It was established by using the filter array that the far-infrared radiation is concentrated in the range 10–20 μm. We note that the dependence of the far-infrared spontaneous emission intensity on the laser current exhibits threshold behavior, where the threshold current is close to the threshold I_{th} for near-infrared emission. At low temperatures this threshold was 0.33 A, which is approximately half I_{th} at room temperature, and far-infrared emission can only be recorded together with near-infrared emission ($\lambda \cong 0.94\ \mu$m). Note that far-infrared emission has not been detected in similar structures without near-infrared emission.

The appearance of spontaneous emission may be explained with reference to the transition diagram in Fig. 2. Calculations[6] made for pyramidal InAs/GaAs quantum dots with a characteristic linear base dimension of 8–12 nm indicate that these have one $|000\rangle$ electron level and three $|000\rangle$, $|100\rangle$, and $|001\rangle$ hole levels. When electrons (holes) are injected into the AlGaAs layer, they are trapped for times of the order of a few picoseconds in states in the wetting layer[7,8] and then undergo a transition to an electron (hole)

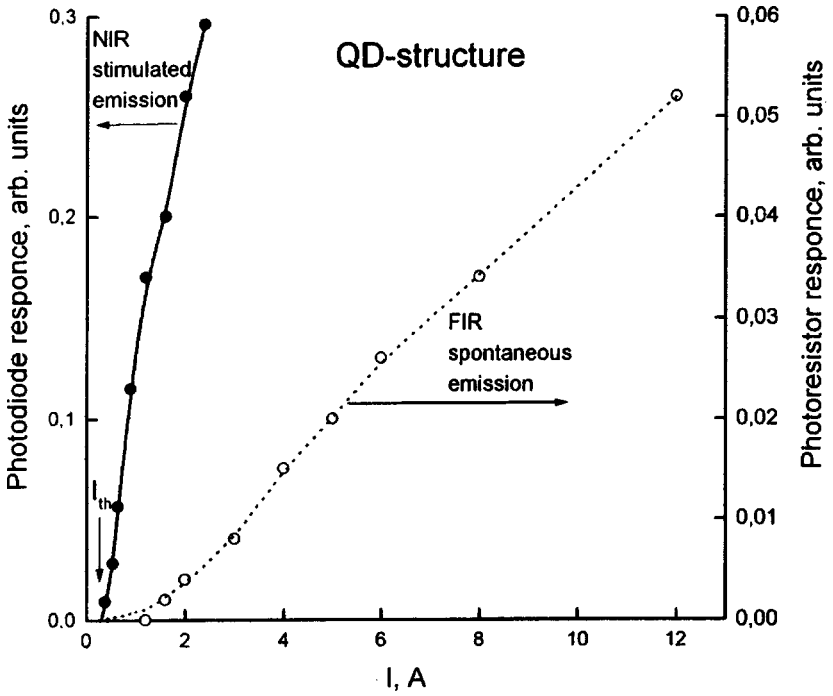

FIG. 1. Intensity of far-infrared spontaneous emission (FIR, $\lambda \cong 10-20\ \mu$m) and near-infrared stimulated emission (NIR, $\lambda = 0.92\ \mu$m) versus current through laser structure with InGaAs/AlGaAs quantum dots at the temperature $T \cong 30$ K. The near-infrared emission was recorded using an Si photodiode and the far-infrared emission using Ge⟨Cu⟩ photoresistors. The threshold current I_{th} is indicated for the near- and far-infrared emission.

level in the quantum dot. Holes may also undergo $|100\rangle \rightarrow |000\rangle$ and $|001\rightarrow|000\rangle$ interlevel transitions in the quantum dot. Transitions from upper to lower states may be accompanied by the emission of phonons[7–9] or the emission of a photon in the range 10–20 μm, or (at high carrier concentrations) they may be accompanied by Auger-type processes.[10] According to Ref. 7, the time taken for a transition between the excited and ground state of holes is approximately 40 ps (Ref. 8 gives tens of picoseconds). In Ref. 4 the optical excitation of electron–hole pairs resulted in the observation of absorption peaks for transitions between hole levels in the quantum dot in the 115 meV range and electron transitions from the quantum dot level to the continuum in the 190 meV range. The absorption of light by the holes saturated at an exciting light intensity around 100 W/cm^2 which implies that the hole levels in the InAs/GaAs quantum dot are filled. Assuming that the level pattern and processes in a system of coupled InGaAs/AlGaAs quantum dots are similar, we can predict that the levels in InGaAs/AlGaAs quantum dots are filled at the same optical intensity. At threshold currents $I_{th} \cong 0.3$ A($J_{th} \cong 140$ A/cm^2) approximately twice as many electron–hole pairs are generated compared with those generated by exciting light of intensity $J^{\nu} \cong 100$ W/cm^2. In this case, the ground states of the quantum dot are filled and holes (electrons) from excited states of the quantum dot or quantum-well states (Fig. 2) cannot undergo optical transitions to these states. Such transitions only occur under conditions where interband near-infrared radiation is generated, which partially depletes the ground states. Thus, spontaneous far-infrared emission appears, its intensity being proportional to the number of carriers in the excited states N_{ex} and the probability that the ground states are free. The number N_{ex} depends linearly on the current and the probability of filling of the lower states decreases after emission has occurred and the lower levels have been depleted by the stimulated emission. As the intensity of the near-infrared emission (or the current) increases, an increasingly large number of quantum dots of different size become involved in the emission. This is evidenced, for example, by the different differential quantum efficiency $\eta^{\nu} = dJ^{\nu}_{NIR}/dI$ at different temperatures T (η^{ν} increases as T increases from low temperatures to 300 K). For these reasons, the intensity of the far-infrared emission J^{ν}_{FIR} may increase more rapidly than linear, as is confirmed experimentally. Our results indicate that for $I > I_{th}$ we have $J^{\nu}_{FIR} \propto I^2$.

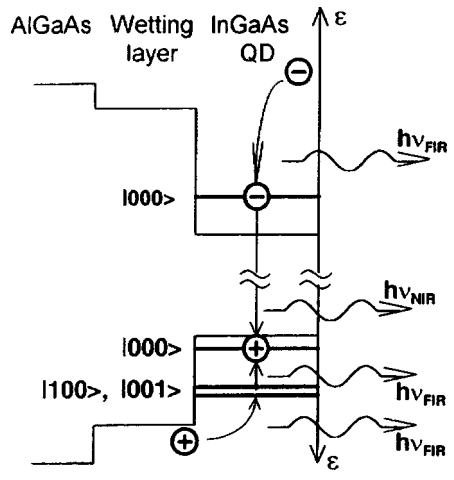

FIG. 2. Diagram of optical transitions of electrons and holes between size-quantization levels of InGaAs/AlGaAs quantum dots and between states in the AlGaAs layer and levels of the quantum dots, which lead to far-infrared spontaneous emission. The unexcited (ground) levels of the electrons and holes are depleted as a result of the induced near-infrared interband emission.

As the current through the structure increases, the dependence $J^{\nu}_{FIR}(I)$ becomes slower ($J^{\nu}_{FIR} \propto I$), possibly as a result of ejection of holes (electrons) from the upper states by

high-power stimulated emission and intensified Auger processes.[10]

We also observed far-infrared emission from quantum-well $In_{0.2}Ga_{0.8}As/GaAs$ laser structures. The threshold current for the onset of interband near-infrared emission was approximately 0.25 A. The emission was approximately an order of magnitude weaker and did not exhibit threshold behavior. Calculations made for $In_{0.2}Ga_{0.8}As/GaAs$ quantum wells of width $L_w = 7$ nm indicate that for electrons in the quantum well there are two size-quantization levels between which the energy gap is $\varepsilon_2 - \varepsilon_1 = 108$ meV, and for the holes there are three levels having the energies $\varepsilon_1(HH_1) = 12$ meV, $\varepsilon_2(HH_2) = 45$ meV, and $\varepsilon_3(LH_1) = 79$ meV. Transitions between size-quantization subbands of electrons and holes in the quantum well may also give emission in the range $\lambda = 10-20$ μm. The number of carriers in the excited states (upper subbands) is proportional to the current through the structure. The lower (ground) subbands always have unfilled states to which holes (or electrons) are transferred. Thus, the intensity of the far-infrared emission is approximately proportional to the current, $J^{\nu}_{\mathrm{FIR}} \propto I$, and has no threshold, as is observed experimentally. However, it should be noted that the carrier lifetime in quantum-well excited states given by various authors is between fractions of a picosecond and 1 ps, which is more than an order of magnitude lower than that for the quantum dot. Therefore, the intensity of the far-infrared emission for quantum-well structures should be lower than that for quantum dot structures. In fact, it was observed experimentally that J^{ν}_{FIR} is approximately an order of magnitude lower for quantum wells than for quantum dots.

To sum up, spontaneous emission has been observed for the first time as a result of carrier transitions between levels in quantum dots under conditions where interband short-wavelength emission occurs in quantum-dot laser structures. The long excited-state lifetime of electrons and holes in quantum dots (tens of picoseconds) compared with the similar lifetime for quantum wells (around 1 ps) suggests that population inversion of holes or electrons may be achieved under conditions of interband emission (where the ground levels of the quantum dot are depleted by this emission) and a far-infrared laser may be developed using interlevel carrier transitions in the quantum dot.

This work was partially supported by the Russian Fund for Fundamental Research, Grant No. 96–02–17404, INTAS-RFBR, Grant 00615i96, by the Ministry of Science and Technology, under the Program ''Physics of Solid-State Nanostructures'' Grant No. 96-1029, and also by the Federal Specific Program ''Integration,'' Grant No. 75.

[1] *Intersubband Transitions in Quantum Wells*, edited by E. Rosencher and B. Levine, NATO ASI Series, Ser. B Physics, Vol. 288 (Plenum Press. New York, 1992).
[2] J. Faist, F. Capasso, D. L. Sivco *et al.*, Science **264**, 553 (1994).
[3] O.-Lafaye Gauthier, S. Sauvage, P. Boucaud *et al.*, Appl. Phys. Lett. **70**, 3197 (1997); in *Proceedings of Symposium on ''Nanostructures: Physics and Technology,''* St. Petersburg, 1997, pp. 567–570.
[4] S. Sauvage, P. Boucaud, F. H. Julien *et al.*, Appl. Phys. Lett. **71**, 2785 (1997).
[5] M. V. Maximov, Yu. M. Shernyakov, N. N. Ledentsov *et al.*, in *Proceedings of Symposium on ''Nanostructures: Physics and Technology,''* St. Petersburg, 1997, pp. 202–205.
[6] M. Grundmann, O. Stier, and D. Bimberg, Phys. Rev. B **52**, 11 969 (1995).
[7] R. Heitz, M. Veit, N. N. Ledentsov *et al.*, Phys. Rev. B **56**, 10 435 (1997).
[8] N. N. Ledentsov, in *The Physics of Semiconductors*, Vol. 1, edited by M. Scheffler and R. Zimmermann (World Scientific, Singapore 1996), pp. 19–26.
[9] M. J. Steer, D. J. Mowbray, M. S. Skolnick *et al.*, in *The Physics of Semiconductors*, Vol. 2, edited by M. Scheffler and R. Zimmermann (World Scientific, Singapore 1996), pp. 1389–1392.
[10] J. H. H. Sandmann, G. von Plessen, J. Feldman *et al.*, Program and Abstracts of the 10th International Conference on Nonequilibrium Carrier Dynamics in Semiconductors, Berlin, 1997, Report MoD3.

Translated by R. M. Durham

Formation of optoelectronic structures based on InAsSb/InAsSbP solid solutions

E. A. Grebenshchikova, A. M. Litvak, V. V. Sherstnev, and Yu. P. Yakovlev

A. F. Ioffe Physicotechnical Institute, Russian Academy of Sciences, St. Petersburg
(Submitted January 29, 1998)
Pis'ma Zh. Tekh. Fiz. **24**, 27–33 (August 12, 1998)

An etchant having the composition $HCl/CrO_3/HF/H_2O$ is proposed for fabricating optoelectronic devices (lasers, light-emitting diodes, and photodiodes) based on InAs solid solutions for the $3-5\ \mu$m spectral range. It is shown that the proposed etchant ensures isotropic rates of etching of InAs and GaInAsSb, InAsSPbP, and InAsSb solid solutions of varying composition. An example is given of the use of this etchant to produce high-power light-emitting diodes for the $3.3\ \mu$m spectral range. © *1998 American Institute of Physics.* [S1063-7850(98)00508-4]

The last decade has seen rapid progress in the development of optoelectronic devices for the $3-5\ \mu$m spectral range using InAs solid solutions[1,2] as a result of the increased use of these devices for ecological monitoring and control of various technological processes.[3]

The properties of optoelectronic devices depend very strongly on the method of fabricating the optoelectronic element. The most widely used methods at present are chemical techniques combined with photolithography, in which a given profile is formed on the surface of the grown epitaxial structure.

The numerous publications available in the literature usually describe the formation of optoelectronics devices using chemical etchants for wide-gap solid solutions based on GaAs (Ref. 4), GaSb (Refs. 4 and 7), and InP (Ref. 4). However, the number of publications on etchants for narrow-gap InAs materials is very limited. The authors of Ref. 4 describe an etchant for the treatment of InAs consisting of nitric, hydrofluoric, and acetic acids. Disadvantages of the proposed etchant include, first, that it is impossible to treat multilayer heterostructures containing InAs and four-component solid solutions based on this, such as $Ga_xIn_{1-x}As_{1-y}Sb_y$ and $InAs_{1-x-y}Sb_yP_x$, because of the different rates of the redox reaction at the surface of layers of different composition, which leads to the formation of a stepped mesa. Second, the active release of nitrogen oxides during etching has the result that the surface is partially blocked by gas bubbles and underetched islands form at these sites, producing a rough surface.

The aim of the present study is to develop a new method of producing a smooth, polished mesa structure surface free from lateral projections, cracks, and other irregularities in order to avoid stresses at the surface of the latent mesa and reduce the surface leakage current. Such a mesastructure surface is required to achieve high quality in the subsequent stages of photolithography (application of the photoresist) and also for the deposition of dielectric coatings and the formation of Ohmic contacts.

To solve this problem, we developed an etchant for forming a mesa on the surface of an InAs optoelectronic structure which can ensure isotropic rates of etching of InAs and solid solutions based on this (GaInAsSb, InAsSbP, and InAsSb).

For the etching experiments we used *n*-type InAs [100], GaSb [100] InSb [100] and structures with GaInAsSb, InAsSbP, and InAsSb epitaxial layers of different composition. An H-383 positive photoresist was used for the photolithography. The thickness of the resistive layer was taken to be $1.5\ \mu$m. Our stated aim was satisfied by using an etchant having the composition $HCl/CrO_3/HF/H_2O$. These components are contained independently in various types of etchants.[4] However, the role of hydrochloric acid is altered in the combination of components being discussed. In all the etchants used previously, hydrochloric acid created an acidic medium. In our etchant the hydrochloric acid participates in the reaction (2) to give a strong oxidant ($2Cl^0 \rightarrow Cl_2$) which can produce a high rate of redox reactions at the surface of the semiconductor. According to chemical theory,[5] etching is considered to be a normal heterogeneous reaction and consequently, the entire etching process is divided into five stages: diffusion of the reagent toward the surface, adsorption of the reagent, surface chemical reaction, desorption of the interaction products, and diffusion of reaction products away from the surface.

Since each of the etchant reagents should undergo this sequence, the kinetics of the entire process may be very complicated. The entire process is determined by the slowest (controlling) stage. At moderate temperatures, etching is controlled by the chemical interaction stage, less frequently by the diffusion. At high temperatures, the etching kinetics is usually determined by the diffusion rate. The presence of hydrochloric acid creates conditions for the rapid oxidation of the solid solution components so that layers of a four-component solid solution having different chemical compositions can be etched at the same rate, producing a high-quality mesa. The hydrochloric acid performs two functions: it creates an acidic medium and forms an active Cl_2 oxidant (at the instant when a Cl^0 radical is released). The high oxidizing properties of the free Cl^0 radical are responsible for the high density of etching centers and can produce a polished mesa surface.

We shall analyze the redox reactions taking place in this particular etchant:[6]

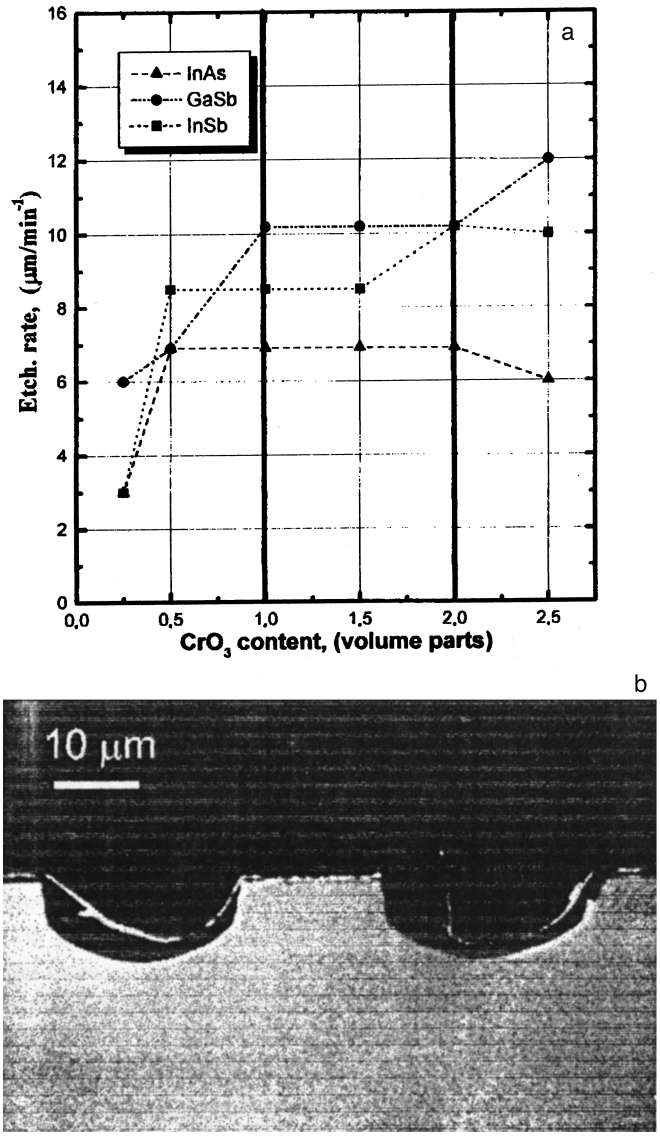

FIG. 1. a — Rate of etching of binary compounds in etchant as a function of CrO_3 content. The range of concentrations in which a polished surface can be obtained is indicated by the two vertical lines; b — photograph of a cleaved mesa section of an InAsSbP/InAsSb/InAsSbP/InAs heterostructure.

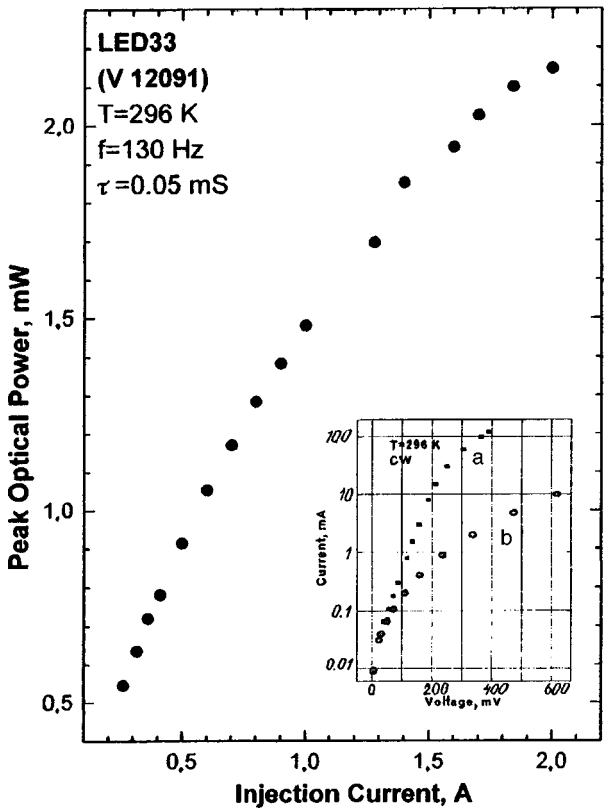

FIG. 2. Peak optical power of light-emitting diode ($\lambda = 3.3\ \mu$m) as a function of current. The inset shows the current–voltage characteristic of a forward- (a) and reverse-biased (b) diode.

$$2CrO_3 + H_2O \Leftrightarrow H_2Cr_2O_7 \Leftrightarrow 2H^+ + Cr_2O_7^{-2}, \quad (1)$$

$$H_2Cr_2O_7 + 12HCl \Leftrightarrow 2CrCl_3 + 3Cl_2 + 7H_2O. \quad (2)$$

Thus, the solution contains two strong oxidants, $Cr_2O_7^{-2}$ and Cl_2. For InAs we shall analyze the oxidation of the solid-solution components:

$$InAs + 3Cl_2 + 3H_2O \Leftrightarrow H_3AsO_3 + InCl_3 + 3HCl, \quad (3)$$

As^{-3} As^{+3} (oxidizes to oxidation state $+3$)

$$InAs + H_2Cr_2O_7 + 9HCl \Leftrightarrow H_3AsO_3 + 2CrCl_3 + InCl_3 + 4H_2O, \quad (4)$$

As^{-3} As^{+3}. An additional process is also possible, deeper oxidation to As^{+5}: AsO_3^{-3} + oxidant ($Cr_2O_7^{-2}$; Cl_2) – AsO_4^{-3}. As a result of the presence of a powerful oxidant, which results in deeper oxidation of the components, the etching rate is limited by diffusion processes rather than by redox processes, giving the same rates of etching of layers containing InAs and multicomponent solid solutions based on this: $In_{1-x}Ga_xSb_yAs_{1y}$, where $x \leqslant 0.20$, $y \leqslant 0.35$, and $InAs_{1-x-y}Sb_yP_x$, where $x \leqslant 0.32$, $y \leqslant 0.15$. Oxidation is usually accompanied by the formation of barely soluble oxides which must be converted to solution using complexing agents.[5] In this etchant, HF functions as the complexing agent.

Figure 1a gives the etching rate of binary compounds in $HCl/CrO_3/HF/H_2O$ etchant as a function of the CrO_3 content. It can be seen that the binary compounds discussed can have a polished surface when the etching rates are similar and remain almost constant. This range of etching rates between 7 and 10 μm/min is obtained with between 1 and 2 parts by volume of chromium trioxide.

Table I gives data on the etching rates of InAs solid solutions using the this etchant.

It can be seen from Table I that the etching rate of the four-component solid solutions differs little from that of InAs and is almost independent of the composition of the solid solution, as is confirmed by a photograph (Fig. 1b) obtained using an electron microscope. This suggests that this etchant can be used to obtain a smooth mesa profile and a polished surface for a structure containing layers of solid solutions of different stoichiometric composition and can thereby reduce the surface leakage currents and increase the breakdown voltage of diodes containing InAs and solid so-

TABLE I.

Composition of structure	Etching rate, μm/min
InAs	6.9
$Ga_{0.08}In_{0.92}As_{0.77}Sb_{0.23}$	6.9
$Ga_{0.12}In_{0.88}As_{81}Sb_{0.19}$	7.0
$Ga_{0.14}In_{0.8}As_{0.77}Sb_{0.23}$	7.1
$In_{1.0}As_{0.68}Sb_{0.12}P_{0.20}$	7.0

lutions based on this. A similar etchant was used to fabricate light-emitting and photodiodes (circular mesa) and lasers (mesastripes) for the $\lambda = 3-5\ \mu$m spectral range. To illustrate this structure, Fig. 2 gives the current–voltage characteristic of a light-emitting diode at room temperature and also gives the output power ($\lambda = 3.3\ \mu$m) as a function of current. These structures can be used to fabricate emitters with the highest output powers yet achieved.

To sum up, an etchant having the composition $HCl/CrO_3/HF/H_2O$ has been proposed to make structures based on InAsSb/InAsSbP solid solutions. This can etch layers of different composition at the same rate to produce a high-quality mesa and opens up possibilities for developing highly efficient light-emitting devices for the $3-5\ \mu$m spectral range containing InAs and multicomponent solid solutions based on this.

[1] Yu. P. Yakovlev, A. A. Popov, V. V. Sherstnev, A. N. Imenkov, T. N. Danilova, and O. G. Ershov, in *Proceedings of the Third European Conference on Optical Chemical Sensors and Biosensors,* Zurich, Switzerland, 1996, p. 10.
[2] A. A. Popov, M. V. Stepanov, V. V. Sherstnev, and Yu. P. Yakovlev, Pis'ma Zh. Tekh. Fiz. **23**(21), 24 (1997) [Tech. Phys. Lett. **21**, 828 (1997)].
[3] D. O. Gorelik, and L. A. Konopel'ko, *Monitoring of Atmospheric Pollution and Sources of Emission, Aero-Analytic Measurement* [in Russian], Moscow (1992), p. 289.
[4] *Compound Semiconductors*, Vol. 1, *Preparation of III-V Compounds*, edited by R. K. Willardson and H. L. Goering (Reinhold, New York, 1962; Metallurgiya, Moscow, 1967).
[5] Ya. A. Ugaĭ, *Introduction to Semiconductor Chemistry* [in Russian], Moscow (1975), p. 276.
[6] N. L. Glinka, *General Chemistry* [in Russian], Leningrad (1985), p. 635.
[7] J. Electrochem. Soc. Solid State Sci. Technol. **133**, 2565 (1986).

Translated by R. M. Durham

InAsSb light-emitting diodes for the detection of CO_2 ($\lambda = 4.3\ \mu m$)

A. A. Popov, M. V. Stepanov, V. V. Sherstnev, and Yu. P. Yakovlev

A. F. Ioffe Physicotechnical Institute, Russian Academy of Sciences, St. Petersburg
(Submitted January 15, 1998)
Pis'ma Zh. Tekh. Fiz. **24**, 34–41 (August 12, 1998)

The main characteristics of room-temperature light-emitting diodes ($\lambda = 4.3\ \mu m$) based on InAsSbP/InAsSb/InAsSbP III–V semiconductor heterostructures with a variable-gap buffer layer are reported. An optical power $P = 0.85$ mW was achieved with a pulse length of $\sim 5\ \mu s$ and 1 kHz repetition frequency. Conditions for maximizing the power of the light-emitting diodes are indicated. An example is given of the use of these diodes to detect carbon dioxide using the 4.3 μm fundamental absorption band.
[S1063-7850(98)00608-9]

Gas analyzers based on spectral methods of detection in the 4.0–4.8 μm wavelength range are attractive for the rapid analysis of CO and CO_2 content[1] in industrial and domestic applications. These analyzers may be fabricated using semiconducting light-emitting diodes (LEDs) based on InAsSb compounds as radiation sources.[2] However, the fabrication of LED structures by epitaxial methods on InAs substrates at wavelengths greater than 3.8 μm encounters specific difficulties.[3,4] This is because epitaxy cannot be used to produce layers with a lattice mismatch $\Delta a/a$ greater than 0.5%, whereas the fabrication of InAsSb layers with a band gap corresponding to emission wavelengths greater than 3.8 μm requires large lattice mismatches between the semiconductors. Although LEDs using CdHgTe semiconductors[5] can be fabricated for the 4 μm range,[5] heterostructures using III–V antimonide compounds are more attractive because of their better thermal conductivity. Such diodes have been fabricated by various methods. One approach was demonstrated in Ref. 2 where 4.2 μm LEDs were constructed using InAsSb epitaxial layers grown on a GaSb substrate. Another method involving growing an InAsSbP/InAsSb/InAsSb/InAsSbP heterostructure with a variable-gap InAsSbP emitter layer on a substrate.[4]

The present paper is a continuation of our previous studies of InAs long-wavelength light-emitting structures.[5] The aim is to report the main characteristics of InAsSbP/InAsSb/InAsSbP LEDs using an InAsSb variable-gap buffer layer and emitting in the 4.3 μm range at room temperature. It will be shown that optimizing the power supply to the LEDs can increase their optical power by more than an order of magnitude, and an example is given of the practical use of such an LED for the detection of CO_2 in the 4.3 μm spectral range.

The LEDs were formed by an InAsSbP/InAsSb/InAsSbP double heterostructure (Fig. 1a) grown by liquid-phase epitaxy on an InAs(100) substrate with a variable gap (5–8%) InAsSb buffer layer. We reported the epitaxy technology in an earlier study.[7] The intermediate layer was 4 μm thick and was doped to the substrate level. The InAsSb active region was 2 μm thick, was not specially doped, and had a natural

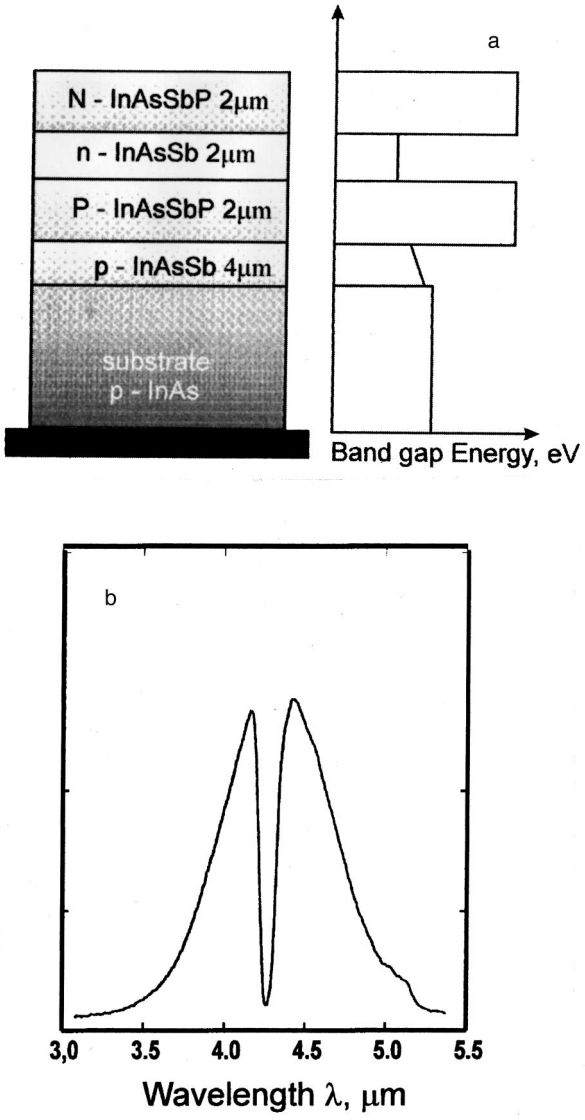

FIG. 1. a — Diagram of double heterostructure studied consisting of an InAs substrate with an InAsSb variable-gap buffer layer. Its flat band diagram is shown on the right-hand side; b — spectrum of absorption of LED radiation by carbon dioxide at atmospheric pressure recorded using a pulsed supply at room temperature. The FWHM of the emission spectrum is 0.8 μm and the injection current is 0.5 A.

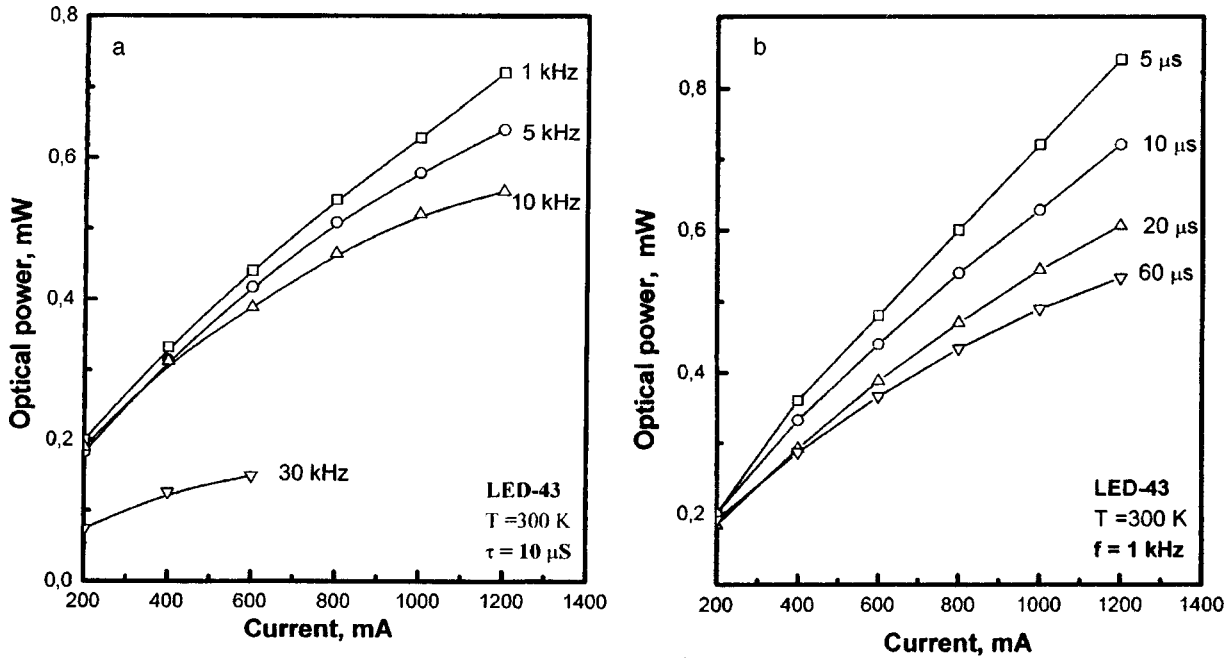

FIG. 2. Peak power of LED at room temperature as a function of repetition frequency for a fixed pulse length $\tau=10\ \mu$s (a) and as a function of pulse length at a fixed repetition frequency $f=1$ kHz (b). The highest peak power is achieved for a pulse length of less than 5 μs.

impurity concentration. The wide-gap InAsSbP confining layers were grown with a phosphorus content of 18–20% and were doped with Sn and Zn to concentrations of $(5-7)\times10^{18}$ cm^{-3} and $(1-2)\times10^{18}$ cm^{-3} for the *n*- and *p*-type layers, respectively. The antimony content in the intermediate layer and the active region was 6–8% and 12–13%, respectively. In this case, the mismatch of the intermediate layer relative to the InAs substrate was around 0.5% and that for the active region was around 0.9%.

Standard photolithography and deep chemical etching were used to form a $500\times500\ \mu$m square mesa (area $S=2.5\times10^{-3}$ cm^2) on the epitaxial structure. The LED crystal was indium soldered to a standard TO-18 case. A parabolic reflector mounted on the case was used to narrow the angular distribution of the radiation to 10–12 deg. The overall dimensions of the LED with the reflector were 9 mm in diameter and 5.5 mm in length.

The spectral characteristics of the LEDs were investigated using a synchronous detection system incorporating an MDR-12 monochromator and a cooled InAs photodiode with a pass band of up to 10 MHz. The optical power was recorded using an IMO-2M device. All the measurements were made at room temperature ($T=300$ K). The dc current supplied to the LED was limited to 200 mA. Pulses of 1.2 A amplitude and $5-50\ \mu$s length were used to supply the LEDs at high currents.

The emission spectrum of the LED contained a single emission band with a peak at $\lambda=4.3\ \mu$m at room temperature. The full width at half-maximum (FWHM) was $\sim0.8\ \mu$m. It should be noted that this value corresponds to $\sim2.5-3$ kT and is typical of the electroluminescence of InAs compounds. The position of the LED emission peak did not depend on the injection current. The spectral and energy characteristics broadly corresponded to quasi-interband recombination in the bulk of the active medium, which is consistent with the conclusions reached in previous studies.[3,4] Figure 1b shows the LED spectrum when the radiation is passed through a non-hermetically sealed monochromator. In this case, the spectrum shows a dip corresponding to the integrated absorption spectrum of a group of closely spaced CO_2 absorption lines ($\lambda\sim$ 4.23–4.29 μm). The absorption spectrum corresponds to the carbon dioxide content in the air at atmospheric pressure and a 2 m monochromator base. The presence of fairly high-intensity, closely spaced absorption lines overlapping the width of the LED spectrum means that the detection sensitivity can be enhanced by recording the sum signal.

In the quasi-cw regime, the dependence of the optical output power of the LED on the current deviated from linear (at $I\geqslant100$ mA) and tended to saturate at currents of ~200 mA ($P\sim20\ \mu$W). This was most likely attributable to the strong influence of Joule heating on the nonradiative recombination processes in narrow-gap semiconductors. Thus, the most interesting measurements were those made using a pulsed supply with a low repetition rate.

Detailed investigations were made using pulsed pumping at currents exceeding 200 mA. The maximum modulation frequency was determined by the response time of the LEDs which was estimated from the total rise and decay time of the emission when the pump current was switched. At room temperature this was around $\sim50-100$ ns. Thus, in our measurements the modulation frequency was limited to the frequency range below 10 MHz. However, this frequency band is attractive for most applications since it allows modulation at frequencies within the pass band of typical near-infrared photodetectors.

Measurements were made as a function of repetition fre-

quency and pulse length in order to investigate the current regimes giving the maximum pulse power.

Figure 2a shows the LED output power as a function of current at various pulse repetition frequencies ($f=1-30$ kHz) for a fixed pulse length ($\tau=10$ μs). At a repetition frequency of 1 kHz the output power depends almost linearly on the current up to $I=1200$ mA. With increasing repetition frequency, the dependence deviates appreciably from linear for $f\geqslant 10$ kHz and at $f=30$ kHz it begins to saturate at 600 mA (Fig. 2a).

Figure 2b gives the output power as a function of current for various pulse lengths ($\tau=5-60$ μs) at a fixed repetition frequency ($f=1$ kHz). Whereas for pulse lengths of less than 10 μs, the dependence is actually linear up to currents of 1200 mA, for longer pulses ($\tau\geqslant 20$ μs), the output power increases more slowly with current and has a lower absolute value for longer pulse lengths.

The maximum optical power was 0.8 mW at $I=1.2$ A, $\tau=5$ μs, $f=1$ kHz. It should be noted that this value exceeds the optical output power of HgCdTe LEDs, ~ 0.048 mW, for which high pump currents cannot be used because of the high series resistance ($R\sim 80$ Ω) (Ref. 6). The power achieved here is also higher than the LED power reported in Ref. 4.

To sum up, we have reported the main characteristics of LEDs using InAsSbP/InAsSb/InAsSbP semiconductor heterostructures with an emission peak at 4.3 μm. These LEDs were fabricated using a variable-gap InAsSb buffer layer which allowed us to obtain LEDs with a maximum emission wavelength of 4.3 μm on an InAs substrate. It is shown that by optimizing the power supply, the optical power of these LEDs can be increased by more than an order of magnitude. Since 4.3 μm radiation sources are promising, especially for applications in gas analysis, we have given an example of a carbon dioxide absorption spectrum recorded using these diodes.

This work was supported by the European Commission under the auspices of the INCO-Copernicus Program.

[1] L. S. Rothman, R. R. Gamache, R. H. Tipping, C. P. Rinsland, M. A. Smith, D. Chris, V. Benner, D. Malathy, J. -M. Flaud, C. Camy-Peyret, A. Goldman, S. T. Massie, L. R. Brown, and R. A. Toth, J. Quant. Spectrosc. Radiat. Transf. **48**, 469 (1992).
[2] Y. Mao and A. Krier, Opt. Mater. **6**, 55 (1996).
[3] N. P. Esina, N. V. Zotova, B. A. Matveev, N. N. Stus', and G. N. Talalakin, Pis'ma Zh. Tekh. Fiz. **9**, 391 (1983) [Sov. Tech. Phys. Lett. **9**, 167 (1983)].
[4] A. N. Baranov, A. N. Imenkov, O. P. Kapranchik, V. V. Negreskul, A. G. Chernyavskiĭ, V. V. Sherstnev, and Yu. P. Yakovlev, Pis'ma Zh. Tekh. Fiz. **16**(16), 42 (1990) [Sov. Tech. Phys. Lett. **16**, 618 (1990)].
[5] A. A. Popov, M. V. Stepanov, V. V. Sherstnev, and Yu. P. Yakovlev, Pis'ma Zh. Tekh. Fiz. **23**(21) 24 (1997) [Tech. Phys. Lett. **23**, 828 (1997)].
[6] E. Hadji, J. Bleuse, N. Magnea, and J. L. Pautrat, Appl. Phys. Lett. **67**, 2591 (1995).
[7] A. M. Litvak, M. V. Stepanov, V. V. Sherstnev, and Yu. P. Yakovlev, Zh. Prikl. Khim. **12**, 1957 (1994).

Translated by R. M. Durham

Influence of tip vibration on the probability of surface modification by a voltage pulse in a scanning tunneling microscope

G. G. Vladimirov, A. V. Drozdov, and V. D. Molchunov

Institute of Physics, St. Petersburg State University
(Submitted March 17, 1998)
Pis'ma Zh. Tekh. Fiz. **24**, 42–46 (August 12, 1998)

An investigation was made of the probability of modification of a gold surface by a voltage pulse in a scanning tunneling microscope in the presence of harmonic vibrations of the tip. The dependence of the modification probability on the pulse amplitude revealed a substantial shift of the threshold voltage and a corresponding broadening of the transition section. These results confirm the assumption that the modification probability may undergo a smooth transition from zero to maximum as a result of mechanical vibrations of the tip.
 [S1063-7850(98)00708-3]

One of the promising methods of modifying the surface in scanning tunneling microscopy (STM) involves the action of a voltage pulse on the surface. Studies have shown that in this case, the formation of inhomogeneities is a probabilistic process. The probability P becomes nonzero when the pulse amplitude exceeds a certain value U_0 after which P increases and reaches saturation when $U \geqslant U_{\text{thr}}$ holds. The value of $U_0 - U_{\text{thr}}$ is quite appreciable and may exceed 1 V.

We are of the opinion that the smooth variation of P may be caused by vibration of the tip relative to the substrate. Thus, we investigated the influence of vibration on the shape of the dependence $P(U)$.

The investigations were carried out using a conventional design of STM (Ref. 1). The method of preparing the tungsten tip and the gold film samples was the same as that used in Ref. 2. An image of the surface was obtained using a direct current of 1 nA with a bias voltage of 0.1 V between the tip and the sample. The width of the feedback pass band was ~ 5 kHz. The surface was modified by isolated 5 μs positive electrical pulses from a G5-54 generator. The feedback used to keep the current constant during imaging of the surface was not switched off. Forced vibrations produced by a G3-118 acoustic generator were supplied to the z component of a piezomanipulator. The frequency of the forced vibrations, 20 kHz, was selected so that it exceeded the feedback pass band and was not a multiple of the natural vibration frequency (~ 50 kHz) of the piezomanipulator.

It has been observed on several occasions that when a voltage pulse acts on a gold surface, hillocks of 10–20 nm diameter and 2–3 nm high are formed. Figure 1a shows the modification probability for various amplitudes of the forced vibrations of the tip. Each point on the curves was obtained from thirty modification attempts.

The existence of forced vibrations does not alter the modification probability at saturation. It can also be seen that the voltage U_0 at which P becomes nonzero varies negligibly. This behavior is evidently attributable to the fact that the average distance between the tip and the sample must be greater in the presence of vibrations. This is caused by the exponential dependence of the tunnel current on distance, so that the largest contribution to the current is made when the tip is at the minimum distance from the surface of the sample. However, a substantial shift of the threshold voltage with a corresponding broadening of the transition region are observed, this behavior becoming more pronounced as the amplitude of the tip vibrations increases.

In Refs. 3 and 4 we proposed a model of surface modification in which we assumed that the process is initiated by heating of the tip by the energy ε released by electron emission as a result of the Nottingham effect. It can be assumed that up to a certain value of ε this is balanced by the radiation and heat conduction losses of the tip. Beyond a certain critical value ε_c the apex undergoes avalanche-like heating, causing thermal expansion and reducing the tunneling gap. This increases the tunnel current and therefore causes further heating of the tip until contact is established. Quite clearly, ε_c should be uniquely related to the tunneling gap S and the voltage U between the tip and the sample. This implies that at a given voltage there must be a certain critical gap S_c. If $S < S_c$ holds at the time of application of the pulse, the surface should undergo modification. We assume that the tip undergoes harmonic vibrations about a certain average position S_0 (Fig. 2). For simplicity we shall also assume that the length of the modifying pulse is negligible compared with the period of the tip vibrations. Then the time within a single period of the vibrations during which the tip is located at distances for which surface modification may take place can be determined from the following relation:

$$t = \frac{2}{\omega} \arccos \frac{S_0 - S_c}{\Delta S},$$

where ΔS is the amplitude of the vibrations and ω is the cyclic frequency.

Under these assumptions, the modification probability has the simple form: $P = t/T$, where T is the period of the tip vibration.

Quite clearly, ε_c should be linearly related to the critical specific power released by electron emission:

$$W_c = j_c \varepsilon N / e,$$

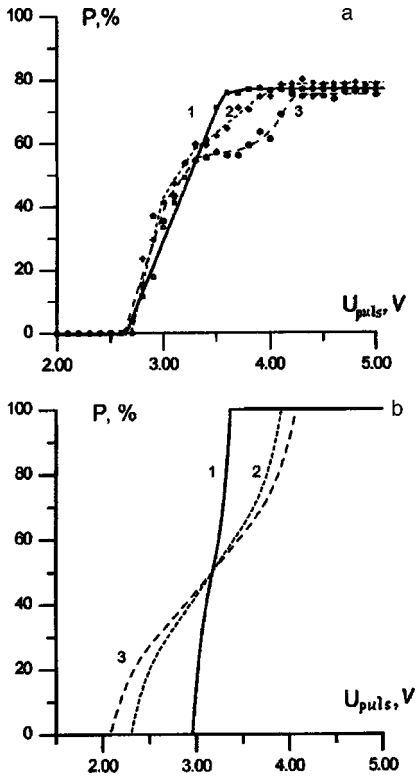

FIG. 1. Probability of the modification of a gold surface versus the strength of the modifying pulse: a — experimental curves without (*1*) and with forced vibrations of amplitude 0.03 nm (*2*) and 0.04 nm (*3*); b — theoretical curves for harmonic vibration amplitudes of 0.01 nm (*1*), 0.04 nm (*2*), and 0.05 nm (*3*).

where j is the emission current density and ε_N is the average energy released by electron emission as a result of the Nottingham effect. Since U does not exceed the work function in the range of interest, in the following calculations we used expressions obtained for a trapezoidal potential barrier.[5] In this case, we have:

$$\ln W_c = 3 \ln \frac{U}{S[\varphi^{1/2} - (\varphi - U)^{1/2}]} - A_0 \frac{S}{U}[\varphi^{3/2} - (\varphi - U)^{3/2}] + \text{const},$$

where $A_0 = 0.683\ \text{eV}^{-1/2} \cdot \text{A}^{-1}$. For this analysis the value of U_0 should correspond to $S_c = S_0 - \Delta S$ and assuming that U_0 is known, we can construct the dependences $P(U)$ having defined S_0 and ΔS. The calculated curves are plotted in Fig 1b. We feel that they show reasonable qualitative agreement with the experimental curves.

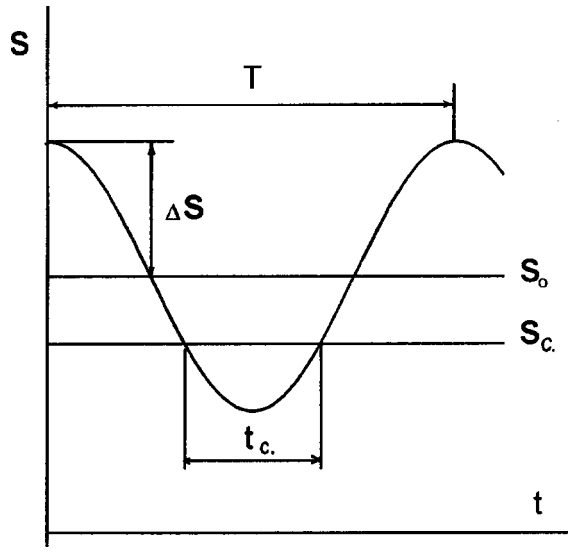

FIG. 2. Model of tip motion in the presence of harmonic vibrations.

When making such a comparison, we must bear in mind that for forced vibrations, natural unsynchronized vibrations are superposed on the vibrations induced by the external source. In addition, in our case the length of the modifying voltage pulse was not optimized, since it was only a few times smaller that the period of the natural vibrations of the tip.

Thus, these results confirm the assumption that the smooth transition of the modification probability from zero to maximum may be caused by mechanical vibrations of the tip. Consequently, neither U_0 nor U_{thr} is a true characteristic of the process, and both are strongly influenced by the technical characteristics of the equipment used.

[1] V. K. Adamchuk, A. V. Ermakov, and I. V. Lyubinetskiĭ, Prib. Tekh. Éksp. No **1**, 230 (1990).
[2] G. G. Vladimirov, A. V. Drozdov, and V. K. Dmitriev, Pis'ma Zh. Tekh. Fiz. **21**(11), 24 (1995) [Tech. Phys. Lett. **21**, 406 (1995)].
[3] G. G. Vladimirov, L. M. Baskin, and A. V. Drozdov, Pis'ma Zh. Tekh. Fiz. **21**(11), 66 (1995) [Tech. Phys. Lett. **21**, 426 (1995)].
[4] G. G. Vladimirov, L. M. Baskin, and A. V. Drozdov, Surf. Sci. **369**, 385 (1996).
[5] G. G. Vladimirov, A. V. Drozdov, and N. E. Linkov, Phys. Low-Dim. Struct. **7/8**, 127 (1996).

Translated by R. M. Durham

Influence of the parameters of a pulsed electron beam on the removal of nitrogen oxides from flue gases

G. V. Denisov, D. L. Kuznetsov, Yu. N. Novoselov, and R. M. Tkachenko

Institute of Electrophysics, Ural Branch of the Russian Academy of Sciences, Ekaterinburg
(Submitted February 23, 1998)
Pis'ma Zh. Tekh. Fiz. **24**, 47–50 (August 12, 1998)

Results are presented of an experimental investigation of the oxidation of small quantities of nitrogen oxides in air irradiated by a pulsed electron beam. It is shown that the impurity removal process is strongly influenced by the pulse length and current density of the electron beam. It is noted that an adequate model is needed to describe the plasma-chemical oxidation processes of nitrogen oxides involving charged and excited particles. © *1998 American Institute of Physics.* [S1063-7850(98)00808-8]

Toxic oxides of nitrogen (NO_x) may be removed from the flue gases of thermal power plants by ionizing these gases using electron beams or pulsed discharges.[1,2] The action of the discharge or beam electrons leads to the formation of free radicals such as O, OH, and O_2H in the ionized moist gas which react with oxides of nitrogen to form nitric acid. The addition of ammonia initiates the formation of NH_4NO_3 ammonia salts in solid powder form which can be trapped using various types of filters.[2,3] We showed in an earlier study[4] using oxides of sulfur that the use of pulsed electron beams with optimized parameters can appreciably reduce, by several factors, the energy expended in the removal of a single toxic molecule.

Here we report results of experimental investigations of the influence of the electron beam pulse length and current density on the removal of nitrogen oxides from a model mixture. The experiments were carried out using a system similar to that used in Ref. 4, which incorporated a plasma-cathode electron accelerator generating a radially diverging beam[5] and a 170 L cylindrical plasma chemical reactor. The accelerator produced an electron beam having a half-height pulse length between 32 and 90 μs, an electron energy of 280–300 keV, and a current density between 0.2×10^{-3} and 1.2×10^{-3} A/cm^2. The beam cross section at the exit from the foil was 1.44 m^{-2}.

The quantity of nitrogen oxide molecules removed in a series of pulses and also the energy deposited in the gas by the electron beam were determined experimentally. These data were used to calculate the degree of purification of the mixture η and the energy expended in the removal of a single toxic molecule ε. The values of η and ε were calculated as in Ref. 4. A model mixture containing 10% oxygen, 87% nitrogen, 3% water vapor, and 1000 ppm nitrogen oxides (1000 impurity molecules per 10^6 molecules of the main gas) was irradiated. The impurity concentrations were measured using conductometric and chromatographic methods as in Ref. 4. The measurement error was less than 1%. The electron beam energy absorbed by the gas was determined experimentally by a standard technique using film dosimeters.

Figure 1 gives results of measurements of η and ε when the mixture was irradiated by an electron beam having a current density of 0.7×10^{-3} A/cm^2 and various pulse lengths τ. Each point corresponds to a series of 300 irradiation pulses. It can be seen that an increase in the pulse length τ reduces the degree of purification and increases the energy needed to remove a single toxic molecules. The dependences of these quantities on the beam current density are similar (Fig. 2). The curves plotted in Fig. 2 were obtained for the same pulse length of 32 μs with each point corresponding to 300 irradiation pulses. The minimum energy consumption ε in these experiments was 3–4 eV per molecule and corresponded to the shortest pulse length and the lowest beam current density attainable with this experimental setup.

Various authors have investigated the oxidation of oxides of sulfur and nitrogen in ionized flue gases using cw electron beams (see, for example, Refs. 6–8). These investigations were used to develop a model of the physicochemical processes which explains the experimental results in terms of a free radical mechanism for the oxidation of NO and NO_2. Active forms of oxygen such as O and O_3 play an important role in these processes.

We used the models developed for cw electron beams to make a numerical analysis of the thirty main reactions result-

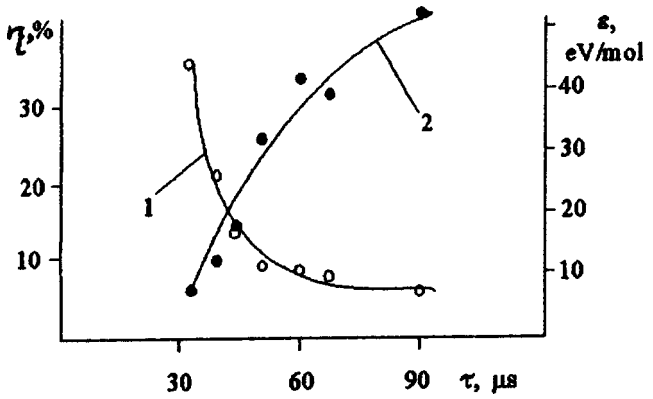

FIG. 1. Influence of electron beam duration on the degree of purification η (*1*) and the energy consumption ε (*2*).

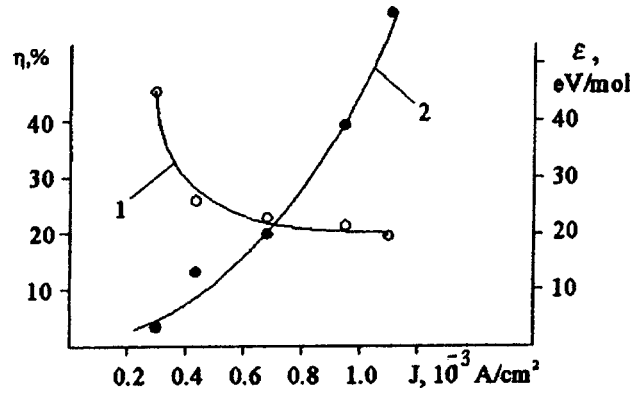

FIG. 2. Influence of electron beam current density on the degree of purification η (*1*) and the energy consumption ε (*2*).

ing in the removal of nitrogen oxides from ionized air. It was found that the existing models cannot describe our experimental results even qualitatively. In particular, the existing model indicates that an increase in the duration of the electron beam should be accompanied by an increase in the concentration of oxygen atoms and ozone molecules, which vigorously oxidize NO. Thus, an increase in the degree of purification should be observed as the pulse length increases. The opposite behavior was recorded experimentally (curve *1* in Fig. 1): an increase in the pulse length from 32 to 90 μm reduces the degree of purification from 35% to 8% for 300 irradiation pulses.

We draw attention to the fact that the degree of purification, and thus the quantity of oxidized NO molecules, responds to changes in the duration of the ionizing irradiation in the microsecond range. Typical time constants for chemical reactions involving free radicals are of the order 10^{-3}–10^{-4} s (Refs. 6–9). In our case, reactions with time constants of 10^{-6}–10^{-5} s probably play an important role, reducing the concentration of active oxidizing particles. These reactions may include ion–ion recombination reactions between negative oxygen ions which participate in the removal of nitrogen oxides, and positive O_2^+ and N_2^+ ions. The time constants of these reactions at atmospheric pressure in ionized air are microseconds and tens of microseconds.[10]

Thus, the dependence of the characteristics of the purification processes on the pulsed electron beam parameters indicates that there is a need to develop a model of the plasma-chemical processes which, unlike existing models, could adequately describe the oxidation of nitrogen oxides in pulsed ionized air by taking into account reactions between charged and excited particles.

This work as carried out as part of Project No. 271 of the International Scientific Technical Center.

[1] E. L. Neau, IEEE Trans. Plasma Sci. **22**, 2 (1994).
[2] A. A. Valuev, A. S. Kaklyugin, G. É. Norman *et al.*, Teplofiz. Vys. Temp. **28**, 995 (1990).
[3] S. Masuda, Pure Appl. Chem. **60**, 727 (1988).
[4] D. L. Kuznetsov, G. A. Mesyats, and Yu. N. Novoselov, Teplofiz. Vys. Temp. **34**, 845 (1996).
[5] A. M. Efremov, B. M. Koval'chuk, Yu. E. Kreĭndel' *et al.*, Prib. Tekh. Eksp. No. 1, 167 (1987).
[6] O. Tokunaga and N. Suzuki, Radiat. Phys. Chem. **24**, 145 (1984).
[7] J. C. Person and D. O. Ham, Radiat. Phys. Chem. **31**, 1 (1988).
[8] F. Busi, M. D'Angelantonio, O. Mulazzani, and O. Tuberini, Radiat. Phys. Chem. **31**, 101 (1988).
[9] R. Atkinson, D. L. Baulch, R. A. Cox, R. F. Hampson, J. A. Kerr, and J. Troe, J. Phys. Chem. Ref. Data **18**, 881 (1989).
[10] H. S. W. Massey, *Negative Ions* (Cambridge University Press, Cambridge, 1976; Mir, Moscow, 1979, 754 pp).

Translated by R. M. Durham

Numerical simulation of the oscillation line width in synchronous multi-element Josephson structures

V. K. Kornev and A. V. Arzumanov

M. V. Lomonosov State University, Moscow
(Submitted January 8, 1998)
Pis'ma Zh. Tekh. Fiz. **24**, 52–59 (August 12, 1998)

A method of simulating the dynamics of systems with Josephson junctions with allowance for thermal fluctuations is developed using the PSCAN program package followed by calculation of the Josephson oscillation spectrum using an autoregression method. An investigation is made of the synchronous Josephson oscillation line width in several types of Josephson structures. [S1063-7850(98)00908-2]

SIMULATION OF NOISE

A numerical simulation of the dynamics of analog and digital Josephson devices is one of the most effective methods of studying these nonlinear systems. Analyses of a whole range of problems, including studies of the Josephson oscillation line width, involve simulating processes to take account of thermal or quantum fluctuations. One of the most effective and well-known program packages for the numerical simulation of the dynamics of systems with Josephson junctions is PSCAN[1] developed in the Cryoelectronics Laboratory of the Faculty of Physics at Moscow State University. Its high efficacy is based on integrating a system of differential equations with respect to time with a variable step.

A pseudorandom number generator is required to define the fluctuating components of the current through each Josephson element when simulating the dynamics of Josephson systems. In order to obtain a white noise spectrum by accessing the generator at each integration time step, it would be necessary to minimize the step and this would substantially reduce the effectiveness of the PSCAN package. Thus, we simulated the fluctuations using a series of rectangular pulses of random amplitude and a fixed duration equal to the repetition period T and greater than the maximum variable integration step $\Delta T_{\max}$ (Fig. 1a). In this case, the noise spectrum shown by the dotted curve in Fig. 1c is approximately described by the following expression:

$$S(\Omega)=(2\pi)^{-1}\sigma^2 T\ \mathrm{sinc}^2(\pi\Omega T/\Omega_c). \tag{1}$$

Taking the period T to be fairly small, we can obtain a quasiwhite noise spectrum up to frequencies Ω exceeding the characteristic Josephson frequency $\Omega_c=(2e/\hbar)V_c$, where $V_c=I_C R_N$ is the characteristic voltage of the Josephson junction. The spectral density of this noise at low frequencies $\Omega\approx 0$ is determined by the dispersion σ^2 of the pulse amplitudes:

$$S(0)\approx\sigma^2 T/(2\pi). \tag{2}$$

Subsequently, the noise signal will be modified by replacing the series of rectangular pulses by a signal in the form of a continuous broken line (Fig. 1b) whose peaks have the same repetition period but their heights being a random quantity. This type of noise signal is preferable from the point of view of the numerical simulation techniques. The noise signal spectrum calculated numerically for $\sigma^2=4\times10^{-4}$ and $T_c=1.17$, which corresponds to the noise factor $\gamma\equiv\pi S(0)=2.3\times10^{-4}$, is shown by the solid curve in Fig. 1c. Here and subsequently we shall use the normalized time $\tau=t\Omega_c$, the normalized frequency $\omega=\Omega/\Omega_c$, the normalized current $i=I/I_c$, and the voltage $v=V/V_c$. The maximum integration step in units of $\Delta T_{\max}$ was limited to 0.1.

CALCULATION OF THE OSCILLATION SPECTRUM

As is well known, calculations of the spectrum by classical methods require a computation time proportional to $KM\log_2 M_1$, where M is the number of measurements of the

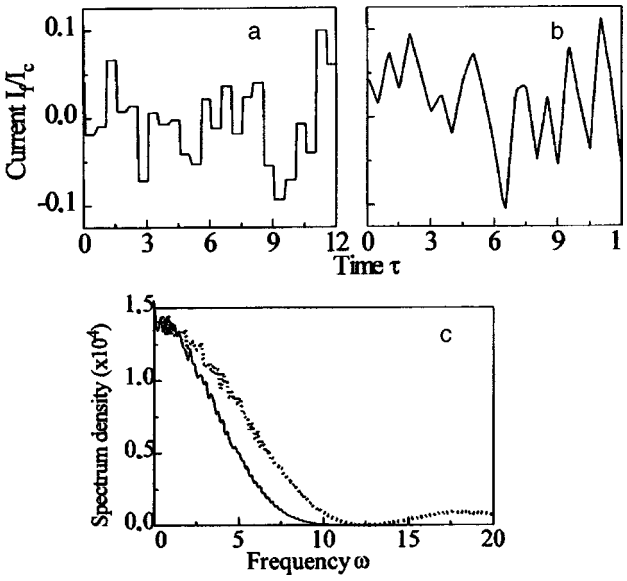

FIG. 1. Two types of current noise component (a) and (b) and their spectra (c). The dotted line gives the signal spectrum for (a) and the solid line gives that for (b).

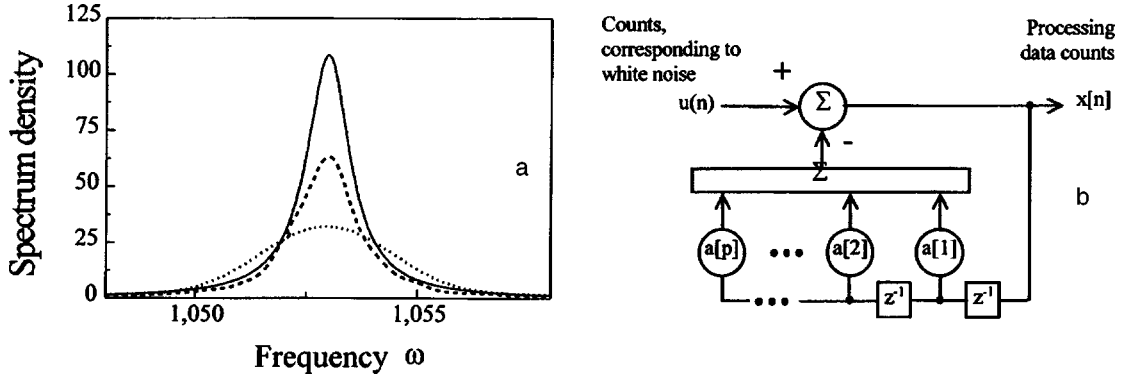

FIG. 2. a — Spectrum of Josephson oscillation $2S_u(\omega)$ for a single Josephson element (first harmonic), where the solid curve gives the real spectral oscillation line calculated using the autoregression method and the dashed and dotted curves give the results of calculating this spectral line using the classical method with $M=10^6$ measurements and $K=256$ and $K=128$ averaging intervals, respectively. The noise factor is $\gamma=2\times10^{-4}$; b — autoregression filter of order P.

signal being studied with a fixed step ΔT_{samp} within each averaging interval and M_1 is the number of these intervals. In this case, the upper limiting frequency of the calculated spectrum will be determined by the step ΔT_{samp} and the spectral resolution depends on the total number of measurements $M\sim KM_1$. Modern personal computers with 64 MB RAM can process up to $M\sim10^6$ measurements without requiring disk memory. However, this value of M is too small to resolve the Josephson oscillation line even for a uniaxial Josephson element (Fig. 2a), while synchronous multi-element structures of N Josephson junctions can demonstrate narrowing of the oscillation line proportional to N or N^2 (Ref. 2). A further increase in the number of measurements M causes a catastrophic increase in the computation time as a result of accesses to permanent memory .

Recent years have seen the development of so-called autoregression methods of spectral analysis[3] which have proved highly effective in the analysis of many types of process spectra. The high efficiency of these methods for Josephson systems allows the required spectral resolution (both for single Josephson elements and for multi-element synchronous structures) to be obtained using only $M\sim10^5$ measurements. The basic idea of these methods involves determining the parameters of a linear filter of order P which would convert white noise into the required signal (see block diagram in Fig. 2b). In this case, the combination of filter parameters can be used to calculate the spectral characteristic of the signal being analyzed and an increase in P enhances the spectral resolution.

We established that the Josephson oscillation spectrum of a single Josephson junction can be reliably calculated over a wide range of P values between $P=100$ and $P=2000$, above which ''overresolution'' of the spectral line is observed for $M=10^5$ as a result of the appearance of a nonexistent fine structure. The total time required to calculate the

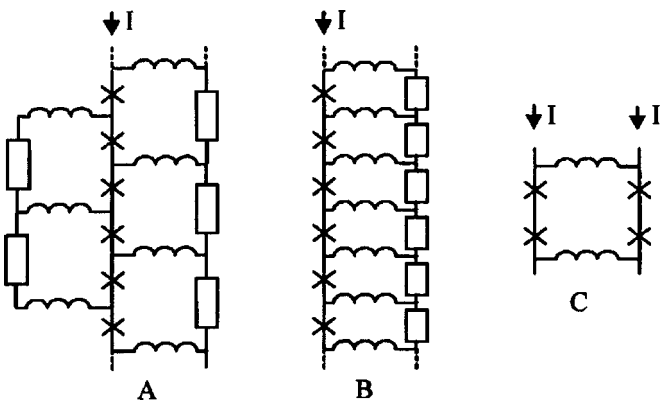

FIG. 3. One-dimensional Josephson chains ''A'' and ''B'' and single cell ''C'' of a two-dimensional Josephson structure.

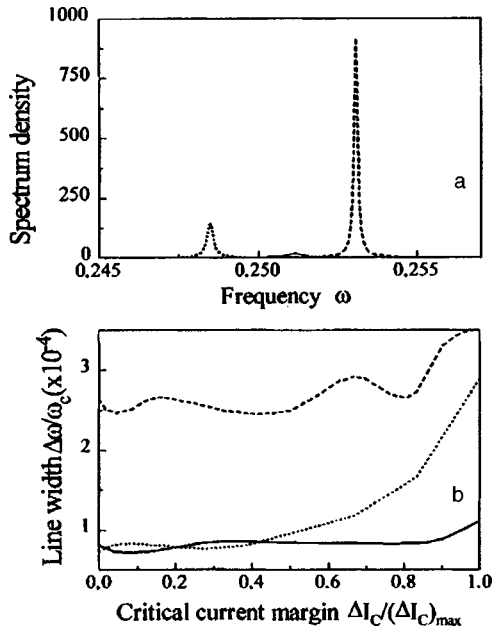

FIG. 4. a — Spectral line (first harmonic) of synchronous Josephson oscillation in chain ''B'' of N Josephson elements. The solid curve corresponds to $N=1$, dotted curve — $N=2$, and dashed curve — $N=4$. In the last two cases, the critical current of one Josephson element differed from the others by $\Delta I_c=1\%$ and the noise factor is $\gamma=2\times10^{-4}$; b — spectral line width of synchronous Josephson oscillation in a single cell of chain ''B'' (consisting of two elements) versus the critical current difference ΔI_c for two frequencies $\omega=0.3$ (dashed curve) and $\omega=0.6$ (dotted curve), and also in the single cell ''C'' for $\omega=0.9$ (solid curve).

TABLE I. Spectral line width and amplitude of spectral component A_1 for chain ''B'' of N Josephson elements.

N	1	2	4
$\Delta\omega$	6.2×10^{-4}	2.5×10^{-4}	1.4×10^{-4}
A_1	15	145	890

spectral characteristics of Josephson structures using the autoregression method is comparable with the time taken to calculate their current–voltage characteristics using the PSCAN package.

OSCILLATION LINE WIDTH IN MULTI-ELEMENT SYNCHRONOUS STRUCTURES

The methods of simulating fluctuations and calculating the spectra proposed above were used for a preliminary analysis of the Josephson oscillation line width in synchronous multi-element structures (Fig. 3) which were investigated previously neglecting the influence of thermal fluctuations.[4,5] In particular, it was shown earlier that the most promising one-dimensional structure among those studied is the ''B'' chain (Fig. 3) of Josephson tunnel junctions with a nonlocal RL electrodynamic coupling circuit. In this structure synchronous oscillation is conserved over a wide range of spreads of the critical currents I_c of the Josephson elements, which can be 50–60% for values $\beta\equiv(2e/\hbar)I_CR_N^2C\approx10$ of the McCumber parameter characterizing the intrinsic capacitance of a Josephson element and coupling circuit parameters $l\equiv(2e/\hbar)I_CL\approx0.5$ and $r\equiv R/R_N\approx0.7$ (Ref. 5).

The calculations show that the synchronous oscillation line width in this chain of N Josephson elements decreases in proportionate to N (Fig. 4a and Table I). However, a completely unexpected result was obtained for chain ''A'' (Fig. 3) with a local RL electrodynamic coupling circuit: no narrowing of the oscillation line with increasing number N isobserved in this structure (see the data presented in Table II).

TABLE II. Spectral line width and amplitude of spectral component A_1 for chain ''A'' of N Josephson elements.

N	3	4	5
$\Delta\omega$	2.1×10^{-5}	2.1×10^{-5}	2.4×10^{-5}
A_1	7960	14550	19100

TABLE III. Spectral line width and amplitude of spectral component A_1 for a single Josephson element and a four-junction interferometer (cell ''C'') with the signal taken from one arm of the interferometer and from one of the Josephson elements of this cell.

	Single	2	1
$\Delta\omega$	1.3×10^{-3}	7.5×10^{-5}	7.5×10^{-5}
A_1	105	6560	1690

Finally, for the four-junction interferometer (structure ''C'') consisting of a single cell of a two-dimensional Josephson structure,[5] the oscillation line was narrower by a factor of sixteen, i.e., N^2, than that of a single Josephson element (see Table III). Figure 4b gives the synchronous oscillation line width as a function of the difference ΔI_c between the critical currents of the Josephson elements in the two-junction cell of the linear structure ''B'' and in the four-junction interferometer. It can be seen that in the last case, the oscillation line width is almost the same within the entire synchronization range, whereas for the chain the line width increases slightly near the boundary of the synchronization region (with increasing ΔI_c and with increasing oscillation frequency).

This work was partially financed by the State Program ''Topical Trends in the Physics of Condensed Media'' (Project No. 98051) and by the ''Integration'' Educational Scientific Center (Project No. 461).

[1] S. V. Polonsky *et al.*, in Extended Abstracts of the Third International Superconductive Electronics Conference (ISEC'91), 1991, pp. 160–163.
[2] A. K. Jain, K. K. Likharev, J. E. Lukens, and J. E. Sauvageau, Phys. Rep. **109**, 309 (1984).
[3] S. L. Marple, Jr., *Digital Spectral Analysis with Applications* (Prentice-Hall, Englewood Cliffs, N. J., 1987; Mir, Moscow, 1990).
[4] A. D. Mashtakov, V. K. Kornev, and G. A. Ovsyannikov, Radiotekh. Elektron. **40**, 1735 (1995).
[5] V. K. Kornev, A. V. Arsumanov, A. D. Mashtakov, and G. A. Ovsyannikov, IEEE Trans. Appl. Supercond. **7**, 3111 (1997).

Translated by R. M. Durham

Theory of excitation of irregular waveguides

V. I. Koroza

Scientific-Research Institute of Pulse Technology, Moscow
(Submitted July 3, 1997)
Pis'ma Zh. Tekh. Fiz. **24**, 60–63 (August 12, 1998)

A variational method is proposed to study the excitation of waveguides by arbitrarily time-dependent sources, which is suitable for irregular waveguides. © *1998 American Institute of Physics.* [S1063-7850(98)01008-8]

Theories of the excitation of waveguides by monochromatic[1,2] and then by arbitrarily time-dependent[3] sources can be applied to specially shaped waveguides which allow the coordinates to be ''split'' in the direction of propagation. This limits the range of validity of these methods. Here we present equations for excitation by arbitrarily time-dependent sources which are suitable for irregular waveguides.

For the calculations we shall use the functional

$$J(\mathbf{H},\mathbf{H}_0,\mathbf{j})=\int_\Omega\left\{\varepsilon^{-1}(\mathbf{r})[\operatorname{curl}\mathbf{H}-(4\pi/c)\mathbf{j}\cdot\operatorname{curl}\mathbf{H}_0]-\frac{\mu(\mathbf{r})}{c^2}(\partial\mathbf{H}/\partial t)\cdot(\partial\mathbf{H}_0/\partial t)\right\}d\Omega, \tag{1}$$

which depends on three vector functions: the magnetic and auxiliary field strengths $\mathbf{H}(\mathbf{r},t)$ and $\mathbf{H}_0(\mathbf{r},t)$ and the current density $\mathbf{j}(\mathbf{r},t)$. Each of these is a function of four independent variables (the time t and three spatial coordinates $\mathbf{r}$). The range of integration of Ω in Eq. (1) is the interior of a segment of a four-dimensional cylinder with the interval $t_0<t<t_0+T$ as the generatrix (t_0 and T are fixed) and with the directrix being the boundary of the segment of the waveguiding system along the rectilinear Z axis ($z_0<z<z_1$), which consists of an ideally conducting lateral surface Π and two plane cross sections $S(z)$ orthogonal to the axis and intersecting it at $z=z_0(S(z_0))$ and $z=z_1(S(z_1))$.

The steady-state condition

$$\delta_{\mathbf{H}_0}J(\mathbf{H},\mathbf{H}_0,\mathbf{j})=0 \tag{2}$$

for the variation over $\mathbf{H}_0(\mathbf{r},t)$ with ''fixed ends''

$$\delta\mathbf{H}_0(\mathbf{r},t_0)=\delta\mathbf{H}_0(\mathbf{r},t_0+T)=\delta\mathbf{H}_0(\mathbf{r}|_{z=z_0},t)=\delta\mathbf{H}_0(\mathbf{r}|_{z=z_1},t)=\mathbf{0} \tag{3}$$

is equivalent to the choice of a fixed value of $\mathbf{H}(\mathbf{r},t)$ in condition (2), which within Ω satisfies the condition

$$\operatorname{curl}(\varepsilon^{-1}\operatorname{curl}\mathbf{H})+\frac{\mu}{c^2}\frac{\partial^2\mathbf{H}}{\partial t^2}=\frac{4\pi}{c}\operatorname{curl}(\varepsilon^{-1}\mathbf{j}), \tag{4}$$

and at the π surface satisfies the condition

$$\left[\left(\operatorname{curl}\mathbf{H}-\frac{4\pi}{c}\mathbf{j}\right)\cdot\mathbf{n}\right]\Big|_{\mathbf{r}\in\pi}=\mathbf{0}. \tag{5}$$

The boundary condition (5) is equivalent to the condition at the boundary of an ideal conductor correct to within the steady-state term.

Thus, determining a set of solutions of the boundary-value electrodynamics problem (4)–(5) with allowance for the nonuniqueness associated with the openness of the π surface in condition (5) and the nonuniqueness of the initial conditions reduces to the variational problem (2)–(3) for the functional (1). The nonuniqueness is eliminated by subsequently selecting the solution satisfying the necessary additional conditions from the set obtained.

We write

$$\mathbf{H}(\mathbf{r},t)=\sum\mathbf{e}_i(\mathbf{r}_\perp,z)f_i(z,t),$$

$$\mathbf{H}_0(\mathbf{r},t)=\sum\mathbf{e}_i(\mathbf{r}_\perp,z)g_i(z,t), \tag{6}$$

where $\{\mathbf{e}_i(\mathbf{r}_\perp,z)\}$ is a set of basis vector functions in the waveguide cross sections $S(z)$ with the planes perpendicular to the Z axis. Each of these functions $\mathbf{e}_i$ depends on the coordinates $\mathbf{r}_\perp$ in the cross sections $S(z)$ and on the corresponding values of z as a parameter.

After substituting expression (6) into the functional (1) as a result of condition (2) and the conditions

$$\delta g_i(z,t_0)=\delta g_i(z,t_0+T)=\delta g_i(z_0,t)=\delta g_i(z_1,t)=0,$$

corresponding to Eq. (3), we obtain a system of differential equations to determine $\{f_i(z,t)\}$, which may be written in vector form as follows:

$$\frac{\partial}{\partial z}\left[G(z)\frac{\partial\mathbf{f}}{\partial z}+Q(z)\mathbf{f}\right]-Q^{\tau}(z)\frac{\partial\mathbf{f}}{\partial z}-P(z)\mathbf{f}-T(z)\frac{\partial^2\mathbf{f}}{\partial z^2}=\frac{\partial}{\partial z}\boldsymbol{\lambda}-\boldsymbol{\rho}. \tag{7}$$

Here $G(z)$, $Q(z)$, $P(z)$, and $T(z)$ are matrix functions with the elements

$$G_{mn}=\int\int_{S(z)}\varepsilon^{-1}(\mathbf{z}\times\mathbf{e}_m)\cdot(\mathbf{z}^0\times\mathbf{e}_n)ds,$$

$$Q_{mn}=\int\int_{S(z)}\varepsilon^{-1}(\mathbf{z}^0\cdot\mathbf{e}_m\times\mathrm{curl}\mathbf{e}_n)ds,$$

$$P_{mn}=\int\limits_{S(z)}\int\varepsilon^{-1}(\mathrm{curl}\ \mathbf{e}_m\cdot\mathrm{curl}\ \mathbf{e}_n)dS,$$

$$T_{mn}=\frac{1}{c^2}\int\limits_{S(z)}\int\mu\mathbf{e}_m\cdot\mathbf{e}_n dS, \tag{8}$$

$Q^{\tau}(z)$ is the transpose of $Q(z)$; $\boldsymbol{\rho}=\boldsymbol{\rho}(z,t)$ and $\boldsymbol{\lambda}=\boldsymbol{\lambda}(z,t)$ are column vectors with the components

$$\rho_i(z,t)=\frac{4\pi}{c}\int\limits_{S(z)}\int\varepsilon^{-1}(\mathbf{r})\mathbf{j}\cdot\mathrm{curl}\ \mathrm{e}_i ds,$$

$$\lambda_i(z,t)=\frac{4\pi}{c}\int\limits_{S(z)}\int\varepsilon^{-1}(\mathbf{r})\mathbf{j}\cdot\mathbf{z}^0\times\mathbf{e}_i ds. \tag{9}$$

The dimensions of the square matrices in Eq. (7) and the columns $\mathbf{f}(z,t)=(f_1,f_2,\ldots,f_N)^{\tau}$, $\boldsymbol{\rho}(z,t)$, and $\boldsymbol{\lambda}(z,t)$ are the same, being equal to the number N of terms contained in the sums (6) (the total for each of these sums) and corresponding to the number of modes taken into account.

The vector equation (7) extends the method of coupled strings for nonsteady-state free oscillation in irregular waveguides[4] to a study of their excitation by an arbitrarily time-dependent source and corresponds to a strict electrodynamic approach. Note that numerical experiments with Eq. (7), but for free oscillations under nonsteady-state conditions[5] using finite-difference methods, reveal that high accuracy is attainable in the calculations.

Here we confine ourselves to an approximate analysis of an example of the simplest type of irregular system — a planar layer with a homogeneous medium bounded by two ideally conducting surfaces $x=0$ and $x=\Delta(z)$ (in an XYZ Cartesian system where $\Delta(z)>0$ is the layer thickness), excited by the current

$$\mathbf{j}(\mathbf{r},t)=q\mathbf{v}\delta(x-vt)\delta(z),\mathbf{v}=v\mathbf{x}^0,v>0 \tag{10}$$

using the approximation of the single-mode TEM model for which $\mathbf{e}(\mathbf{r}_{\perp},z)=\mathbf{y}^0$. The current (10) is produced by a filament moving uniformly with the linear charge density q. To determine $f(z,t)$ from the corresponding row of the vector equation (7), we have

$$\frac{\partial^2 f}{\partial z^2}+\frac{\Delta'}{\Delta}\frac{\partial f}{\partial z}-\frac{\mu\varepsilon}{c^2}\frac{\partial^2 f}{\partial t^2}$$
$$=\begin{cases}-(4\pi/c)qv\,\delta'(z), & t<\Delta(z)/v,\\ 0, & t>\Delta(z)/v.\end{cases} \tag{11}$$

In this case integration over ds in the calculations of (8) and (9) was reduced to integration over dx between the limits $[0,\Delta(z)]$. For slowly varying $\Delta(z)$ we have for the required solution (11) in the adiabatic approximation

$$f(z,t)=-\mathrm{signz}\times\frac{2\pi qv}{c\sqrt{\Delta_0\Delta(z)}}$$
$$\times\begin{cases}1, & (\sqrt{\varepsilon\mu}/c)|z|<t<(\sqrt{\varepsilon\mu/c})|z|+(\Delta_0/v),\\ 0, & t<(\sqrt{\varepsilon\mu}/c)|z|\ \text{ or }\ t>(\sqrt{\varepsilon\mu}/c)|z|+(\Delta_0/r),\end{cases}$$

which is consistent with the concept of two stepped pulses being formed in the layer, having the width $\Delta_0=\Delta(0)$ and traveling at the same velocities $C/\sqrt{\varepsilon\mu}$ but in opposite directions along the Z axis. In this case, as the pulses propagate, their amplitudes vary as $\sim[\Delta(z)]^{-1/2}$.

[1] Ya. N. Fel'd, Zh. Tekh. Fiz. **17** 1471 (1947).
[2] L. A. Vaĭnshteĭn, Zh. Tekh. Fiz. **23**, 654 (1953).
[3] V. V. Borisov, *Nonsteady-State Fields in Waveguides* [in Russian], Leningrad State University Press, Leningrad (1991), 156 pp.
[4] V. I. Koroza, Pis'ma Zh. Tekh. Fiz. **22**(21), 6 (1996) [Tech. Phys. Lett. **22**, 865 (1996)].
[5] V. I. Koroza and V. E. Kondrashov, Pis'ma Zh. Tekh. Fiz. **22**(17), 91 (1996) [Tech. Phys. Lett. **22**, 947 (1996)].

Translated by by R. M. Durham

Ultrasound-stimulated degradation–relaxation effects in gallium phosphide light-emitting *p–n* structures

A. N. Gontaruk, D. V. Korbutyak, E. V. Korbut, V. F. Machulin, Ya. M. Olikh, and V. P. Tartachnik

Institute of Semiconductor Physics, Ukraine National Academy of Sciences, Kiev
(Submitted February 10, 1998)
Pis'ma Zh. Tekh. Fiz. **24**, 64–68 (August 12, 1998)

An investigation was made of the processes taking place in gallium phosphide light-emitting diodes exposed to ultrasound treatment. It was observed that the luminescence intensity of the diodes decreases monotonically in the field of an ultrasound wave. After the action of the ultrasound has ceased, the radiative recombination intensity gradually recovers. The degradation effects occur as a result of the destructive effect of the ultrasound on bound excitons and the formation of nonequilibrium dislocation pileups at room temperature. © *1998 American Institute of Physics.* [S1063-7850(98)01108-2]

The propagation of high-intensity ultrasound in a crystal is usually accompanied by changes in the semiconductor properties, such as the photosensitivity, electrical conductivity, radiative recombination intensity, and noise characteristics.[1–4] The energy of the ultrasound wave can also be used specifically to improve the parameters of semiconductor electronics devices such as transistors, optrons, and heterojunctions.[5–7]

Here we report results of an investigation of the gradual reduction in the luminescence intensity of a gallium phosphide (GaP) light-emitting diode exposed to the action of an ultrasound wave and the subsequent monotonic increase in the brightness of the luminescence after the acoustic load has been switched off.

We used red GaP light-emitting diodes (as-prepared and after exposure to Co^{60} γ-radiation, $\Phi = 10^7 - 10^9$ rad), whose dominant emission component corresponded to recombination of an exciton bound at a Zn–O pair ($h\nu = 1.8$ eV). The ultrasound treatment was carried out at 77 and 300 K. The power of the ultrasound wave was 1 W/cm^2 at frequencies of 3–5 MHz. Measurements were made of the spectral characteristics of the luminescence brightness (in the range 600–850 μm, $T = 300$ K) and also of the oscillations of the luminescence intensity at 77 K.

It was observed that when the ultrasound is switched on, the luminescence brightness drops instantaneously by 5–10% accompanied by an increase of the current through the *p–n* junction. The nature of the changes indicates that a high-intensity ultrasound wave has a destructive influence on the exciton field in the crystal. An increase in the duration of the ultrasound treatment produces a further, slower, drop in the emission intensity (degradation of the diode) with the working current remaining constant (Fig. 1), which indicates that a different mechanism of brightness degradation is initiated (appears). If the ultrasound exposure time is not especially long (<1 h), the luminescence recovery period is comparable with the quenching time.

The application of successive degradation-recovery cycles of ultrasound treatment to a diode containing radiation-induced structural damage ($\Phi = 10^9$ rad) leads to partial recovery of the emissivity. Ultrasound treatment of a reverse-biased GaP structure whose spectrum contains mi-

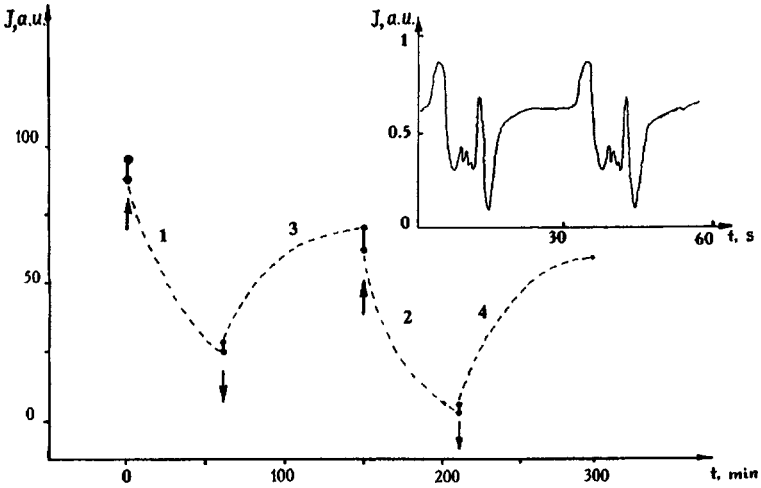

FIG. 1. Emission intensity of GaP light-emitting diode versus treatment time ($f = 4.75$ MHz, $W = 1$ W/cm^2) for two successive cycles of ultrasound treatment. Curves *1* and *2* correspond to degradation of the electroluminescence intensity; curves *3* and *4* correspond to relaxation of the emission intensity after the ultrasound has ceased. The arrows indicate the times when the ultrasound is switched on (upward arrow) and off (downward arrow). Inset: low-frequency oscillations of the luminescence at 77 K.

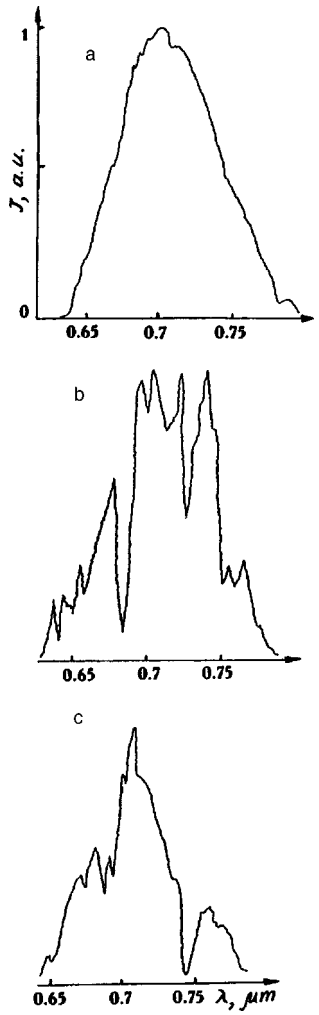

FIG. 2. Spectral distribution of the electroluminescence intensity of a GaP diode: a — emission spectrum of initial sample; b — spectrum of sample after ultrasound treatment for 6 h in operating regime (the current through the p–n junction was $I=20$ mA); c — spectrum recorded 10 min after the previous measurement.

croplasma luminescence, reduces its intensity. A significant feature of ultrasound-degraded crystals is that their luminescence is unstable over the entire spectral range: the $I(\lambda)$ curve reveals isolated narrow lines which can alter their position during a subsequent measurement (Fig. 2). These local ''flashes'' are only typical of diodes which have been subjected to a comparatively high dose of ultrasound treatment (exposure for several hours).

A possible mechanism for the evolution of these degradation–relaxation effects in this particular case may be the capture of carriers by long-lived traps.[2] However, our preliminary experiments revealed that prolonged ultrasound treatment of Hall GaP samples did not produce any significant changes in the carrier concentration. Thus, as has already been noted, the drop in the radiative recombination intensity is caused by decay of bound excitons in an ultrasound field as a result of the forced vibrations of dislocations. This effect is particularly noticeable at the instant when the ultrasound is switched on. As the ultrasound treatment continues, the dominant effect becomes the destructive influence of dislocations set in motion by the ultrasound wave and acting as powerful fields of nonradiative recombination. In a sample which has been treated with ultrasound for 30 min, the concentration of these dislocations, calculated as in Ref. 8, is close to $\rho \approx 10^7$ cm^{-2}. At such high dislocation densities, dislocation network pileups may occur, which were observed in Ref. 8 as ''dark spots'' and ''dark lines.''

In gallium phosphide at room temperature, these formations are fairly mobile, so after the ultrasonic load has been removed the degradation process is replaced by relaxation to the initial state. At low temperatures (77 K) these dislocation pileups form mobile dislocation packets moving slowly through the sample and acting as sources of current and luminescence brightness oscillations at frequencies of a few hundredths of a hertz (Fig. 1, inset).

The narrow lines resembling flickering observed on the spectral dependence of the luminescence for the ultrasound-treated crystal (Fig. 2b) are reminiscent of the acoustoluminescence flashes described in the literature.[2] At high dislocation densities the sample very likely contains unstable regions of internal mechanical stresses which are capable of acting as sources of local emission.

The ''improving'' influence of an ultrasound wave on irradiated devices and on the intensity of the microplasma luminescence is to a considerable extent attributable to the gettering action of the mobile dislocations. By acting as an effective sink for the simplest structural damage[8–10] as they move through the crystal, these dislocations can absorb both initial and irradiation-induced point defects.

It has thus been established as a result of these investigations that an acoustic wave has a destructive influence on bound excitons in GaP crystals. The influence of ultrasound treatment on gallium phosphide at room temperature leads to the formation of thermodynamic nonequilibrium pileups of dark-spot dislocations which reduce the electroluminescence intensity. The luminescence recovers within a few tens of minutes after the ultrasound treatment has ceased. During the relaxation time short-lived narrow emission lines appear in the spectrum caused by the existence of unstable zones of mechanical stresses created previously by the ultrasound treatment.

The mobile dislocations have a gettering effect on radiation-induced point defects and the decay products of complex damage.

This work was partially supported by the Ukraine Fund for Fundamental Research, Project No. 2.5.1/55.

[1] A. P. Zdebskiĭ, N. V. Mironyuk, S. S. Ostapenko *et al.*, Fiz. Tekh. Poluprovodn. **20**, 1861 (1986) [Sov. Phys. Semicond. **20**, 1167 (1986)].
[2] I. V. Ostrovskiĭ, *Acoustoluminescence and Crystal Defects* [in Russian], Vishcha Shkola, Kiev (1993), p. 223.
[3] A. P. Zdebskiĭ, M. K. Sheĭnkman, A. N. Anniyazov *et al.*, Fiz. Tverd. Tela (Leningrad) **29**, 1135 (1987) [Sov. Phys. Solid State **29**, 648 (1987)].
[4] Ya. M. Olikh and Yu. N. Shavlyuk, Fiz. Tverd. Tela (St. Petersburg) **38**, 3365 (1996) [Phys. Solid State **38**, 1835 (1996)].
[5] A. P. Zdebskiĭ, V. L. Korchnaya, T. V. Torchinskaya *et al.*, Pis'ma Zh. Tekh. Fiz. **12**(1), 76 (1986) [Sov. Tech. Phys. Lett. **12**, 31 (1986)].
[6] E. Yu. Brailovskiĭ, A. P. Zdebskiĭ, G. I. Semenova *et al.*, Pis'ma Zh. Tekh. Fiz. **13**, 1310 (1987) [Sov. Tech. Phys. Lett. **13**, 547 (1987)].

[7] E. Yu. Brailovskiĭ, *Radiation-Induced Defect Formation in Wide-Gap Semiconductors and Heterostructures Using These*, Author's Abstract of Doctoral Dissertation [in Russian], Kiev (1986), 276 pp.
[8] W. A. Brantleu, O. I. Lorimor, P. D. Dapkus *et al.*, J. Appl. Phys. **46**, 2629 (1975).
[9] V. M. Loktev and Yu. M. Khalak, Ukr. Fiz. Zh. **42**, 343 (1997).
[10] R. M. Vernidub, Ya. M. Olikh, V. P. Tartachnik *et al.*, Ukr. Fiz. Zh. **40**, 886 (1995).

Translated by R. M. Durham

Luneberg lens formed from cubes: geometric-optics calculations

A. V. Golubyatnikov and B. Z. Katsenelenbaum

Institute of Radio Engineering and Electronics, Russian Academy of Sciences, Moscow;
N. E. Bauman State Technical University, Moscow
(Submitted January 30, 1998)
Pis'ma Zh. Tekh. Fiz. **24**, 69–72 (August 12, 1998)

An analysis is made of the focusing by a spherical Luneberg lens composed of discrete dielectric cubes with different permittivities. Geometric-optics calculations are used to determine the degree of focusing of rays by a lens consisting of 2600 cubes. It is shown that the degree of focusing is considerably inferior to that obtained for a continuous distribution of ε.
 [S1063-7850(98)01208-7]

1. A Luneberg lens consists of an inhomogeneous dielectric sphere in which the permittivity ε is a function of the distance R from the center, $\varepsilon=2-R^2/a^2$ (a is the radius of the sphere). Calculations made using the geometric-optics approximation show that when a beam of parallel rays is incident on this sphere, they all converge at a single point, the focus. Here we analyze a lens with a discrete distribution of ε, formed by homogeneous cubes, in each of which ε has the value which should be found at its center. The faces of the cubes form three systems of parallel planes. A parallel beam of rays with the same amplitudes and phases is incident on the lens. The path of each ray is traced to the focal plane and three numbers are determined: the distance from the focus, the phase, and the amplitude. In these calculations the number of rays M was on the order of 10^3 and incidence of the beam in ≈ 10 directions was considered.

We take the side of a cube to be unity. The x, y, and z coordinates of the center of each cube are integers l, m, and n. The value of ε for the cube labeled (l,m,n) is $\varepsilon_{l,m,n}=2-(l^2+m^2+n^2)/p^2$ for $l^2+m^2+n^2\leqslant p^2$, and $\varepsilon_{l,m,n}=1$ for $l^2+m^2+n^2>p^2$. Here we have written $p=a-1/2$. We took that $2a=17$ and the lens contained ≈ 2600 cubes.

The direction of the beam is defined by three nonpositive numbers α_0, β_0, and γ_0 ($\alpha_0^2+\beta_0^2+\gamma_0^2=1$) which are the cosines of the angles with the x, y, and z axes. The angle μ with the z axis is the smallest, $|\gamma_0|\geqslant|\alpha_0|$, $|\gamma_0|\geqslant|\beta_0|$, and $\gamma_0=\cos\mu$. We assumed $\alpha_0=\beta_0$ almost everywhere; this constraint had no influence on the result. The angle μ varied between $\mu=0°$ ($|\gamma_0=1|$) and $\mu=55°$ ($|\gamma_{\gamma_0}|=1/\sqrt{3}$). At the entry plane $\alpha_0 x+\beta_0 y+\gamma_0 z+a=0$, the Nth ($N\leqslant M$) ray has the coordinates x_0^N, y_0^N, and z_0^N. We need to find its parameters on the focal plane $\alpha_0 x+\beta_0 y+\gamma_0 z-a=0$. In order to ensure that the ray is incident on the lens, the condition $(x_0^N)^2+(y_0^N)^2+(z_0^N)^2\leqslant 2a^2$ must be satisfied. On the x,y plane the projections of these points should form a square grid with side $d/\sqrt{|\gamma_0|}$, where d is the side of the square grid formed by the rays on the entry plane. We assumed that $d=1/2$; four rays are incident on each cube.

2. The points where the Nth ray intersects with the faces of the cubes are successively determined by an iterative method using the following scheme. We first determine the number of the cube in which the point x_0, y_0, z_0 lies (the superscript N is omitted), i.e., the integers l,m,n, such that $l-1/2<x_0<l+1/2$, $m-1/2<y_0<m+1/2$, and $n-1/2<z_0<n+1/2$. The ray equation before the next refraction has the form $x=x_0+\alpha_0 t$, $y=y_0+\beta_0 t$, $z=z_0+\gamma_0 t$, where $t\geqslant 0$. We then find the roots of the six equations (faces of the cubes) $x=l-1/2$, $x=l+1/2$, $y=m-1/2$, $y=m+1/2$, $z=n-1/2$, $z=n+1/2$, which can be solved independently together with the ray equation. The smallest positive root t of these equations gives the coordinate of the next point and this value of t, multiplied by $\sqrt{\varepsilon}$ for this particular cube, gives the optical path of the ray therein. The direction cosines $\alpha_1,\beta_1,\gamma_1$ in the next cube are obtained from three equations. One of these is obvious: $\alpha_1^2+\beta_1^2+\gamma_1^2=1$. The other two depend on the face at which refraction has taken place and the cube in which the ray is found. If, for instance, the value of t corresponds to the first of the six equations, the new cube has the number $l-1,m,n$ and the normal to the boundary has the direction cosines $(1,0,0)$. Then the second equation is $\gamma_1\beta_0-\beta_1\gamma_0=0$, and the third is $\sin\varphi_1=\sin\varphi_0\sqrt{(\varepsilon_{l,m,n})/(\varepsilon_{l-1,m,m})}$, where the angles φ_1 and φ_0 are determined (in our example) by the fact that $\cos\varphi_0=\alpha_0$ and $\alpha_1=\cos\varphi_1$. If the angle φ_0 is so large that it satisfies $|\sin\varphi_1|>1$, i.e., total internal reflection takes place, two angles are retained at this stage of the iterative process and the cosine of the third changes sign.

All the coordinates of the points of refraction obtained are successively substituted into the left-hand side of the focal plane equation. When the result first becomes positive, we must return to the preceding point and solve the ray equation with the focal plane equation (but not with the equations for the cube faces). In this way we obtain the coordinate of the ray on the focal plane. The sum of all the optical paths (including the last segment) gives the optical path of the ray.

In these calculations the polarization of the ray was not investigated and the square of the amplitude of the transmitted ray was multiplied by the half-sum of the squares of the Fresnel coefficients for both polarizations. The square of the amplitude on the focal plane is the product of these factors in all the iterations. In cases of glancing incidence, less energy may enter the refracted ray than the reflected ray. In this case, in one variant of the program, the path of the reflected ray is then traced.

Some rays leave the lens almost parallel to the focal plane and their motion outside the lens is described by numerous iterations. The smallest number of iterations is obviously $2a$. The program discarded a ray which had not reached the focal plane after $6a$ iterations.

3. If $\mu=0$ (the beam is normal to the two faces of the cubes), the rays do not undergo refractions, no focusing occurs, and the distribution of the rays on the focal plane is the same as that on the entry plane. For small μ (i.e., when $1-|\gamma_0|\ll 1$) the discrete lens does not differ so appreciably from the continuous one, but focusing will be considerably weaker; the same will be found for $1-|\alpha_0|\ll 1$ and $1-|\beta_0|\ll 1$. However, when the direction of the beam is random, the probability of the angle between the beam and the edges being small will be of order $\frac{3}{2}\mu^2$, and even for $\mu \approx 1/10$ these ''bad'' directions will only account for around 6%.

Nevertheless, the calculations have shown that even for the ''rough'' division which has been analyzed ($2a=17$), the discreteness still leads to appreciably weaker focusing. We shall give some of the results.

One of the characteristics of the focusing action of a lens formed by cubes is the distance $\bar{r}$ between the focus and the point of intersection, averaged over all the rays which have intersected the focal plane. For a continuous lens $\bar{r}=0$ would be obtained (geometric-optics calculations). For $\mu=0$, i.e., in the absence of refraction, we obtain $r=2a/3$, which for $a=8.5$ gives $r=5.7$. Figure 1 gives $\bar{r}$ as a function of μ for two versions of the program: *1* — in which the path of that refracted or reflected ray carrying the greater energy is traced subsequently for glancing incidence; *2* — the path of the refracted ray is always traced (except for cases of total internal reflection). Version *1* more accurately reproduces the ray propagation process. The value of $\bar{r}$ for moderate μ is of the order of 1–2. This value must be compared with the diffraction radius of the focal spot having the order λ (Ref. 1).

The focusing quality is also characterized by the energy distribution on the focal plane. For instance, if the beam forms equal angles (55°) with all three axes, 0.24 of the entire energy reaching the focal plane is found within the ring on this plane between radii $r=1$ and $r=2$.

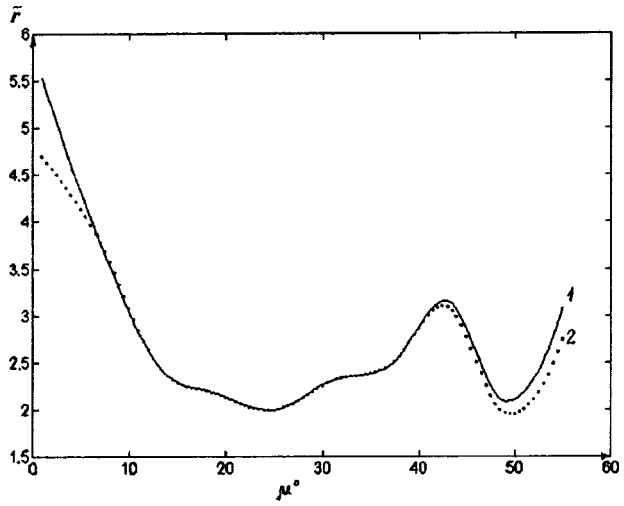

FIG. 1.

Another characteristic is the dispersion of the optical path length: for a continuous lens this is zero. For rays whose distance from the focus is less than 1, this dispersion is ≈ 0.5 and if the distance from the focus is less than $a/2$, the dispersion is ≈ 1.

These examples (and more detailed results not reported here) show that if the number of cubes is approximately 2000–3000, the focusing of the lens is appreciably inferior to that for a continuous distribution of ε. With this discretization the ε jump at the faces is of order $\Delta\varepsilon=0.1$, which is clearly too large.

Note that the number of rays M is proportional to a^2 and the number of iterations for each ray is proportional to a, so that the number of operations in this method increases as a^3, i.e., $(\Delta\varepsilon)^{-3}$.

[1] A. V. Golubyatnikov and B. Z. Katsenelenbaum, Radiotekh. Elektron. **42**, No. 12 (1997).

Translated by R. M. Durham

Investigation of the thermal stability of picosecond gallium arsenide dynistor switches

K. V. Evstigneev, V. I. Korol'kov, and A. V. Rozhkov

A. F. Ioffe Physicotechnical Institute, Russian Academy of Sciences, St. Petersburg
(Submitted March 2, 1998)
Pis'ma Zh. Tekh. Fiz. **24**, 73–78 (August 12, 1998)

The operation of GaAs $n^+-p-i-n^0-p^+$ dynistor structures has been demonstrated experimentally under conditions of reversible avalanche breakdown at temperatures up to 200 °C with switching times remaining under 140 ps. A numerical simulation refined the influence of various parameters of the semiconductor on the temperature dependence of the switching characteristics. © *1998 American Institute of Physics.* [S1063-7850(98)01308-1]

Among well-known powerful, high-speed, picosecond switches, those operating on the principle of switching using a delayed impact ionization wave belong to a special class. These semiconductor switches usually do not have a steady-state *S*-shaped current–voltage characteristic and function in a regime with reversible dynamic breakdown of a high-voltage $p-n$ junction. Dynamic breakdown is accompanied by a nonuniform distribution of current over area with the formation of filaments of high-current density and an ensuing appreciable rise in temperature near the $p-n$ junction. Both these factors impose severe constraints on the operating characteristics of silicon-based structures. Thus, the results of investigating structures fabricated using different, wider-gap materials are attracting particular interest.

We investigated the thermal stability of high-voltage switches using an $n^+-p-i-n^0-p^+$ GaAs dynistor structure. The central, high-voltage, linear-gradient $p-i-n^0$ junction was grown by liquid-phase epitaxy. The junction was formed by varying the concentration of background donor and acceptor impurities. These structures typically exhibit antisite defects with two levels in the lower half of the band gap and a concentration of $(0.5-2)\times 10^{15}$ cm^{-3} (Ref. 1). At room temperature the maximum forward dc voltage before breakdown was 600–800 V. The coefficient of positive feedback between the emitter junctions was less than 1 at voltages up to breakdown. The working area of the device was 0.5 mm^2.

The main switching parameters of the devices were measured when these operated as current pulse sharpening devices. The sharpened pulse had an amplitude of 400 V at 50 Ω load with a 0.3 ns rise time and a temporal stability better than 30 ps. This pulse was applied with a fixed bias to a 50 Ω line and the dynistor being investigated was connected in a gap. A matched load was connected to the other end of the line. At room temperature fast switching was observed at bias voltages from 90 V almost up to the static breakdown voltage. The transition time to the conducting state was around 100 ps with a delay of 0.1–0.4 ns relative to the input pulse (Fig. 1).

As expected, this switch exhibited substantially better thermal stability than known silicon picosecond switches, for

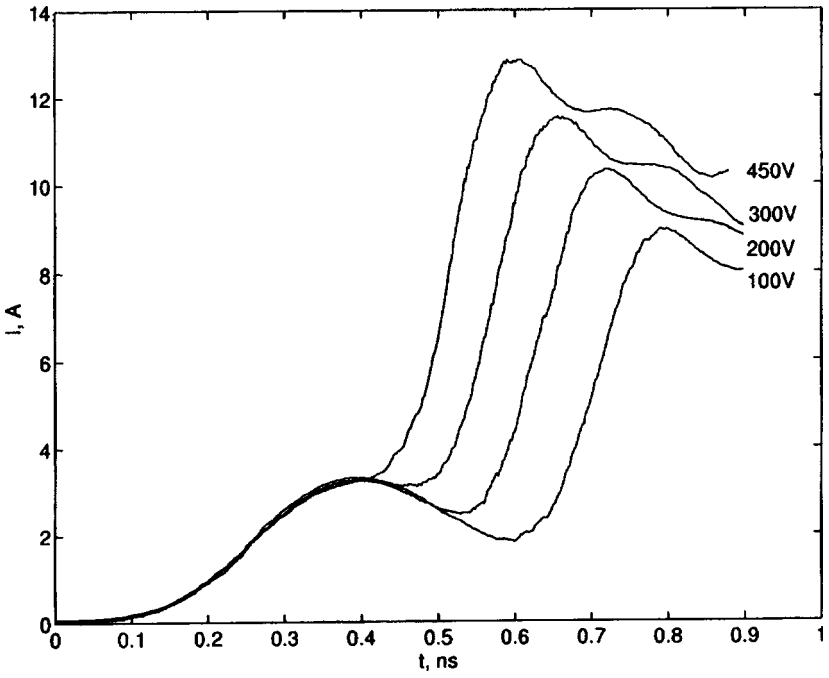

FIG. 1. Oscilloscope traces of current through peaking dynistor at various bias voltages.

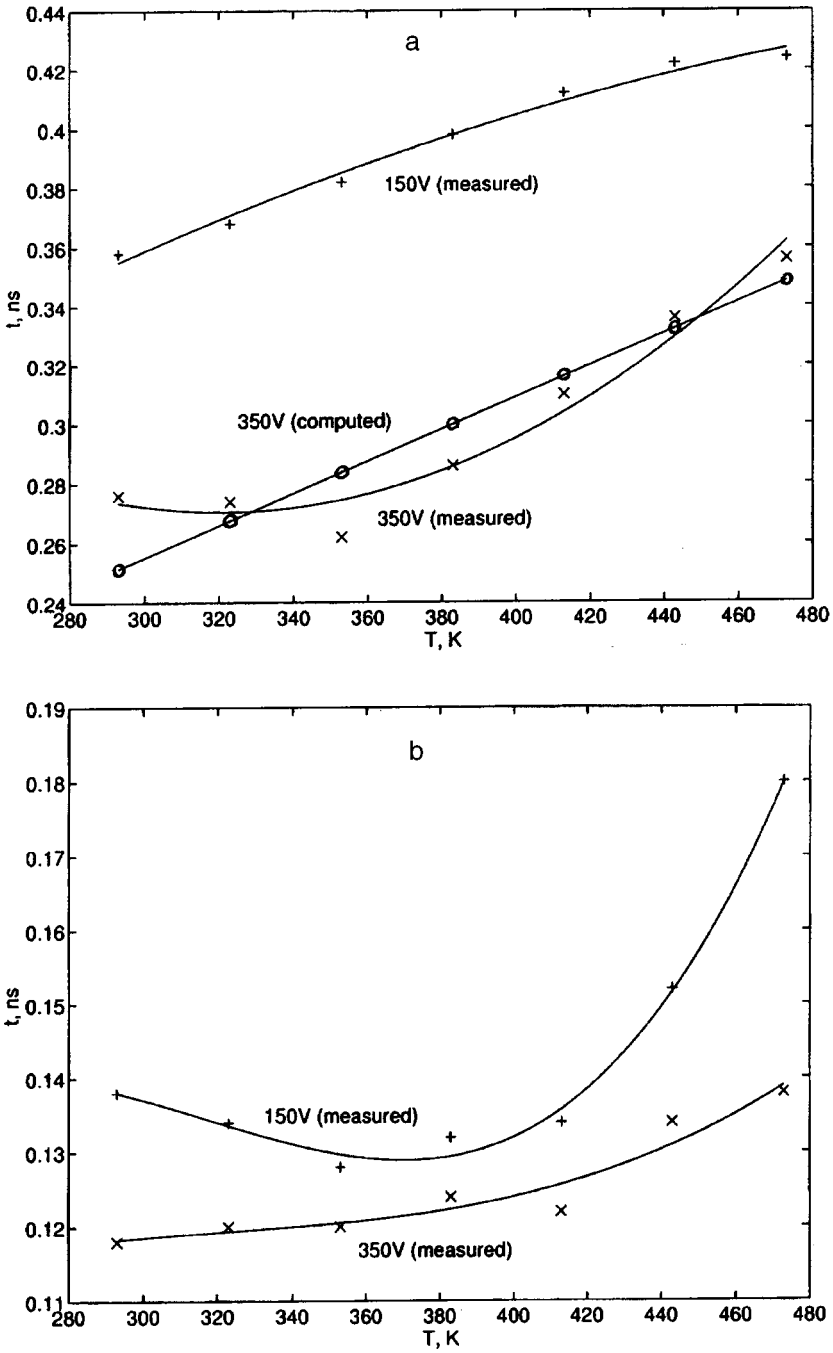

FIG. 2. Temperature dependences of switching delay (a) and switching time (b) at various bias voltages.

which the operating temperature limit was at most 100 °C. However, heating the gallium arsenide dynistors to 200 °C merely increased the switching delay and caused a slight drop in the current amplitude. Figure 2a gives temperature dependences of the switching delay relative to the sharpened pulse which clearly shows that this parameter typically increases with increasing temperature and decreasing bias voltage. The rise time of the sharpened pulse also increases (by 10–15%) with heating (Fig. 2b). This figure clearly shows that the switching process slows appreciably with increasing temperature at a bias voltage of 150 V. This can be explained by the fact that the minimum fixed bias to ensure sharpening was less than 90 V at room temperature but approached 130–150 V at 200 °C.

Note that the instability of the switching delay time (jitter) was almost independent of temperature and was 30 ps for most temperatures and bias voltages. Exceptions were the lowest values of the fixed bias close to the lower threshold of the sharpening regime and the highest values close to the static switching voltage, where the instability increased to 120–150 ps. This behavior of the temporal instability in the boundary regions is generally typical of gallium arsenide diode[2] and thyristor[3] structures.

In order to explain the switching pattern of this device, we made a numerical simulation of the breakdown of the base regions. We used a diode $p-i-n^0$ structure similar to the base regions of our dynistor as a model. The simulation took into account drift, diffusion, recombination and thermal

generation (in the simplest band–band representation), and impact ionization. The dynamics of the processes were described by the system of continuity equations

$$\begin{cases} \dfrac{dE}{dt} = \dfrac{4\pi}{\epsilon}[J - e(j_p - j_n)], \\ \dfrac{dp}{dt} = t - r(p,n) + g(E,p,n) - \dfrac{\partial}{\partial x}[pv_p(E)] + D_p \dfrac{\partial^2 p}{\partial r^2}, \\ \dfrac{dn}{dt} = t - r(p,n) + g(E,p,n) - \dfrac{\partial}{\partial x}[nv_n(E)] + D_n \dfrac{\partial^2 n}{\partial x^2}, \end{cases}$$

where E is the electric field strength, J is the density of the total current through the device determined by the external circuit and by the geometry of the instrumental structure, j_p and j_n are the particle current densities, and t, r, and g are the rates of thermal generation, recombination, and impact ionization, respectively. A fairly elaborate approximation given in Ref. 4 was used as the impact ionization coefficient.

The assumption that the conductance of the high-resistivity region was uniformly modulated over area did not produce quantitative agreement between the calculated and experimental time dependences of the current through the device. However, theoretical analysis of the stability of impact ionization waves in $p-p$ junctions[5] indicates that the assumption of uniform breakdown is rather unrealistic. In this particular device, the wave is transversely unstable (although to a lesser extent than in an abrupt p^+-i-n^+ structure) and the breakdown should be local. By fitting to the experimental results, it was established that approximately 0.25 of the entire area of the central junction is transferred to the conducting state, which was also assumed in the simulation.

The numerical calculations indicate that as the temperature rises, the switching delay of the dynistor should increase (Fig. 2a) while the switching time should remain almost constant. The change in the form of the current pulse through the device was merely a result of the temperature dependence of the impact ionization coefficients. A reduction in the mobilities and diffusion coefficients has little influence on the external switching characteristics. The constant switching time can be explained by the fact that in the TRAPATT regime the rate of current rise through the device is mainly a function of the parameters of the external circuit and the geometric dimensions of the device. An increase in the switching delay results from an increase in the threshold field needed for breakdown. An increase in the threshold field is caused by a decrease in the coefficients of impact ionization, which may also be responsible for increased losses in the switched state.

To sum up, the results of an experimental investigation and numerical simulation indicate that gallium arsenide dynistor peaking devices operate successfully at elevated temperature. The results of the simulation suggest that the changes in the dynamic parameters are merely caused by the thermal dependence of the impact ionization coefficients. Changes in the carrier transport coefficients had no significant influence up to 200 °C.

In conclusion, the authors would like to thank S. V. Shendereĭ for numerous discussions and useful comments on the experimental part of this work.

[1] Yu. M. Zadiranov, V. I. Korol'kov, S. I. Ponomarev *et al.*, Zh. Tekh. Fiz. **57**, 771 (1987) [Sov. Phys. Tech. Phys. **32**, 466 (1987)].
[2] Zh. I. Alferov, I. V. Grekhov, V. M. Efanov *et al.*, Pis'ma Zh. Tekh. Fiz. **13**, 1089 (1987) [Sov. Tech. Phys. Lett. **13**, 454 (1987)].
[3] V. I. Korol'kov, A. S. Prokhorenko, A. V. Rozhkov, and A. M. Sulatanov, Pis'ma Zh. Tekh. Fiz. **18**(10), 26 (1992) [Sov. Tech. Phys. Lett. **18**, 311 (1992)].
[4] Hin-Fai Chau and D. Pavlidis, J. Appl. Phys. **72**, 531 (1992).
[5] A. M. Minarskiĭ and P. V. Rodin, Fiz. Tekh. Poluprovodn. **31**, 432 (1997) [Semiconductors **31**, 366 (1997)].

Translated by R. M. Durham

Nanostructure and radiation resistance of carbon stripper foils

A. V. Vasin, V. G. Vysotskiĭ, and L. A. Matveeva

Institute of Semiconductor Physics, Ukraine National Academy of Sciences, Kiev
(Submitted February 17, 1998)
Pis'ma Zh. Tekh. Fiz. **24**, 79–84 (August 12, 1998)

Raman light scattering has been used to analyze the short-range order structure of carbon stripper foils. It has been shown that the radiation resistance of the foils depends strongly on their nanostructure. It was observed that under the action of a 2 MeV hydrogen ion beam, soot-like foils have a considerably longer life than foils with a graphite-like nanostructure.
 [S1063-7850(98)01408-6]

Self-supporting amorphous carbon foils 25–100 nm thick are used in charge-transfer electrostatic accelerators (tandems) to ''strip'' negatively charged ions. Ions undergo more efficient charge transfer in carbon strippers compared with gas targets, which enhances the energy of the positive ions at the accelerator exit. However, the radiation resistance of carbon foils is a problem.

It has been established[1–4] that damage to stripper foils exposed to ion beams is caused by their graphitization and by the formation of stresses in the irradiation zone. Foils deposited by vacuum thermal techniques usually have the texture of graphite-like clusters with basal planes (002) parallel to the substrate. As a result of radiation defects in the graphitized zones, the foils exhibit ''swelling'' perpendicular to their plane and compression along the surface.[2–4] This leads to the formation and buildup of mechanical stresses in the stripper, which are accompanied by cracking, rendering further operation of the accelerator impossible. The operating life of carbon foils can be improved appreciably by using ion-plasma methods of deposition.[1,4] However, these methods require complex and expensive equipment.

The aim of the present paper was to study the nanostructure and radiation resistance of carbon stripper foils obtained by a spark method.[5] Pointed graphite rods were heated by ~ 50 A current pulses at a working pressure of 10^{-3} Pa. The foils were deposited on glass precoated with a soluble sublayer of sodium chloride around 150 nm thick. The foils were then removed from the substrates in distilled water and mounted on copper mandrels which were placed in the charge-transfer drum of the EGP-10 accelerator at the Institute of Nuclear Research (Kiev). The foils were studied under various irradiation doses (10^{16}–10^{17} cm^{-2}) of 2 MeV hydrogen ions at a beam current density of 10 μA/cm^2.

The nanostructure of the foils was investigated using Raman light scattering. Raman spectra for irradiated and unirradiated sections of the foils extracted from the charge-transfer drum were measured using a DFS-24 spectrophotometer with an FÉU-136 photomultiplier in the photon counting mode. The spectra were excited using the 514.5 nm argon laser line.

The results of the investigations showed that foils obtained under apparently the same deposition conditions have completely different Raman spectra and are quite differently influenced by irradiation. Typical spectra are shown in Fig. 1 for one type of foil and in Fig. 2 for a different type. The Raman spectrum of the type-I foils before irradiation (Fig. 1, curve *1*) has a well-defined band near 1580 cm^{-1} and a weak but broad band near 1350 cm^{-1}. After exposure to a dose of $\sim 10^{16}$ cm^{-2}, the relative intensity of the 1350 cm^{-1} band increases and the half-width of the 1580 cm^{-1} band decreases (Fig. 1, curve *2*).

The Raman spectrum of an unirradiated section of type-II foil (Fig. 2, curve *1*) consists of a high-intensity, fairly narrow line $\nu = 1370$ cm^{-1} and two weak bands near 1450 and 1580 cm^{-1}. Even when these foils were exposed to a dose of 10^{17} cm^{-1}, the spectra showed no fundamental changes (Fig. 2, curve *2*), which reflects the radiation resistance of this structure. To explain these results, we shall examine the published data.

The first-order Raman scattering spectrum of ordered graphite consists of a single line at a frequency of around 1580 cm^{-1} known as the *G*-line (''graphitic''). In finely crystalline graphite with disordered regions of ~ 30 nm, an additional line is observed near 1355 cm^{-1} which is usually called the *D*-line (''disordered'').[6,7] This band corresponds to the phonon density-of-states peak in solid graphite at the edge of the Brillouin zone and is observed as a result of the weakening of the selection rule for the wave vector in disordered structures. The ratio I_D/I_G of the intensities of the *D* and *G* bands depends nonmonotonically on the size of the graphite nanocrystallites. As these decrease in size in disordered graphite, the ratio I_D/I_G increases since the fraction of phonons far from the center of the Brillouin zone increases in the scattering process. However, below a certain threshold ($\leqslant 10$ nm) the relative intensity of the *D* band begins to decrease.[8] This is attributed to a decrease in the phonon density of states corresponding to the graphite crystal lattice in a strongly disordered system. In the Raman spectra of a diamond crystal the only active line is $\nu = 1332$ cm^{-1}. The highest-intensity lines in the spectra of the fullerenes C_{60} and C_{70} are those at frequencies of 1470 cm^{-1} and 1570 cm^{-1}, respectively.[9,10]

A comparison between these results and the published data indicates that the unirradiated type-I foils have a well-defined *G*-band and a weak *D*-band. Irradiation causes graphitization even at a dose of 10^{16} cm^{-2} which is observed

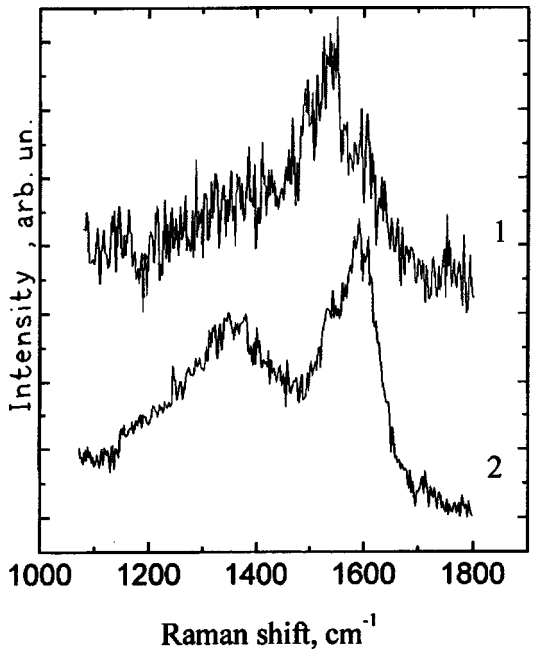

FIG. 1. Raman spectra of type-I carbon foils: *1* — unirradiated section, *2* — section irradiated by a dose of 10^{16} cm^{-2}.

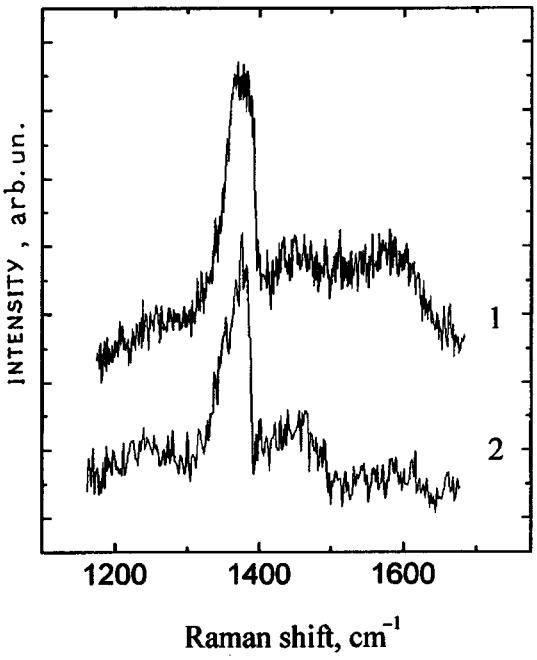

FIG. 2. Raman spectra of type-II carbon foils: *1* — unirradiated section, *2* — section irradiated by a dose of 10^{17} cm^{-2}.

as an increase in the relative intensity I_D/I_G. We observed a similar change in the Raman spectra after type-I unirradiated foils had been thermally annealed in vacuum at 800 °C.

The weakly defined 1580 cm^{-1} *G*-line in type-II foils suggests that these have a low content of three-dimensionally ordered graphite-like regions. The 1370 cm^{-1} and 1450 cm^{-1} lines identified for these foils were also observed in fullerene-containing soot.[9,10] However, the highest-intensity lines of the C_{60} and C_{70} molecules (1470 cm^{-1} and 1570 cm^{-1}) did not appear in our foils.

The most surprising result is that even at extremely high doses (an order of magnitude higher than those for type-I foils), no signs of graphitization are detected in type-II foils. Thermal annealing of unirradiated type-II foils in vacuum at 800 °C also produced no significant changes in the spectra. Whereas some type-I foils revealed cracking even at doses of $\leqslant 10^{16}$ cm^{-2}, type-II foils withstood doses of $\geqslant 10^{17}$ cm^{-2} without any catastrophic cracking.

To conclude, the results of a study of the nanostructure of carbon stripper foils suggest that their radiation and thermal resistance and therefore their operating life are determined by the initial nanostructure. Unfortunately, it has not yet been established for certain which of the technological parameters (deposition rate, current density, vapor-phase ion component, and so on) is mainly responsible for the nanostructure of the foils. Further research in this direction is required to ascertain this. However, it has been conclusively established that, in principle, the radiation resistance of carbon stripper foils may be improved substantially without using complex and expensive technologies.

[1] N. R. S. Tait, Nucl. Instrum. Methods **184**, 203 (1981).
[2] G. Dollinger and P. Maier-Komor, Nucl. Instrum. Methods Phys. Res. A **282**, 223 (1989).
[3] G. Dollinger, P. Maier-Komor, and A. Mitwalsky, Nucl. Instrum. Methods Phys. Res. A **303**, 79 (1991).
[4] G. Dollinger, C. M. Frey, and P. Maier-Komor, Nucl. Instrum. Methods Phys. Res. A **334**, 167 (1993).
[5] G. N. Kozeratskaya, N. F. Onoshko, and V. A. Stepanenko, *Boron, Silicon, and Carbon Targets for Nuclear Research*, Preprint No. KIYaI–87–50 [in Russian], Kiev Institute of Nuclear Research, Kiev (1987), 13 pp.
[6] Hisao-chu Tsai and D. B. Bogy, J. Vac. Sci. Technol. Phys. Res. A **5**, 3287 (1987).
[7] M. A. Tamor, J. A. Haire, C. H. Wu *et al.*, Appl. Phys. Lett. **54**, 123 (1989).
[8] R. O. Dillon, J. A. Woollam, and V. Karkanant, Phys. Rev. B **29**, 3482 (1984).
[9] D. S. Bethun, G. Meijer, W. C. Tang *et al.*, Chem. Phys. Lett. **174**, No. 3–4 (1990).
[10] A. V. Eletskiĭ and B. M. Smirnov, Usp. Fiz. Nauk **165**, 977 (1995).

Translated by R. M. Durham

Photodeflection response of a gyrotropic–isotropic sample under conditions of tunneling electromagnetic interference

P. V. Astakhov and G. S. Mityurich

Homel F. Skaryna State University, Belarus
(Submitted January 8, 1998)
Pis'ma Zh. Tekh. Fiz. **24**, 85–89 (August 12, 1998)

Calculations of the energy dissipation of oppositely directed light beams in a gyrotropic–isotropic sample are used to determine the photodeflection response. It is shown that the photodeflection signal can be completely suppressed when the beams interact while propagating in opposite directions. © *1998 American Institute of Physics.* [S1063-7850(98)01508-0]

Tunneling electromagnetic interference accompanying the counterpropagating interaction of light waves in an absorbing sample has been studied theoretically and experimentally.[1,2] It was shown in Ref. 2 that as a result of the redistribution of energy by interference, the transmission coefficient of the medium depends strongly on the energy and polarization characteristics of the counterpropagating light beams. Allowance for spatial dispersion effects in the counterpropagating interaction of electromagnetic waves can substantially alter the bulk interference pattern inside the layer.[3] However, if the medium possesses gyrotropic properties, the theoretical expressions become considerably more complicated and require further analysis.

Photoacoustic and photodeflection spectroscopy is now being successfully used to study the thermal and dissipative properties of gyrotropic media.[4] A distinguishing feature of these methods is their high sensitivity and the indirect method of recording the absorbed optical energy which allows nontransparent samples to be studied.

Calculations of the photoacoustic signal were made in Ref. 5 for a sample excited by oppositely propagating beams, and it was shown that the recorded response can be effectively controlled. The formation of a photodeflection response as a result of interaction between oppositely directed beams in a gyrotropic medium is also of considerable interest, since photodeflection spectroscopy, possessing the main advantages of photoacoustics, is fairly sensitive to bulk changes in the temperature of the medium.

We shall analyze the formation of a photodeflection signal in a plane-parallel gyrotropic–isotropic layer excited by two oppositely propagating electromagnetic waves with electric field strengths E_1 and E_3. We shall assume that the z axis is perpendicular to the layer and the coordinates of the interfaces with the surrounding transparent media *1* and *3* are denoted by $z=-d$ and $z=d$, respectively.

By solving a boundary-value electrodynamic problem using the rate equations for gyrotropic absorbing media[6] and expressions for the fields inside the layer, we derive an expression for the energy dissipation Q per unit volume of the sample:

$$\begin{aligned} Q=\omega\{&\varepsilon''(|\mathbf{A}_+|^2+|\mathbf{A}_-|^2+|\mathbf{B}_+|^2+|\mathbf{B}_-|^2 \\ &+2[\mathrm{Re}(\mathbf{A}_+\cdot\mathbf{B}_-^*)+\mathrm{Re}(\mathbf{A}_-\cdot\mathbf{B}_+^*)]) \\ &+4\gamma''(n_0'(|\mathbf{A}_+|^2-|\mathbf{A}_-|^2+|\mathbf{B}_+|^2-|\mathbf{B}_-|^2) \\ &+2n_0''[\mathrm{Im}(\mathbf{A}_+^*\cdot\mathbf{B}_-)+\mathrm{Im}(\mathbf{A}_-^*\cdot\mathbf{B}_+)])\}. \end{aligned} \tag{1}$$

In expression (1) we have written $n_0=\sqrt{\varepsilon}$, and $\mathbf{A}_\pm$ and $\mathbf{B}_\pm$ are expressed in terms of the energy and polarization characteristics of the interacting waves and the optical parameters of the medium.[3]

The energy dissipation Q, determined in accordance with Eq. (1), is the power density of the heat sources in the system of heat conduction equations:

$$\Delta T-\frac{1}{\beta}\frac{dT}{dt}=\begin{cases} 0, & z<-d, \\ -\dfrac{1}{k}Q(\mathbf{r},t)\exp(i\omega t), & -d\leqslant z\leqslant d, \\ 0, & z>d, \end{cases} \tag{2}$$

which describes the temperature distribution in the sample and the surrounding medium under the action of modulated laser radiation.

After solving the system (2) and calculating the temperature fields, we can directly determine the deflection of the probe beam. Assuming that the probe beam propagates through a transparent medium *1* with the refractive index n_1 parallel to the surface of the layer, we can write the following expression for the transverse component of the angle of deflection

$$\Phi(x,y,z)=\frac{1}{n_1}\frac{dn_1}{dT}\int_y\frac{dT(x,y,z,t)}{dx}dy, \tag{3}$$

which we shall subsequently analyze. In expression (3) dn_1/dT is the temperature gradient of the refractive index of the medium through which the probe beam propagates.

On analyzing these results, we note that expression (1) can be reduced to the form

$$Q=F_1E_1^2+F_3E_3^2+F_{13}E_1E_3, \tag{4}$$

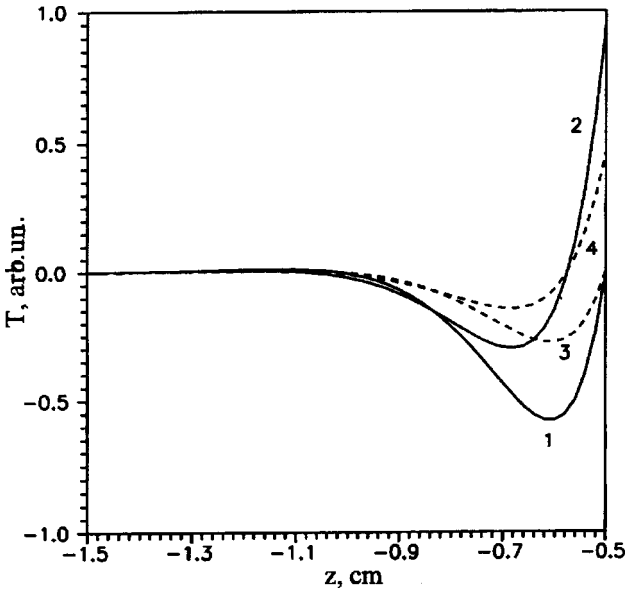

FIG. 1. Distribution of the variable component of the temperature in a transparent medium *1* at various modulation frequencies of the exciting radiation: *1* — $\omega=15.0$ Hz, $E_3=10^{-6}$ V/m; *2* — $\omega=15.5$ Hz, $E_3=10^{-6}$ V/m; *3* — $\omega=15.0$ Hz, $E_3=0$; *4* — $\omega=15.5$ Hz, $E_3=0$.

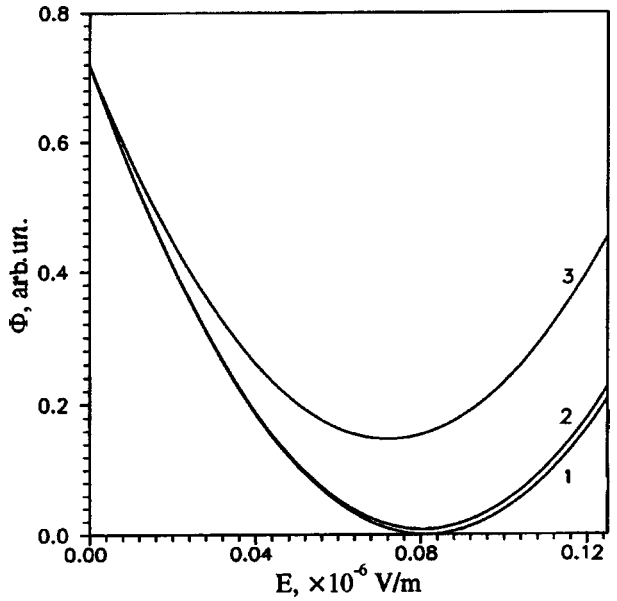

FIG. 2. Photodeflection response versus electric field E_1: *1* — $\gamma'=10^{-3}$, $\gamma''=10^{-5}$; *2* — $\gamma'=10^{-3}$, $\gamma''=2\times10^{-5}$; *3* — $\gamma'=5\times10^{-3}$, $\gamma''=10^{-5}$.

from which it follows that for a constant field E_3 relation (4) has a parabolic dependence $Q=f(E_1)$, where the minimum energy dissipation is achieved when $E_1=-F_{13}E_3/2F_1$.

The nonsteady-state component of the temperature field varies in the transparent medium *1* as a result of the condition that the temperature T and the heat flux $k_g dT/dz$ are equal at the interface of the sample. Figure 1 shows that the variable component of the temperature decays completely over the distance $z=2\pi\mu$ from the interface, where μ is the thermal diffusion length. For air with the incident radiation modulated at the frequency $\omega=15$ Hz, the thermal diffusion length is ≈ 0.159 cm. The calculations show that the contribution of the interacting oppositely propagating beams to the resultant distribution of the nonsteady-state temperature component is observed as a slight increase in the amplitude of the resulting thermal wave.

We shall analyze the dependence of the angle of deflection on the electric field strength of the first wave when the field of the second is constant. The calculations show that when the probe beam propagates parallel to the interface over a distance L shorter than the thermal diffusion length, the angle of deflection has a minimum, and with a suitable choice of measurement conditions the photodeflection response can be completely suppressed (Fig. 2). As a result of the modulated absorption of optical energy by the sample, the position of the minimum point is appreciably determined by the frequency of the amplitude modulation of the incident radiation. An increase in the real part of the gyration parameter γ' leads to the disappearance of this effect as a result of the additional rotation of the major axes of the polarization ellipses of the light waves, which alters the pattern of energy redistribution by interference. An increase in the imaginary part of the gyration parameter γ'' negligibly increases the amplitude of the photodeflection response.

To sum up, it has been shown that the photodeflection response in a gyrotropic medium may be suppressed by the interaction of the oppositely propagating light waves. Dissipative effects and gyrotropy have an appreciable influence on the angles of deflection of the probe beam.

[1] R. V. Bakradze, N. B. Brandt, and V. V. Tolmachev, *Mechanics of Continuous Media* [in Russian], Moscow (1984).
[2] V. V. Sidorenkov and V. V. Tolmachev, Pis'ma Zh. Tekh. Fiz. **15**(21), 34 (1989) [Sov. Tech. Phys. Lett. **15**, 844 (1989)].
[3] G. S. Mityurich and P. V. Astakhov, in *Proceedings of the Ninth International Conference on Photoacoustic and Photothermal Phenomena*, Nanjing, China, 1996; Prog. Nat. Sci. **6**, 701 (1996).
[4] A. Salasar, A. Sanhez-Lavega, and J. Fernandez, J. Appl. Phys. **65**, 4150 (1989).
[5] G. S. Mityurich, V. P. Zelyony, V. V. Sviridova, and A. N. Serdyukov, in *Proceedings of the Ninth International Conference on Photoacoustic and Photothermal Phenomena*, Nanjing, China, 1996, pp. 275–276.
[6] F. I. Fedorov, *Theory of Gyrotropy* [in Russian], Nauka i Tekhnika, Minsk (1976) 456 pp.

Translated by R. M. Durham

Modeling of phenomenological processes in ferromagnetics and ferroelectrics

A. T. Ovakimyan

Research Institute of Optophysical Measurements, Erevan
(Submitted February 17, 1998)
Pis'ma Zh. Tekh. Fiz. **24**, 90–95 (August 12, 1998)

A vector model to used investigate and simulate the phenomenological properties of ferromagnetics and ferroelectrics.
[S1063-7850(98)01608-5]

Certain difficulties encountered in the qualitative and quantitative description of the main phenomenological properties of ferromagnetics and ferroelectrics[1] can easily be overcome by means of a mathematical model.

Such a model may be obtained by considering the behavior of the domain structures as a consequence of the energy conservation law.

To demonstrate this, let us consider a ferromagnetic single crystal in the form of a rectangular parallelepiped.

Let us take the limiting cases when the crystal is completely magnetized to saturation, in the longitudinal direction for instance, under the action of an external magnetic field. In this case, the magnetic moments of all the domains are oriented in the same direction and the entire crystal appears to be a single domain (Fig. 1, which shows one crystal plane for clarity). We shall sum the vectors of the magnetic moments of the domains and find the point of application of the resultant magnetic moment $\mathbf{M}=\Sigma_{i=1}^{S}\mathbf{m}_i$, where $\mathbf{M}$ is the resultant magnetic moment and $\mathbf{m}_i$ is the magnetic moment of the ith domain.

It follows from the properties of parallel vectors that the point of application of a resultant vector coincides with the geometric center of the crystal. Assuming that the crystal contains no nonferromagnetic inclusions, the point of application of the resultant magnetic moment C_m exactly coincides with the center of mass of the crystal. If the crystal is remagnetized to saturation in any other direction, the position C_m remains unchanged relative to the crystal.

We shall show that C_m cannot alter its coordinates for any rotation of the magnetic moments of the domains because this would violate the energy conservation law. We imagine that our crystal is suspended by the center of mass in a nonvarying external magnetic field. If the crystal is made to rotate, the domains begin to move and rotate under the influence of the external magnetic field. If the magnetic moments of the domains always position themselves so that C_m will be displaced, the crystal will be exposed to mechanical rotating moments about the point of suspension, and will rotate continuously in the nonvarying magnetic field, which is impossible.

Thus, the resultant magnetic moment may vary in magnitude and direction as a function of changes in the crystal magnetization, rotating relative to the point of application C_m which cannot alter its coordinates relative to the crystal. We shall analyze the necessary conditions for fixed C_m. We shall take the particular case when the magnetic moments of the domains in the crystal are oriented in three mutually perpendicular directions, forming three systems of parallel vectors (Fig. 2). We shall select the coordinate axes such that their origin coincides with C_m and the directions are parallel to the magnetic moments of the domains. Then, from the properties of parallel vectors, the coordinates of the point of application of the resultant magnetic moment for domains oriented along the X axis are given by the following relations:

$$Xx=\sum_{i=1}^{l}\mathbf{m}_i x_i \Big/ \sum_{i=1}^{l}\mathbf{m}_i=0,$$

$$Yx=\sum_{i=1}^{l}\mathbf{m}_i y_i \Big/ \sum_{i=1}^{l}\mathbf{m}_i=0,$$

$$Zx=\sum_{i=1}^{l}\mathbf{m}_i z_i \Big/ \sum_{i=1}^{l}\mathbf{m}_i=0,$$

where Xx, Yx, and Zx are the coordinates of the resultant magnetic moment of the domains parallel to the X axis, $\mathbf{m}_i$ is the magnetic moment of the ith domain parallel to the X axis, and x_i, y_i, and z_i are the coordinates of the magnetic moment of the ith domain.

Since $\Sigma_{i=1}^{l}\mathbf{m}\neq 0$, we obtain

$$\sum_{i=1}^{l}\mathbf{m}_i x_i=0, \quad \sum_{i=1}^{l}\mathbf{m}_i y_i=0, \quad \sum_{i=1}^{l}\mathbf{m}_i z_i=0. \tag{1}$$

Likewise for the Y and Z axes we obtain

$$\sum_{j=1}^{n}\mathbf{m}_j x_j=0, \quad \sum_{j=1}^{n}\mathbf{m}_j y_j=0, \quad \sum_{j=1}^{n}\mathbf{m}_j z_j=0, \tag{2}$$

$$\sum_{k=1}^{p}\mathbf{m}_k x_k=0, \quad \sum_{k=1}^{p}\mathbf{m}_k y_k=0, \quad \sum_{k=1}^{p}\mathbf{m}_k z_k=0, \tag{3}$$

where $\mathbf{m}_j$ and $\mathbf{m}_k$ are the magnetic moments of the domains parallel to the Y and Z axes, respectively, x_j, y_j, z_j and x_k, y_k, z_k are the coordinates of the magnetic moments of the domains parallel to the Y and Z axes, respectively.

Relations (1)–(3) imply the following:

1. The rotations of the magnetic moments of the domains should be symmetric relative to the ZC_mX, ZC_mY, and XC_mY planes (Fig. 2). For instance, the rotation of the mag-

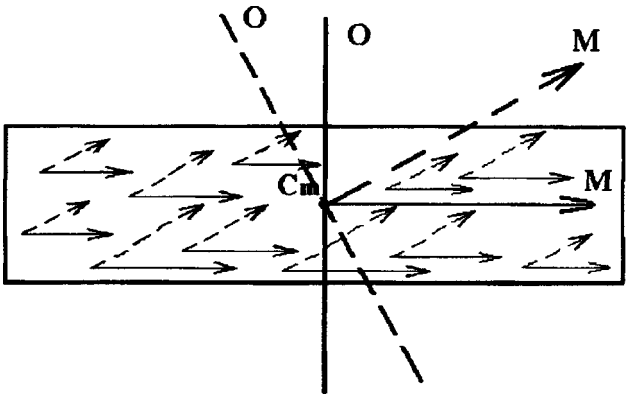

FIG. 1.

netic moments of part of a domain, a single domain, or several domains (displacement and rotation processes) parallel to the ZC_mY plane, to the left of this plane, should be accompanied by a simultaneous rotation of the magnetic moments of the domains to the right so that the sums of the products of the magnetic moments at distances to the left and right of the ZC_mY plane are the same. The same also applies to the ZC_mX and XC_mY planes. Rotations of the magnetic moments of the domains only to the left or only to the right of these planes are impossible.

2. If the domain magnetic moments rotate when they are not parallel and not perpendicular to the magnetic moments of other domains, the coordinates of C_m can only be kept constant by deformation of the crystal, which will disappear after the magnetic moments have completed their rotation.

3. If in general the magnetic moments of the domains are not mutually parallel and not mutually perpendicular, the coordinates of C_m can only be kept constant by deformation of the crystal, which will vary as the crystal magnetization varies.

4. If our crystal is cut into sections and these are separated by distances sufficient to eliminate intercorrelation of the domains, the magnetic moments of the domains in each part should be positioned so that C_m for each part satisfies the above condition. It can be shown that this reorientation

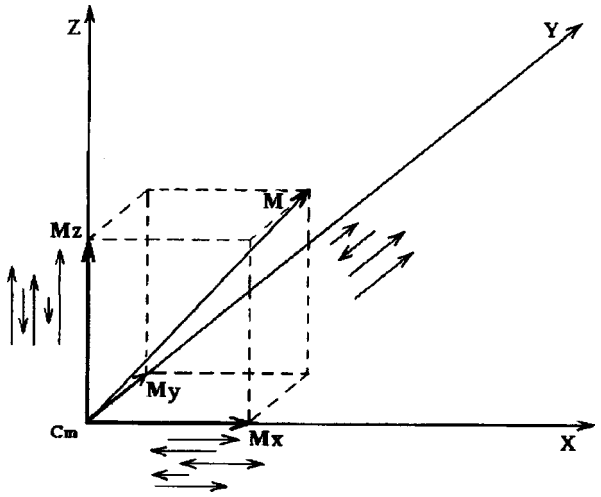

FIG. 2.

can take place with the lowest energy consumption (with the fewest rotations of the magnetic moments of the domains) if the resultant magnetic moments of the separate sections are aligned relative to these sections in the same direction as the initial magnetic moment of the crystal before cutting.

5. An analysis of the initial data used to obtain relations (1)–(3) shows that they can also be derived similarly for other magnetic materials possessing a domain structure. Bearing in mind that in the initial data, we did not envisage any constraints on the presence or absence of field sources (charges), we can also apply these relations to the electric domains of ferroelectrics in an external electric field.

It is readily shown that we have obtained a vector model which simulates the main phenomenological properties (#1 — the dipole nature and hysteresis, #2 — the Barkhausen effect, #3 — magnetostriction, #4 — the division of a permanent magnet into smaller sections, and #5 — the electrical analog of ferromagnetism in ferroelectrics and generalization to other magnetic materials with a domain structure).

It is important to stress that it is only meaningful to consider that the coordinates of C_m remain constant as a consequence of the energy conservation law when external magnetic and electric fields act on ferromagnetics and ferroelectrics. When part of a ferromagnetic crystal or ferroelectric is heated above the Curie point or mechanical deformations change the crystal shape, C_m becomes displaced, only conserving the properties described above under the action of external fields.

This reasoning can also be applied to polycrystalline domain structures if we assume that they are correlated systems in which the orientation of the magnetic moments of the domains in one crystal affects the orientation of the magnetic moments of the domains in neighboring crystals, converting the entire bulk of the sample to a self-organizing system.

If instead of a single crystal, a polycrystalline rod magnet (magnetic needle) is suspended by its center of mass, this should exhibit similar behavior in an external nonvarying magnetic field, i.e., C_m should not alter its coordinates relative to the sample.

Otherwise, the energy conservation law will be violated and we would be able to magnetize one half of the magnetic needle more than the other, which is not observed in practice.

Since C_m should have fixed coordinates in an external field of any magnitude, having selected the limiting case when the sample is magnetized to saturation in one direction, we can easily determine the position of C_m. Assuming that small nonferromagnetic inclusions are distributed uniformly in the entire bulk of the magnetic needle, C_m coincides with its geometric center or center of mass.

For various structures using combinations of permanent magnets, ferromagnetic and nonferromagnetic samples, it is first advisable to identify the intercorrelation of the domains in this system by measuring the long-range magnetic fields.[2,3] If this system is observed as a single magnetic dipole in various magnetic states, the coordinates C_m will be fixed regardless of any change in its magnetic state. If this system is observed as several magnetic dipoles, the above reasoning can be applied to each separately.

For our example we selected the particular case when the magnetic domains are oriented strictly parallel or perpendicular to each other. This allowed us to derive the simple relations (1)–(3) which simulate the main phenomenological properties.

However, we can easily establish that any vector system with arbitrarily oriented initial vectors has the same properties if the point of application of the resultant vector does not alter its coordinates for any rotation of the initial vectors.

Consequently, this vector system may be taken as a mathematical model which by different initial orientations of the initial vectors, can simulate all existing and theoretically possible magnetically ordered systems and ferroelectrics.

[1] S. V. Vonsovskiĭ, *Magnetism* [in Russian], Nauka, Moscow (1984).
[2] A. T. Ovakimyan, Military-Scientific Journal of the Ministry of Defense of the Republic of Armenia, No. 2 (1996).
[3] A. T. Ovakimyan, *Behavior of Domain Structures As a Consequence of the Energy Conservation Law*, ArmNIINTI, Paper No. 133-Ap97, deposited 30.04.97.

Translated by R. M. Durham

Self-organized nanosize InP and InAsP clusters obtained by metalorganic compound hydride epitaxy

D. A. Vinokurov, V. A. Kapitonov, O. V. Kovalenkov, D. A. Livshits, and I. S. Tarasov

A. F. Ioffe Physicotechnical Institute, Russian Academy of Sciences, St. Petersburg
(Submitted February 25, 1998)
Pis'ma Zh. Tekh. Fiz. **24**, 1–7 (August 26, 1998)

Results are presented of investigations of the growth of self-organizing nanosize InP and InAsP clusters in an $In_{0.5}Ga_{0.5}P$ matrix. The structure was characterized by low-temperature photoluminescence and transmission electron microscopy. The photoluminescence measurements revealed highly efficient radiative recombination from the quantum dots and indicated that the structures were of good optical quality. The average density and size of the InP clusters, determined from the results of the transmission electron microscope measurements, are 3×10^9 cm^{-2} and 80 nm, respectively. © *1998 American Institute of Physics.* [S1063-7850(98)01708-X]

The spontaneous formation of nanosize clusters during heteroepitaxial growth of highly strained semiconductors is attracting considerable attention because of the possibility of obtaining three-dimensional electron confinement in homogeneous, coherent quantum dots. These structures grown by standard molecular-beam epitaxy (MBE) and vapor-phase epitaxy from metalorganic compounds and hydrides (MOC hydride epitaxy) possess a high degree of quantization and high radiative efficiency mainly because of the lower defect density and contamination compared with structures fabricated by lithographic procedures. The introduction of three-dimensional confinement of electrons, holes, and excitons in these semiconductor microstructures can be used to study new physical effects[1,2] and also to appreciably improve the characteristics of electronic and optoelectronic devices,[3,4] especially semiconductor heterolasers with a quantum-dot active region. It is hypothesized that these heterolasers will exhibit a high differential gain, high characteristic temperature T_0, and appreciably lower threshold currents.[3,5] At present, even the first quantum-dot lasers grown by MBE and MOC hydride epitaxy in an InGaAs/GaAs system have threshold current densities of 40 A/cm^2 ($T_0=430$ K; Refs. 6 and 8) and 60 A/cm^2 ($T_0=530$ K; Refs. 7 and 8).

Most experimental studies have been concerned with methods of obtaining InAs (InGaAs) quantum dots in a GaAs (AlGaAs) matrix. Another interesting research topic is the fabrication of nanosize clusters in an InP/InGaP system.

In the present study, nanosize InP clusters were grown in an $In_{0.5}Ga_{0.5}P$ matrix at reduced pressure using an MOC hydride epitaxy system in a horizontal reactor with an rf-heated substrate holder. The reagents were trimethyl gallium (TMGa), trimethyl indium (TMIn), arsine (AsH_3) (20% in hydrogen), and phosphine (PH_3) (30% in hydrogen). The growth process took place at a temperature of 700 °C and a reactor pressure of 50 mbar. A 500 nm lattice-matched layer of $In_{0.5}Ga_{0.5}P$ was grown on an accurately oriented GaAs(100) substrate followed by the deposition of an InP layer with nominal thicknesses between 0.7 and 15 ML. After annealing for 5 sec in a PH_3 atmosphere, the InP clusters were overgrown with a 50 nm layer of $In_{0.5}Ga_{0.5}P$. The an-

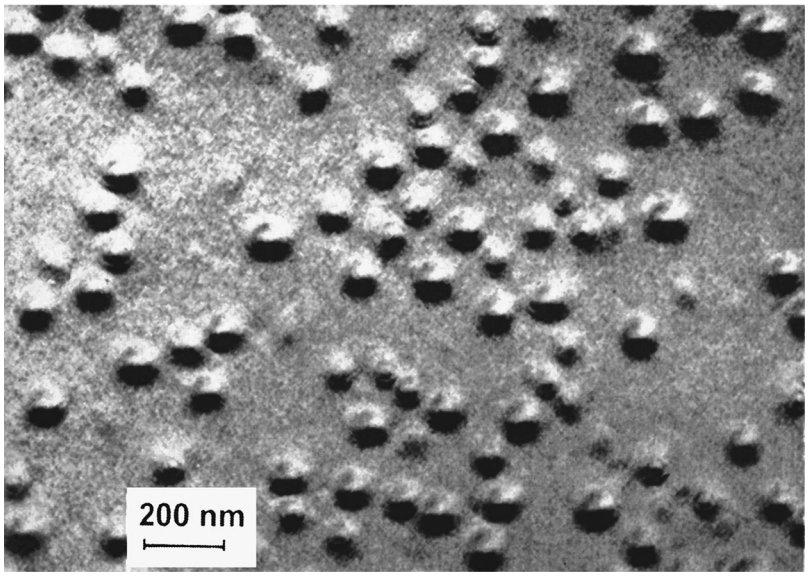

FIG. 1. Transmission electron microscope image of InP clusters with a nominal thickness of 3 ML.

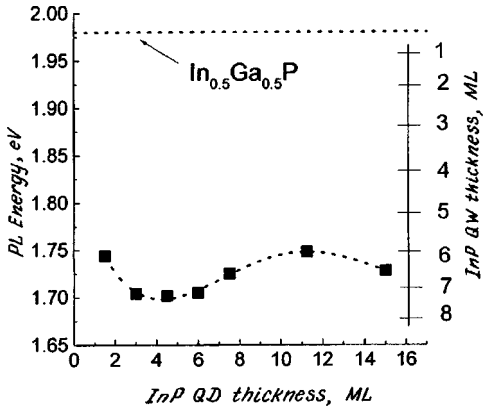

FIG. 2. Position of photoluminescence peak (77 K) from InP quantum dots as a function of the nominal thickness of the deposited InP layer.

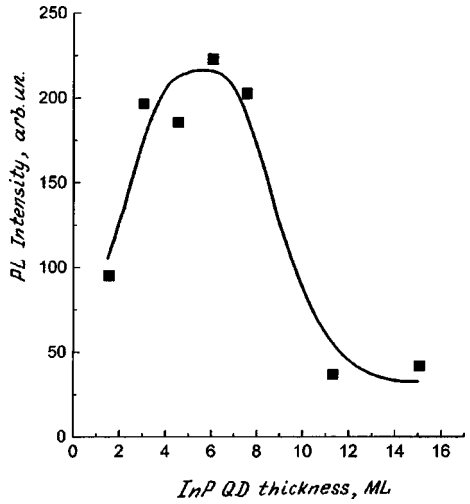

FIG. 3. Intensity of photoluminescence peak (77 K) from InP quantum dots as a function of the nominal thickness of the deposited InP layer.

nealing was carried out to provide conditions for the complete formation of clusters.[9] The nominal growth rates were 1.4 ML/s for the InGaP barriers and 0.7 ML/s for the quantum dots.

The samples were examined by transmission electron microscopy using a high-resolution Philips EM 420 microscope at an accelerating voltage of 120 kV. Figure 1 shows images of nanosize clusters when 3 ML of InP was deposited. The average transverse dimension of the quantum dots is ~ 80 nm and the average density is 3×10^9 cm^{-2}.

Photoluminescence measurements were made using an Ar^+ laser (488 nm) with an excitation density of ~ 50 W/cm^2. As a result of the formation of InP quantum dots, the photoluminescence spectrum reveals a high-intensity peak at 1.2 eV (77 K) (or 1.68 eV at 300 K). The position of the peak remains almost unchanged as the InP quantum dots vary between 2 and 15 ML (Fig. 2), which differs from the systematic decrease in the energy of the photoluminescence peak observed as the layer thickness increases in a quantum well.[10] From this it can be inferred that, in accordance with the Stranski–Krastanow model, three-dimensional clusters develop as far as their critical dimensions which are determined by the equilibrium of the stresses between the matrix and quantum dot materials. The energy position of the photoluminescence peak from the InP clusters theoretically corresponds to a ~ 6–7 multilayer InP quantum well (Fig. 2).

The efficiency of the radiative recombination from the quantum dots is 1.5 orders of magnitude higher than the luminescence from the InGaP barriers and is 30% at 77 K (Fig. 3). The high photoluminescence efficiency demonstrates the extremely high optical quality of these structures and the effective carrier localization in the quantum dots. An increase in the nominal InP thickness above 8 ML causes an abrupt deterioration in the radiative characteristics from the quantum dots, which may be attributed to the evolution of a significant number of dislocations.

These results on the growth of self-organized nanosize clusters of $InAs_xP_{1-x}$ ternary solid solutions in an $In_{0.5}Ga_{0.5}P$ matrix have no analogs in the literature. It was predicted that the addition of arsenic to InP quantum dots would shift their photoluminescence spectrum in the long-wavelength direction. However, in our investigations the position of the photoluminescence peak corresponding to the $InAs_xP_{1-x}$ quantum dots remained constant for all the compositions studied, i.e., having x between 0 and 0.5. Moreover, the position of this peak corresponds to that of the InP quantum dots (Fig. 4). This may be explained by the fact that the average size of the InP quantum dots obtained under different conditions varies between 40 and 100 nm (Refs. 9–11) whereas InAs dots have an average size of 15–30 nm (Refs. 5–8). Thus, the incorporation of arsenic in InP clusters may reduce their

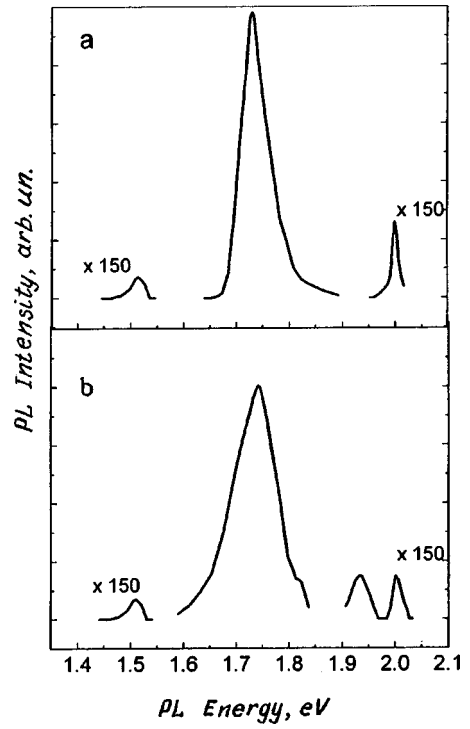

FIG. 4. Photoluminescence spectra (77 K) from: a — InP quantum dots. The nominal thickness of the InP layers is 3 ML; b — $InAs_{0.25}P_{0.75}$ quantum dots. The nominal thickness of the $InAs_{0.25}P_{0.75}$ layer is 3 ML.

size and thereby compensate for the predicted energy shift of the photoluminescence peak.

To sum up, we have grown nanosize InP and, for the first time anywhere in the world, InAsP clusters in an $In_{0.5}Ga_{0.5}P$ matrix. The high photoluminescence efficiency of the self-organized quantum dots indicates that these nanostructures are of high optical quality. The properties of ternary InAsP quantum dots will be the subject of further research.

This work was supported by Project No. 96-2005 under the Russian National Program ''Physics of Solid-State Nanostructures.''

[1] L. Brus, IEEE J. Quantum Electron. **22**, 1909 (1986).
[2] D. S. Chelma and D. A. B. Miller, Opt. Lett. **11**, 522 (1986).
[3] Y. Arakawa and H. Sakaki, Appl. Phys. Lett. **40**, 939 (1982).
[4] H. Sakaki, Jpn. J. Appl. Phys., Part 1 **28**, L314 (1989).
[5] N. Kurstaedter, N. N. Ledentsov, M. Grundmann *et al.*, Electron. Lett. **59**, 1416 (1994).
[6] Zh. I. Alferov, N. A. Bert, A. Yu. Egorov *et al.*, Fiz. Tekh. Poluprovodn. **30**, 351 (1996) [Semiconductors **30**, 194 (1996)].
[7] Zh. I. Alferov, N. Yu. Gordeev, S. Yu. Zaĭtsev *et al.*, Fiz. Tekh. Poluprovodn. **30**, 357 (1996) [Semiconductors **30**, 197 (1996)].
[8] V. M. Ustinov, A. E. Zhukov, A. U. Egorov *et al.*, Inst. Phys. Conf. Ser. **155**, Chap. 7, 557 (1996).
[9] N. Carlsson, W. Seifert, A. Petersson *et al.*, Appl. Phys. Lett. **65**, 3093 (1994).
[10] W. Seifert, N. Carlsson, M.-E. Pistol *et al.*, Appl. Phys. Lett. **67**, 1166 (1995).
[11] O. V. Kovalenko, D. A. Vinokurov, D. A. Livshits *et al.*, in *Proceedings of the International Symposium on Nanostructures: Physics and Technology*, St. Petersburg, 1996, pp. 141–143.

Translated by R. M. Durham

Formation of quasisteady supersonic flow with a pulse-periodic plasma heat source

P. K. Tret'yakov and V. I. Yakovlev

Institute of Theoretical and Applied Mechanics, Siberian Branch of the Russian Academy of Sciences, Novosibirsk

(Submitted February 18, 1998)
Pis'ma Zh. Tekh. Fiz. **24**, 8–13 (August 26, 1998)

An analysis is made of experimental data on the influence of a pulse-periodic optical discharge in a supersonic argon stream on the aerodynamic drag of streamlined objects. The interrelation established between the parameters of the laser radiation and the stream is used to determine the threshold frequency of the laser pulses which determines the transition to quasi-steady-state flow. © *1998 American Institute of Physics.* [S1063-7850(98)01808-4]

In addition to conventional methods of controlling supersonic flows by means of an external power supply (fuel combustion), the possibility of using laser radiation is also being considered.[1,2] Optical breakdown of the gas in the stream results in the formation of a localized high-temperature zone or plasma heat source. A numerical simulation has shown that under certain conditions, a local heat conductor may produce substantial rearrangement of the gas-dynamic structure in flow around objects.[3] Experimental investigations have been confined to studies of transient processes during the interaction between a pulsed heat source and a shock-wave structure ahead of a streamlined object.[4] The lack of experimental investigations of steady-state regimes can be attributed to the requirement for high laser radiation energy parameters which are needed to stabilize the optical discharge in a high-velocity gas stream. In Ref. 4 an attempt was made to use a series of several laser pulses to produce and study steady-state regimes. However, because of the inadequate duration of the entire process, no systematic data were obtained, although the experimental results suggested that quasi-steady-state flow may be achieved by means of a pulsed power supply to the gas stream.

In Ref. 5 an optical discharge in a supersonic stream was stabilized by using pulse-periodic carbon dioxide laser radiation at a high pulse repetition frequency (up to 100 kHz). It was ascertained[2] that the effect of the energy release depends on the frequency and is observed as a change in the aerodynamic drag of streamlined objects. From the experimentally determined frequency dependence of this parameter it was concluded that quasi-steady-state flow is established at a frequency above 50 kHz. However, no detailed analysis was made of the conditions and mechanisms determining the nature of the flow. The aim of the present study is to use the experimental results to examine the main factors and conditions responsible for the transition to steady-state supersonic flow with a pulse-periodic plasma heat source.

A supersonic argon stream was produced in an aerodynamic system[2] which gives Mach number 2 with the following initial parameters: pressure 0.45 MPa and temperature 293 K. In the working frequency range of 12.5–100 kHz, the average powers of the laser pulses were between 113 and 16 kW and the power densities were $(3.7-0.5)\times 10^{12}$ W/m^2, although the real peak values were two or three times higher than the average for ≈ 0.3 μs when the total pulse length was 1.2 μs (Ref. 6). The generalized results of the measurements[2] of the change in the relative aerodynamic drag C/C_0 (where C_0 is the measured parameter in the absence of a plasma heat source) of streamlined objects are plotted by curve *1* in Fig. 1. This parameter decreases as the pulse repetition frequency f increases and remains almost constant at ≈ 0.55 for $f > 50$ kHz, which indicates that steady-state flow is established.

Assuming that the energy is released instantaneously at a point in a gas stream with the velocity u, the condition for the establishment of a steady-state wavefront ahead of a pulse-periodic optical discharge was formulated in Ref. 7 in the form $R(t_0)=ut_0$, where R is the radius of a spherical shock wave and t_0 is the time interval during which it is displaced downstream by the distance R. The well-known[8] self-similar solution $R(t)=(E/\alpha p)^{1/5}t^{2/5}$, where E is the pulse energy, ρ is the initial gas density, and α is a quantity which depends on the specific heat ratio γ, is used to determine the threshold frequency $f_0=1/t_0$.

The experimental results showed that the energy release region exhibits strong luminescence, since it is appreciably elongated along the axis of the stream. The measured length of this region depends on the observation conditions, which are characterized by numerous superposed luminescence flashes. For the minimum exposure time using dense filters, this length is 5–7 mm. For these reasons the experimental determination of the length L of the heat source may lead to appreciable error in the measured results. However, if we take into account the well-known[9] mechanism for the evolution of an optical discharge whereby radiation is absorbed beyond the front of an optical detonation wave, this parameter can be calculated from the ratio $L=\int_0^\tau V dt$, where τ is the laser pulse length and V is the velocity of the front, $V=[2(\gamma^2-1)J/\rho]^{1/3}$. The power density J of the radiation was determined from the experimentally recorded energy characteristics and dynamics of the laser pulses with allowance for the focusing parameters. In the frequency range 12.5–100 kHz we obtain $L=12-6.2$ mm, respectively (in the range of front velocities 11–5.7 m/s). An increase in the length of the luminescence zone with decreasing frequency

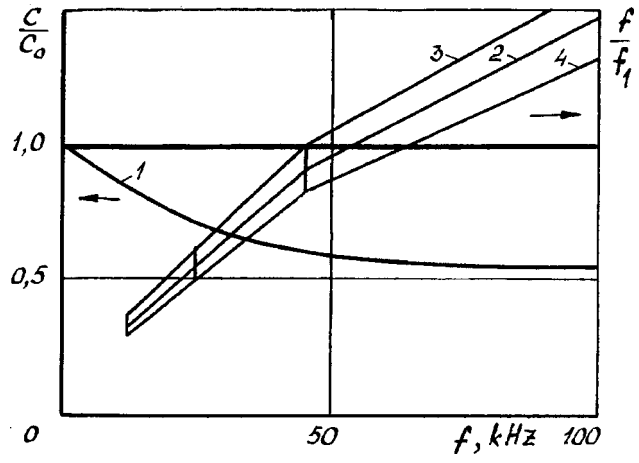

FIG. 1. Experimental C/C_0 (*1*) and calculated f/f_1 (*2*, *4*) data as a function of the pulse repetition frequency, $\gamma=1.2$ (*2*), 1.25 (*3*), and 1.15 (*4*).

was also recorded experimentally as a result of an increase in the pulse energy.

Thus, an extended region of plasma forms periodically almost ''instantaneously'' ($\tau \ll 1/f$, where $1/f$ is the time interval between the pulses and is 10 μs or longer) in the gas and by the time of the next pulse this has moved downstream over the distance u/f. Thus, the condition for the transition to quasi-steady-state flow may be expressed by equating this scale factor u/f to the length of the plasma heat source: $u/f_1=L$, from which the threshold frequency f_1 is determined. Figure 1, curve *2* gives the calculated results in the form of the relative values f/f_1 (for $\gamma=1.2$). Data are also plotted for $\gamma=1.25$ (curve *3*) and 1.15 (curve *4*) which according to the estimates may correspond to the parameters of state of an argon plasma in the optical breakdown range. This range of γ is near but within the limits of the boundary determining the stability of the shock waves.[10] The data shown in the figure indicate that $f/f_1=1$ golds in the frequency range 45–65 kHz. This correlates with the experimental results (curve *1*) which indicate that a steady-state effect is established in this frequency range. An analysis of the possible influence of axial expansion of the heated gas also showed that an increase in the length of the heat source in the interpulse period would reduce f_1 and satisfy the condition $f/f_1=1$ at low frequencies, where the frequency dependence of the measured parameter C/C_0 is observed. Thus, the experimental results indicate that this effect is weak.

This work was supported financially by the Russian Fund for Fundamental Research under Grant No. 96-01-01947.

[1] I. V. Nemchinov, V. I. Artem'ev, V. I. Bergelson *et al.*, Shock Waves No. 4, 35 (1994).
[2] P. K. Tret'yakov, A. F. Garanin, G. N. Grachev *et al.*, Dokl. Akad. Nauk SSSR **351**, 339 (1996) [Phys. Dokl. **41**, 556 (1997)].
[3] P. Yu. Georgievskiĭ and V. A. Levin, Pis'ma Zh. Tekh. Fiz. **14**, 684 (1988)] [Sov. Tech. Phys. Lett. **14**, 503 (1988)].
[4] V. Yu. Borzov, V. M. Mizaĭlov, I. V. Rybka *et al.*, Inzh.-Fiz. Zh. **66**, 515 (1994).
[5] P. K. Tret'yakov, G. N. Grachev, A. I. Ivanchenko *et al.*, Dokl. Akad. Nauk SSSR **336**, 466 (1994) [Phys. Dokl. **39**, 415 (1994)].
[6] G. N. Grachev, A. G. Ponomarenko, A. L. Smirnov *et al.*, Proc. SPIE **2702**, 407 (1996).
[7] L. N. Myrabo and Yu. P. Raizer, in *Proceedings of the 25th Plasma Dynamics and Lasers Conference*, Colorado Springs, 1994, AIAA 94-2451, pp. 1–13.
[8] L. I. Sedov, *Similarity and Dimensional Methods of Mechanics* (Academic Press, New York, 1959).
[9] Yu. P. Raizer, *Gas Discharge Physics* (Springer-Verlag, New York, 1991).
[10] G. A. Tarnavskiĭ and V. P. Fedosov, Chisl. Metod. Mekh. Splosh. Sred. **17**(14), 150.

Translated by R. M. Durham

Domain nucleation in thermomagnetic memory systems near the Curie point

G. E. Khodenkov

Institute of Electronic Control Machines, Moscow
(Submitted February 18, 1998)
Pis'ma Zh. Tekh. Fiz. **24**, 13–17 (August 26, 1998)

The approximation of Landau second-order phase transitions for ferromagnetics near the Curie point is used for a numerical determination of the two-dimensional microstructure which forms the basis of a data-storage domain. This structure and its lower level of the spectrum of small oscillations are strongly delocalized. Depending on the recording regimes, this may be responsible for the severe irregularity of the domain wall shape sometimes observed or the formation of ring domains. © *1998 American Institute of Physics.* [S1063-7850(98)01908-9]

In the simplest thermomagnetic memory system (bubble domains), information is recorded by heating a section of magnetic film to the Curie temperature with a laser beam. Unfortunately, this method is not optimum, especially since non-optimum recording regimes and/or variation in the properties of the film gives rise to bubble domains with highly irregular walls and even ring domains. The aim of the present study is to identify the reason for this effect, which is undesirable from the point of view of the signal-to-noise ratio, by studying domain nucleation.

The second stage of nucleation, in which an already formed 180° Bloch domain wall undergoes a shift, has been well studied (see the review of relevant ideas and results presented in Ref. 1). In this stage however, it is extremely difficult to explain the formation of large-scale irregularities of the domain-wall shape or ring domains. In this context we note that the importance of allowing for the first stage of nucleation and its kinetics has been indicated on various occasions (see in particular, Refs. 2–4). It will be shown subsequently that the micromagnetic structure formed at this stage and the lower level of the spectrum of small oscillations are highly delocalized, which may be responsible for the formation of the irregularities.

When a ferromagnetic film cools, a local temperature region $T \leqslant T_c$ (T_c is the Curie point) inevitably forms where the standard thermodynamic potential can be applied

$$\Phi = \int dV \left[\frac{\alpha}{2} (\nabla M)^2 + AM^2 + BM^4 \right]. \tag{1}$$

Here M is the magnetization, $\alpha > 0$ is the exchange rigidity, $A = a(T - T_c)$, where $a > 0$ and $B > 0$ are the coefficients of the expansion of the potential near the Curie point T_c. It is assumed that the spatial dimension of the region described by Eq. (1) is fairly large and outside this region Eq. (1) must be supplemented by the energy of magnetic anisotropy, and so on. We also note that in the spatially one-dimensional case, Eq. (1) yields the Zhirnov domain wall:

$$M(x) = \sqrt{|A|/2B}\ \tanh(\sqrt{|A|/\alpha}\, x), \tag{2}$$

in which the transition between domains (along the x axis) is achieved by variation in the magnitude of the magnetization vector but without it rotating.

Let us assume that the magnetization vector has a single tangential component which only depends on the radial coordinate so that div $\mathbf{M} = 0$. The magnetization dynamics obeys the Landau–Khalatnikov equation, which we write in cylindrical coordinates:

$$\frac{\partial m}{\partial t} = \frac{2|A|}{\tau_\parallel} [(\rho m')'/\rho + m/\rho^2 + m - m^3]. \tag{3}$$

Here $\tau_\parallel$ is the longitudinal relaxation time; the dimensionless radial coordinate ρ and the magnetization $-1 \leqslant m(\rho) \leqslant 1$ are measured in units of $\sqrt{\alpha/2|A|}$ and $\sqrt{|A|/2B}$, respectively.

The results of a numerical integration of Eq. (3) are plotted in Fig. 1. Curve *1* gives the static solution $m_0(\rho)$ obtained numerically. At the center of the domain we find $m_0(\rho \to 0) \to 0.58\rho$, whereas $m_0(\rho \to \infty) \to 1 - 1/2\rho^2$. The plotted dependence and the equation itself are universal and describe many phenomena (in particular, the vortex filaments in an almost ideal Bose liquid, antiferromagnetic disclinations,[5] and so on).

In order to determine the time evolution of this vortex structure, we determine the spectrum of small oscillations of the problem (3) linearized with respect to the small amplitudes, $m(\rho,t) = m_0(\rho) + \delta m(\rho) \exp(-Et)$:

$$E\,\delta m = -(\rho\,\delta m')'/\rho + V(\rho)\,\delta m,$$
$$V(\rho) = 1/\rho^2 - 1 + 3m_0^2(\rho). \tag{4}$$

The potential $V(\rho)$ and the lower eigenfunction of the discrete spectrum $\delta m_0(\rho)$ are plotted by curves *2* and *3* in Fig. 1, respectively. The eigenvalue of this level is

$$E_0 = 1.627 \ldots, \tag{5}$$

where $\delta m_0(\rho)$ has the asymptotic form $\delta m_0(\rho \to \infty) \sim \exp(-\sqrt{2 - E_0}\rho)/\sqrt{\rho}$ and $\delta m_0(\rho \to 0) \sim \rho$. The spatial scale near the Curie point is large $\sim 1/\sqrt{T - T_c}$ so that the structures shown are highly delocalized. For comparison Fig. 1 also gives the soft mode of the Zhirnov domain wall spectrum (2) $\sim 1/\cosh^2(x/\sqrt{2})$ (see the dashed curve near the peak *3*).

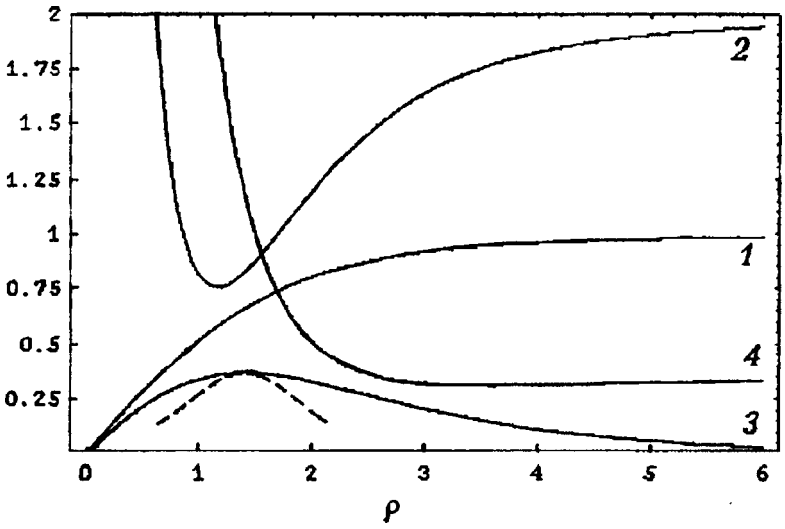

FIG. 1.

We shall examine the possible existence of additional discrete levels below the boundary of the continuous spectrum $E_\infty=2$. The substitution $\delta R=\sqrt{\rho}\,\delta m(\rho)$ eliminates the first derivative from Eq. (4):

$$(E-E_0)\,\delta R=\hat{L}^+\hat{L}^-\,\delta R, \tag{6}$$

where the operators are $\hat{L}^\pm=\pm\partial/\partial\rho+\delta R_0'/\delta R_0$ and $\delta R_0=\sqrt{\rho}\,\delta m_0(\rho)$ is a known function. Introducing into Eq. (6) the variable $x=\hat{L}^-\,\delta R$, we obtain a one-dimensional Schrödinger equation from which the level (5) is eliminated:

$$(E-E_0)\chi=-\chi''+V^*(\rho)\chi,$$

$$V^*(\rho)=2(\delta R_0'/\delta R_0)^2-\delta R_0''/\delta R_0. \tag{7}$$

The new potential $V^*(\rho)$ (see curve *4* in Fig. 1) has a very shallow, gently sloping minimum. The marked asymmetry of the potential $(V^*(\rho\to 0)\to 15/(4\rho^2)$ and $V^*(\rho\to\infty)\to 2-E_0)$ means that the existence of a level additional to (5) is extremely unlikely.

The evolution of the vortex structure $m_0(\rho)$ during cooling is given by Eq. (3) (with the inclusion of uniaxial anisotropy, magnetostatic interaction, and so on in Eq. (1)) and by the heat conduction equation. Possible scenarios depend on the laser pulse parameters and on the technological parameters of the magnetooptic disk, but allowance for these is outside the scope of the present study. However, there is no doubt that a major role in the kinetics will be played by the lower discrete level (5) which, as can be seen from Fig. 1, has a broad ring-shaped profile. It is thus important to select the cooling regime so that its characteristic time does not exceed the time needed for spatial establishment of the mode (5) which, according to Eq. (3), is $\sim\tau_\parallel/(2E_0|A|)$. Depending on the following conditions, violation of this condition may lead to the formation of a ring domain or (as a result of interaction with defects) the formation of a broad irregular region bordering the data storage domain. Under recording conditions, the region of validity of Eqs. (1) and (3) is limited by the size of the temperature field $T\leqslant T_c$ created by the laser beam. To suppress undesirable effects, the energy transferred by the beam and the size of the active region (1) should not be too large and the cooling should be fairly rapid.

The author is grateful to the late Yu. V. Starostin for introducing him to the problems of thermomagnetic recording.

[1] V. V. Randoshkin and A. Ya. Chervonenkis, *Applied Magnetooptics* [in Russian], Energoatomizdat, Moscow (1990), 320 pp.
[2] H. P. D. Shieh and M. Kryder, J. Appl. Phys. **61**, 1108 (1987).
[3] M. Takahashi, T. Niihara, and N. Ohta, J. Appl. Phys. **64**, 262 (1988).
[4] T. Thompson and K. O'Grady, J. Phys. D **30**, 1567 (1997).
[5] B. A. Ivanov, V. E. Kireev, and V. P. Voronov, Fiz. Nizhk. Temp. **23**, 845 (1997) [Low Temp. Phys. **23**, 635 (1997)].

Translated by R. M. Durham

Increase in the modulation of an acoustic wave scattered from weakly stable vibrational states of bubbles

A. O. Maksimov

Institute of Marine Technology Problems, Far-Eastern Branch of the Russian Academy of Sciences
(Submitted March 4, 1998)
Pis'ma Zh. Tekh. Fiz. **24**, 18–23 (August 26, 1998)

A theoretical analysis is made of the mechanism for nonlinear diagnostics of gas inclusions in a liquid. It is shown that the modulation of the scattered acoustic wave amplitude increases appreciably near critical values of the pump field corresponding to weakly stable bubble states.
 [S1063-7850(98)02008-4]

The need to estimate the size and spatial distribution of gas inclusions in a liquid arises in studies of natural objects and in numerous industrial, medical, and ecological applications.[1] Two factors, the resonant nature of the interaction and the appreciable compressibility of the gas in the bubble, ensure that acoustic methods have priority in the diagnostics of these objects, which are examples of nonlinear oscillators. The simplest manifestations of nonlinear pulsations involve the excitation of higher harmonics $2\omega_p$, $3\omega_p$, ... (Ref. 2). Recording these harmonics in the backscattered signal can reveal the contribution of bubbles against the background of other (solid) inclusions. More refined diagnostic methods involve two-frequency sonic irradiation of the medium.[3–7] In these techniques the acoustic field consists of a high-frequency signal wave (generally exceeding the resonant frequencies of the bubbles) and a relatively low-frequency pump wave exciting resonant oscillations of the bubbles. Linear methods of acoustic spectroscopy of gas inclusions[8] based on using amplitude-modulated and phase-manipulated signals have also been improved. In addition to the excitation of higher harmonics and Raman frequencies, nonlinear oscillations of bubbles are also observed in more complex effects caused by bifurcations of the dynamic states of this nonlinear oscillator.[9–11]

In the present paper an analysis is made of the interaction between a high-power amplitude-modulated acoustic wave $P_p=0.5\{(A_p+A_i\sin\omega_i t)\exp[i(k_p x-\omega_p t)]+\text{c.c.}\}$ with a cloud of bubbles. We shall assume that the conditions $A_p \gg A_i$ and $\omega_p \gg \omega_i$ are satisfied between the pump amplitude and frequency A_p, ω_p and between the modulation amplitude and frequency A_i, ω_i. The nonlinear oscillation regime of the various inclusions is defined by the high-power pumping. Weak modulation will only have a significant effect near those dynamic states of bubbles which become unstable (at least one of the two Lyapunov exponents vanishes). Then, as a result of energy being transferred from the field to the weakly stable oscillation modes excited by the modulation component, the percent modulation of the scattered signal may increase appreciably and serve as a diagnostic for the bubbles.

The quantitative analysis of the effect will be based on an analysis of the Rayleigh–Plesset equation which describes the oscillations of a bubble in the pressure field P_p

$$R\ddot{R}+\frac{3}{2}\dot{R}^2+\frac{P_0}{\rho_0}\left[1-\left(\frac{R}{R_0}\right)^{3\gamma}\right]+2\delta R_0\dot{R}=\frac{P_p}{\rho_0}, \tag{1}$$

where γ is the polytropic index, δ is the damping which effectively allows for the dissipative processes of viscosity and heat conduction, and also for the radiation losses, P_0, ρ_0, and R_0 are the equilibrium pressure and density of the liquid and the bubble radii. The approximate solution (2) is constructed by a standard method (see, for example, Ref. 12). Near the main resonance $|\omega_p-\Omega_0|\ll\omega_p$ the asymptotic series has the form $(R-R_0)/R_0=0.5(a\exp(-i\omega_p t+i\varphi)+\text{c.c.})+\varepsilon u_1(a,\varphi)+\varepsilon^2 u_2(a,\varphi)+\ldots$ (see Ref. 13), where $\Omega_0=(3\gamma P_0/\rho_0 R_0^2)^{1/2}$ is the natural frequency of the bubble, and ε is a dimensionless small parameter introduced to denote the order of the nonlinear terms. The slowly varying amplitude a and phase φ of the oscillations are determined from a system of ''reduced'' equations derived from the constraint that the expansion contains no secular terms. Allowance for nonlinear terms through third order in Eq. (1) yields the following equation for $z=a\exp(i\varphi)$:

$$\dot{z}=-\delta z-i[\omega_p-\Omega_0+k\Omega_0 a^2]z+i\frac{[A_p+A_i\sin(\omega_j t)]}{6\gamma P_0\Omega_0^{-1}}, \tag{2}$$

where $\kappa=(6\gamma^2-3\gamma-2)/16$ and Eq. (2) was derived assuming that $\omega_i \leqslant \delta$. In the absence of a modulation term, the structure of the solution (3) is well-known. The amplitude a_* and phase ϑ_* of the steady-state oscillations ($\dot{a}=0$, $\dot{\vartheta}=0$) are described by the expressions[12,9]

$$a_*^2[(\omega_p-\Omega_0+\kappa\Omega_0 a_*^2)+\delta^2]=\frac{A_p^2}{36\gamma^2 P_0^2\Omega_0^{-2}},$$

$$\cos\varphi_*=\frac{6\gamma(\delta/\Omega_0)P_0 a_*}{A_p}. \tag{3}$$

Figure 1 gives the amplitude of the steady-state oscillations a_* as a function of the determining parameters, the detuning $\omega_p-\Omega_0$ and the pump amplitude A_p. Outside the region bounded by the curves B_1 and B_2 the dynamic system (3) (in

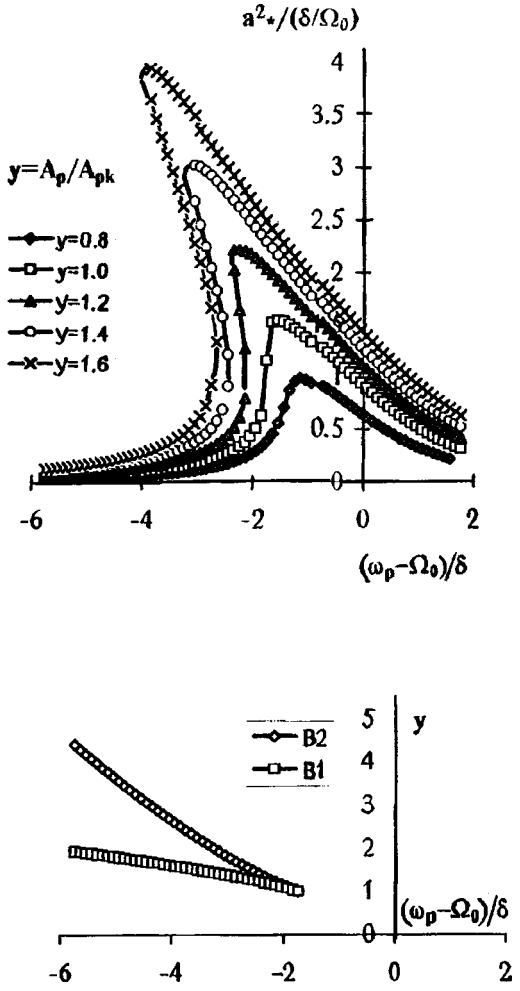

FIG. 1.

the absence of a modulation component) has only one stable state, which corresponds to a simple node on the phase plane a,ϑ. Inside the region bounded by curves B_1 and B_2 there exist three steady states: two stable states corresponding to nodes, and one unstable state corresponding to a saddle. On the bifurcation curves B_1 and B_2, the node and saddle points merge. The point $\mathcal{F}(\omega_{pk}-\Omega_0)=-\sqrt{3}-\delta$, $A_{pk}^2=(32\sqrt{3}/\kappa)\times(\delta/\Omega_0)^3P_0^2)$ is a singular point at which all the singular points, two nodes and the saddle, merge.

Using the ability of nonlinear systems to amplify weak signals near the dynamic stability threshold,[14] we shall analyze the influence of the modulation component near the point $\mathcal{F}$, which is the threshold for bistability. For threshold values of the determining parameters one of the two Lyapunov exponents of the dynamic system (2) (neglecting modulation) vanishes because fast and slow components can be identified in the description of the time evolution. For fairly low-frequency modulation $\omega_i \ll \delta$ the subordination principle[15] can eliminate the fast variable whose relaxation time is determined by $1/\delta$ and yields a single equation for the slow variable $\eta=a\sin\vartheta-a_k\sin\vartheta_k$, where $a_k\sin\vartheta_k=[(\sqrt{3}/2)(\delta/\kappa\Omega_0)]^{1/2}$.

$$\frac{d\eta}{dt}=\left[\frac{\Delta A}{2\Omega_0\rho_0R_0^2}\Delta\Omega\left(\frac{\delta}{2\sqrt{3\kappa\Omega_0}}\right)^{1/2}\right]-\Delta\Omega\frac{\eta}{\sqrt{3}}$$
$$-\frac{4}{3\sqrt{3}}\kappa\Omega_0\eta^3+\frac{A_i\sin\omega_it}{6\gamma P_0\Omega_0^{-1}}. \tag{4}$$

Equation (4) contains deviations of the determining parameters from the critical values, $\Delta A=A_p-A_{pk}$, $\Delta\Omega=(\omega_p-\Omega_0)+\sqrt{3}\delta(|\Delta\Omega|\ll\delta,|\Delta A|\ll A_{pk})$. Here we shall analyze the simplest solution of Eq. (4) which corresponds to such a slow modulation frequency $(\omega_i/\Omega_0)^3\ll(A_i/6\gamma P_0)$ that to leading order $d\eta/dt=0$ holds and the quasisteady oscillation amplitudes will be described by the formulas (4) with the substitution $A_p\Rightarrow[A_p+A_i\sin\omega_it]$.

Since the scattering cross section is $\sigma_s\sim a^2$, the determination of the amplitude modulation in the diverging wave reduces to finding the explicit form of the solution of the algebraic (cubic) equation (3). Near the bistability threshold for $\Delta\Omega\geqslant 0$ we have

$$a^2=\left(\frac{8}{3\sqrt{3}}\frac{\delta}{k\Omega_0}\right)\left\{\frac{1}{4}-\frac{\Delta\Omega}{4\sqrt{3\delta}}-\frac{\mu}{2\sqrt{(3)}+\nu}\right\},$$
$$\mu\equiv\frac{\Delta A+A_i\sin(\omega_it)}{A_{pk}},\quad \nu=B_++B_-, \tag{5}$$
$$B_\pm=\frac{3\sqrt{3}}{8}\left(\frac{2}{3}\right)^{1/3}\left\{\left(\frac{\Delta\Omega}{\delta}+\frac{4}{\sqrt{3}}\mu\right)\pm\left[\left(\frac{\Delta\Omega}{\delta}+\frac{4}{\sqrt{3}}\mu\right)^2\right.\right.$$
$$\left.\left.+\frac{2}{9\sqrt{3}}\left(\frac{\Delta\Omega}{\delta}\right)^3\right]^{1/2}\right\}^{1/3}. \tag{6}$$

For $|\Delta A|\ll A_i$, $\Delta\Omega_0/\delta\ll A_iA_{pk}$ the value of the modulation component $a_m\sim(\delta/\kappa\Omega_0)^{1/2}[(A_i/A_{pk})\sin(\omega_it)]^{1/3}$ considerably exceeds its value far from the threshold $(|\Delta A|\sim A_{pk},\Delta\Omega_0/\delta)\sim 1$, namely, $a_m\sim(\delta/\kappa\Omega_0)^{1/2}[(A_i/A_{pk})\sin(\omega_it)]$.

For $\Delta\Omega<0$ the changes in the oscillation amplitude in the region of bistability $[(\Delta\Omega/\delta)+(4\mu/\sqrt{3})]^2+(2/9\sqrt{3})\times(\Delta\Omega/\delta)^3\leqslant 0$ will be accompanied by hysteresis effects. However, near the threshold the size of this region is small (compared with the amplitude of the variation of the external field $|\Delta A|\ll A_i$)) and the modulation component of the oscillations on the time interval corresponding to intersection of the region of bistability is also small. For this reason formula (5) fairly accurately describes the modulation of the scattered field near the threshold and for $\Delta\Omega<0$.

Thus, near the threshold for bistability of dynamic bubble states slow amplitude modulation of the pump field causes a considerable increase and significant nonlinear modulation of the scattered field. This observation provides new possibilities for the diagnostics of gas inclusions in a liquid.

[1] T. G. Leighton, *The Acoustical Bubble* (Academic Press, London, 1994).
[2] E. A. Zabolotskaya and S. I. Soluyan, Akust. Zh. **18**, 472 (1972) [Sov. Phys. Acoust. **18**, 396 (1972)].
[3] B. M. Sandler, D. A. Selivanovskiĭ, and A. Yu. Sokolov, Dokl. Akad. Nauk SSSR **260**, 1474 (1981).
[4] V. L. Newhouse and P. M. Shanker, J. Acoust. Soc. Am. **75**, 1473 (1984).

[5] T. G. Leighton, R. J. Lingard, and J. E. Field, Ultrasonics **29**, 319 (1991).
[6] T. G. Leighton, A. D. Phelps, D. G. Ramble, and D. A. Sharpe, Ultrasonics **34**, 661 (1996).
[7] A. O. Maksimov, Ultrasonics **35**, 79 (1997).
[8] V. A. Bulanov, Pis'ma Zh. Tekh. Fiz. **21**(15), 67 (1995) [Tech. Phys. Lett. **21**, 616 (1995)].
[9] A. O. Maksimov, Zh. Tekh. Fiz. **56**, 185 (1986) [Sov. Phys. Tech. Phys. **31**, 108 (1986)].
[10] A. O. Maksimov, Zh. Tekh. Fiz. **58**, 822 (1988) [Sov. Phys. Tech. Phys. **33**, 500 (1988)].
[11] A. O. Maksimov, Akust. Zh. **35**(4), 91 (1989) [Sov. Phys. Acoust. **35**, 53 (1989)].
[12] A. H. Nayfeh, *Introduction to Perturbation Techniques* (Wiley, New York, 1981; Mir, Moscow, 1984, 535 pp).
[13] A. Prosperetti, J. Acoust. Soc. Am. **56**, 878 (1974).
[14] K. Weisenfeld and B. McNamara, Phys. Rev. A **33**, 629 (1986).
[15] H. Haken, *Synergetics: An Introduction*, 3rd ed. (Springer-Verlag, Berlin, 1983; Mir, Moscow, 1985, 424 pp.).

Translated by R. M. Durham

Photoluminescence and degradation properties of carbonized porous silicon

B. M. Kostishko, Sh. R. Atazhanov, and S. N. Mikov

Ulyanovsk State University
(Submitted March 10, 1998)
Pis'ma Zh. Tekh. Fiz. **24**, 24–30 (August 26, 1998)

A promising new method of modifying the spectral characteristics of porous silicon and stabilizing its photoluminescence is proposed using high-temperature carbonization. Investigations have shown that carbonized samples exhibit stable photoluminescence and the spectral peak is shifted into the rf–blue range. © *1998 American Institute of Physics.*
[S1063-7850(98)02108-9]

Porous silicon, whose intense photoluminescence in the visible was discovered by Canham[1] in 1990, promised to be the most useful material in optoelectronics found in recent years. However, the light-emitting properties of porous silicon were found to vary substantially with the residence time in an oxygen-containing medium (the so-called aging effect[2]) and under various external influences, such as thermal annealing,[3] laser irradiation,[4] electrons,[5,6] and so on. It is thus fairly important to stabilize the photoluminescence of porous silicon. At present this is done mainly by rapid thermal oxidation[7] or by thermal vacuum annealing.[8]

Here we report an investigation of the spectral and degradation characteristics of porous silicon modified by fast high-temperature carbonization.

The porous silicon samples were prepared using phosphorus-doped (100)-oriented silicon wafers with resistivity $\rho = 2.4\ \Omega$cm ($N_d = 1.5\times 10^{15}$ cm^{-3}). The porous silicon was formed using standard technology by electrochemical etching in an electrolyte composed of 48% hydrofluoric acid and ethanol in the ratio 1 : 1. The etching time was 40 min at a current density of 20 mA/cm^2. The emission of the initial porous silicon was bright red with a maximum spectral intensity near 1.7 eV.

The freshly prepared porous silicon samples were placed in a reactor in which carbonization was carried out as follows: low-temperature purification of the reactor at 400 °C for 5 min in an argon stream was followed by annealing for 5 min at 700 °C in a hydrogen stream, with final carbonization at $T_C = 100$–1200 °C for $t_C = 2$–4 min in a mixture of carbon-containing gas (CCl_4) and carrier gas (hydrogen). During the carbonization process, part of the sample was covered with a mask of boron-doped single-crystal silicon. The surface layer was also doped with boron at a concentration $C_B \approx 10^{18}$ cm^{-2}. This procedure is used to fabricate buffer layers in heteroepitaxial 3C–SiC/Si structures (Ref. 9). The luminescence from the carbonized samples was whitish-blue.

The composition of the buffer layers grown on the single-crystal substrates of control samples was analyzed quantitatively by electron Auger spectroscopy using an 09IOS-10-005 spectrometer. A layer-by-layer Auger analysis revealed that near the surface the carbon concentration was 15% and decreased continuously to zero over the thickness of the buffer layer (100–150 Å). No traces of oxygen were detected in the samples. The ratio of carbon and silicon in the carbonized porous silicon remained constant even at depths greater than 0.4 μm. This indicates that the quantum filaments of silicon were not destroyed by the high-temperature annealing and an interface supersaturated with carbon atoms was formed at these filaments.

The photoluminescence spectra of porous silicon samples carbonized at various temperatures, shown in Fig. 1, were obtained at room temperature using a DFS-52 spectrometer. An LGN-409 He–Cd laser at 325 nm was used for excitation. The cw radiation power did not exceed $P = 5$ mW/cm^2 which, according to the published data,[8] eliminates thermal processes at the surface of the porous silicon.

It can be seen from Fig. 1 that for the section of the sample covered by the mask which was annealed at 100 °C for 2 min (subsequently called sample No. 1) a low-intensity peak was observed near 2.4 eV in addition to the photoluminescence characteristic of freshly prepared porous silicon (curve *1*). However, the initial peak did not appear on the section without the mask (curve *2*). The photoluminescence spectrum changed substantially with two distinct peaks being observed near 2.4 eV (peak *A*) and 1.8–1.9 eV (peak *B*). The porous silicon carbonized at 1200 °C for 4 min (subsequently called sample No. 2) had similar photoluminescence spectra, where the ratio of the intensities of the high-energy peak *A* to the low-energy peak *B* increased with annealing temperature from 1.6 at 1000 °C to 2.6 at 1200 °C. For the buffer layers formed on single-crystal substrates with the initial carbonization parameters, absolutely no photoluminescence was observed.

In our view, the photoluminescence spectra of the carbonized porous silicon changed because during the high-temperature annealing in the presence of CCl_4, the interface supersaturated with carbon atoms contains a single-crystal silicon carbide (SiC) phase in addition to the amorphous phase. Then, in accordance with the published data,[10] the peak at 2.4 eV can be identified as an impurity radiative transition in the conduction band: a deep boron acceptor level in SiC. The low-energy *B* band may be attributed to the appearance of new radiative transitions and to a reduction in the size of the single-crystal regions of silicon quantum fila-

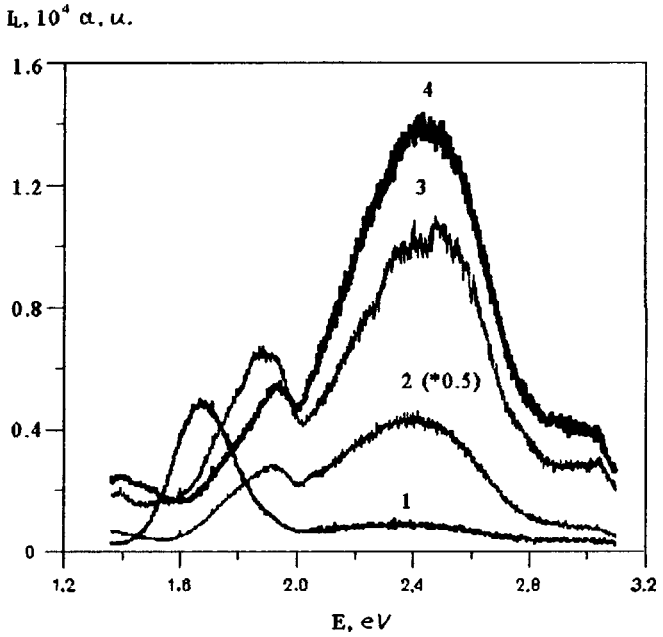

FIG. 1. Photoluminescence spectra of porous silicon carbonized at $T_C=1000$ °C for 2 min — curves *1* and *2*, and at $T_C=1200$ °C for 4 min — curves *3* and *4*. Spectra *1* and *3* were obtained with sections covered by a mask during carbonization. For convenience the values on curve *2* were halved.

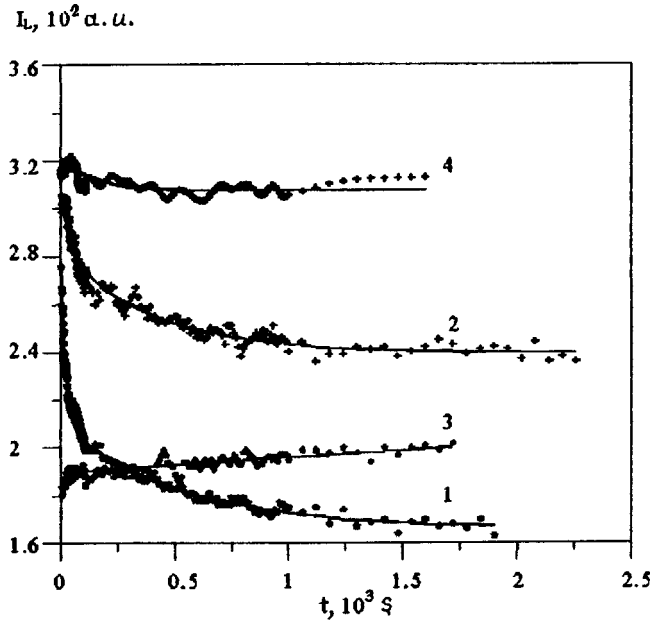

FIG. 2. Intensity of the blue–green photoluminescence of carbonized porous silicon as a function of the laser irradiation time. The numbering of the curves corresponds to that in Fig. 1. The points give the experimental data and the curves give the results of the calculations using Eq. (1).

ments as a result of the growth of silicon carbide on the inner walls of the pores. In this last case, the observed shift of the peak from 1.7 eV by 0.2 eV in the short-wavelength direction according to the data given in Ref. 11 implies that during annealing the average sizes of the silicon quantum regions decreased from 30 to 20 Å.

The photostimulated evolution of the photoluminescence of carbonized samples under the action of cw laser irradiation was investigated in the red and in the blue–green part of the spectrum. Figure 2 gives the photoluminescence intensity as a function of the time of exposure to He–Cd laser irradiation ($P=20$ mW/cm^2) in the most interesting, short-wavelength range.

In terms of the theory developed in Refs. 12–14, the behavior of the curves plotted in Fig. 2 is described by a photostimulated change in the number of centers of radiative exciton annihilation. Their concentration is determined by the number of hydrogen, carbon, and oxygen components passivating the pore walls. The change in the composition of the surface may be described by a system of rate equations[13,14] whose solution can yield an equation for the photostimulated quenching of the porous silicon photoluminescence in the general form

$$I_L=A_L(B_1+B_2\exp(-k_1t)+B_3\exp(-k_2t) -\exp(-k_3t)). \quad (1)$$

Here k_1 and k_2 are the rate constants of the photodestruction reactions of the hydrogen and carbon groups, k_3 is the rate of formation of oxygen-containing components, and A_L is a dimensional constant, The values of the pre-exponential factors in Eq. (1) depend on the reaction rates, the total concentration of adsorption sites, and the initial concentrations of atoms passivating the pore surface.

In order to determine the change in the rate of degradation of the porous silicon photoluminescence after carbonization, the experimental data plotted in Fig. 2 were approximated by Eq. (1) The results of computer fitting are given by the curves, which fairly accurately describe the experimental points. An analysis of the change in the degradation properties of the carbonized porous silicon revealed the following. In the red, carbonization of the sample at 1000 °C reduced the photoluminescence quenching and the quenching rates k_1 and k_2 by an average of 1.5–1.6 times, whereas for the sample treated at 1200 °C these parameters were reduced by factors of 2.7 and 5, respectively. The photoluminescence of sample No. 1 in the blue-green became even more stable, its amplitude decreasing only by 22%, whereas the photoluminescence of sample No. 2 varied negligibly under the laser action. These results indicate that an increasing number of stable surface states are formed as the carbonization temperature increases. It is interesting to note that the section of sample No. 2 beneath the mask shows increased photoluminescence in the short-wavelength region rather than quenching. Thus, by means of preliminary preparation we created conditions under which the photostimulated formation of luminescence centers described by the fourth term in Eq. (1) begins to play a dominant role.

To sum up, we have studied the spectral and degradation properties of porous silicon which has undergone fast high-temperature carbonization. The investigations showed that as a result of carbonization the photoluminescence spectrum of the porous silicon is modified appreciably: it exhibits two distinct peaks near 1.9 and 2.4 eV and the low-frequency band near 1.7 eV disappears. It was also observed that com-

pared with the initial samples, this treatment substantially reduces the rate of degradation of the porous silicon luminescence under the action of the cw laser radiation. In the blue–green, samples treated at 1200 °C possessed stable light-emitting properties. The results suggest that high-temperature carbonization is a promising method of modifying the spectral characteristics of the porous silicon photoluminescence and stabilizing its light-emitting properties.

This work was financed by the grants ''Conversion and High Technologies 1997–2000'' (101-1-2), ''Fundamental Research in High Technologies,'' and by the Russian Fund for Fundamental Research Grant No. 97-02-16710.

[1] L. T. Canham, Appl. Phys. Lett. **57**, 1046 (1990).
[2] V. Grivickas, J. Kolenda, A. Bernussi *et al.*, Braz. J. Phys. **24**, 349 (1994).
[3] C. Tsai, K.-H. Li, J. Sarathz *et al.*, Appl. Phys. Lett. **59**, 2814 (1991).
[4] I. M. Chang, G. S. Chou, D. C. Chang *et al.*, J. Appl. Phys. **77**, 5365 (1995).
[5] S. Migazaki, K. Shiba, K. Sakamoto *et al.*, Optoelectron., Devices Technol. **7**, 95 (1992).
[6] B. M. Kostishko, A. M. Orlov, and T. G. Emel'yanova, Neorg. Mater. **32**, 1432 (1996).
[7] H. Mimura, T. Futagi, T. Matsumoto *et al.*, Jpn. J. Appl. Phys., Part 1 **33**, 586 (1994).
[8] N. K. Kashkarov, E. A. Konstantinova, S. A. Petrov *et al.*, Fiz. Tekh. Poluprovodn. **31**, 745 (1997) [Semiconductors **31**, 639 (1997)].
[9] Sh. R. Atazhanov, A. N. Kamov, V. I. Chepurnov *et al.*, Abstracts of papers presented at the International Seminar on Semiconducting Silicon Carbide and Devices Using This [in Russian], Novgorod State University Press, Novgorod (1995), pp. 25–26.
[10] V. F. Agekyan, A. A. Lebedev, A. A. Lebedev *et al.*, Fiz. Tekh. Poluprovodn. **31**, 250 (1997) [Semiconductors **31**, 146 (1997)].
[11] G. D. Sanders and Yia-Chung Chang, Phys. Rev. B **45**, 9202 (1992).
[12] N. K. Kashparov, E. A. Konstantinova, and V. Yu. Timoshenko, Fiz. Tekh. Poluprovodn. **30**, 1479 (1996) [Semiconductors **30**, 778 (1996)].
[13] B. M. Kostishko, A. M. Orlov, and T. G. Emel'yanova, Pis'ma Zh. Tekh. Fiz. **22** (10), 68 (1996) [Tech. Phys. Lett. **22**, 417 (1996)].
[14] B. M. Kostishko and L. I. Gonchar, JETP Lett. **66**, 386 (1997).

Translated by R. M. Durham

Predetonation optical breakdown spectrum of silver azide

B. P. Aduev, É. D. Aluker, A. G. Krechetov, and Yu. P. Sakharchuk
(Submitted June 24, 1996; resubmitted January 8, 1998)
Pis'ma Zh. Tekh. Fiz. **24**, 31–34 (August 26, 1998)

Time-resolved predetonation absorption spectra of silver azide were measured using the ''spectrum per pulse'' technique. An analogy is observed between the behavior of the absorption spectra at the initial stages of explosive decomposition and radiolysis. From the character of the spectra it is inferred that during the explosive decomposition of AgN_3 the formation of N_2^- radicals precedes the formation of N_4^- radicals. © *1998 American Institute of Physics.* [S1063-7850(98)02208-3]

Although for many years silver azide has been a model substance for the study of initiating explosives,[1] the mechanism responsible for the explosive decomposition of AgN_3 has not yet been clarified.

The main reason for this, at first glance, paradoxical situation is that there are no reliable experimental data on the rate of variation of the main physical characteristics of the sample during the explosive decomposition process. It is our view that this gap may be filled by applying the experimental technique of flash radiolysis and photolysis[2] to study explosive processes.

In Ref. 3 we observed the predetonation conductivity and luminescence of silver azide and the predetonation luminescence spectrum was measured in Ref. 4. The present study, which is a continuation of Refs. 3 and 4, reports measurements of the predetonation optical absorption spectrum. The existence of predetonation absorption (without measuring its spectrum!) was confirmed in Ref. 5. However, in order to measure the spectral-kinetic characteristics of the absorption during an explosion, we need to measure the relaxation of the absorption spectrum during the explosion of a single sample because the spread of the sample characteristics and the stochastic nature of the explosive decomposition process mean that the method of measuring the spectrum ''one point at a time'' cannot be used.[4]

This problem was solved by using the apparatus shown schematically in Fig. 1. The explosion was initiated by a pulse from an electron accelerator *1* (10 ns, 300 keV, 10 A/cm^2). Probe light from an IFP-800 flashlamp *2* was passed through a lens *3* and the sample *4* located inside a vacuum chamber *5*, before being focused by a lens *6* onto the entry slit of an ISP-51 spectrograph *7*. An image of the spectrum was projected from the spectrograph along the time slit of an FÉR-7 streak camera *8* and was then passed to the photocathode of an image converter which swept the spectrum in time on the exit screen. The image was stored by a television readout device incorporating an LI-702 ''superkremnikon'' *2* and was fed to a computer *10* fitted with a special device for storing the transmitted information in digital form. The image converter traces were then processed as required. The components of the system were synchronized from the power supply to the television readout system *11* which triggered the line scan of the readout system, a digital information storage system and a GI-1 pulse generator *12*. The latter triggered the power supply *13* to the pulsed light source, the electron accelerator, and scanning of the streak camera with suitable time delays.

Using the spectrograph *7* and the streak camera *8* instead of the usual monochromator–photomultiplier system[3] in the recording channel allows us to record the relaxation of the absorption spectrum during the detonation of a single sample.

The maximum temporal resolution of the recording channel was 10 ns, the spectral resolution at the short-wavelength sensitivity limit was 0.02 eV, that at the long-wavelength limit was 0.05 eV, and the spatial resolution was better than 7.5 mm^{-1}.

The samples were AgN_3 single crystals ($3\times3\times0.05$ mm^3) grown from solution.

Figure 2 shows the absorption spectra at various times for one of the samples. We stress that the spectra shown in

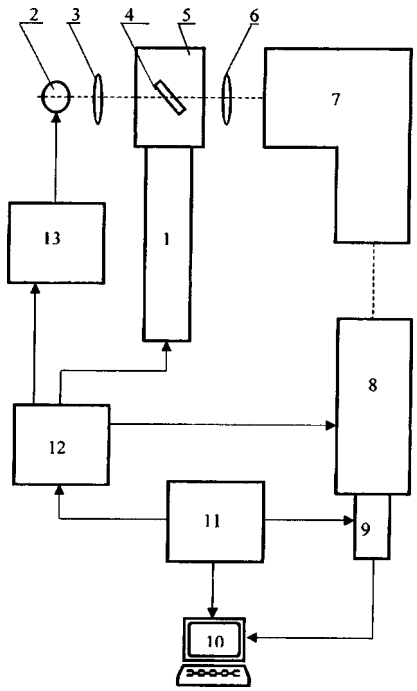

FIG. 1. Block diagram of apparatus to measure the relaxation kinetics of the predetonation absorption spectra (see text for notation).

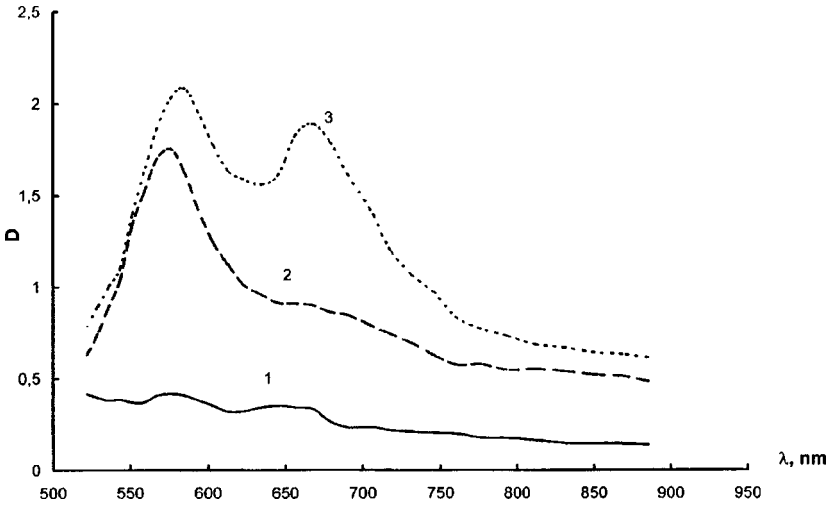

FIG. 2. Predetonation absorption spectra of AgN_3 at various times: *1* — 0.5 μs, *2* — 2 μs, *3* — 3.5 μs (the time is measured from the time of application of the ionizing pulse, *D* is the optical density).

Fig. 2 correspond to the absorption of the sample before the detonation, i.e., before the appearance of the line spectrum caused by the plasma luminescence formed as a result of detonation.[3,4] Thus, these spectra can be reliably identified as the preliminary absorption spectra.

We draw particular attention to the analogy between the behavior of the absorption spectra at the initial stages of explosive decomposition (Fig. 2) and the radiolysis of AgN_3 (Ref. 1).

The predominant view expressed in the literature (Ref. 1, for example) is that the observed spectra of irradiated AgN_3 are attributable to colloidal metal particles of various sizes which increase as the radiation dose increases.

In our experiments, however, broad, possibly not elementary, bands with peaks at 580 and 680 nm are observed during the evolution of the explosive process (Fig. 2). Interestingly, irradiated KN_3 crystals[1] reveal an absorption spectrum almost exactly the same as our measured predetonation spectrum in AgN_3 (Fig. 2). In the case of KN_3 the elementary components were isolated by pulsating annealing of the absorption spectra and ESR and it was established that the band with a peak at 565 nm belongs to N_2^- and the bands at 585 and 700 nm are assigned to N_4^- radicals.

In view of this reasoning, we consider that the interpretation of the predetonation absorption spectra as being similar to KH_3 is preferable. In this case, it follows from Fig. 2 that during the explosive decomposition of AgN_3 the formation of N_2^- radicals precedes the formation of N_4^- radicals.

[1] *Energetic Materials*, Vol. 1, *Physics and Chemistry of the Inorganic Azides*, edited by H. D. Fair and R. F. Walker (Plenum Press, New York, 1977), p. 501.
[2] É. D. Aluker, V. V. Gavrilov, R. G. Deĭch, and S. A. Chernov, *Fast Radiation-Stimulated Processes in Alkali-Halide Crystals* [in Russian], Zinatne, Riga (1987), p. 183.
[3] B. P. Aduev, É. D. Aluker, G. M. Belokurov *et al.*, [JETP Lett. **62**, 215 (1995).
[4] B. P. Aduev, É. D. Aluker, and A. G. Krechetov, Pis'ma Zh. Tekh. Fiz. **22**(6), 24 (1996) [Tech. Phys. Lett. **22**, 236 (1996)].
[5] S. M. Ryabykh and K. Sh. Karabukaev, *Radiation-Stimulated Effects in Solids* [in Russian], Sverdlovsk (1988), p. 51.

Translated by R. M. Durham

Removal of acrolein vapor from air by a nanosecond electron beam

Yu. N. Novoselov and I. E. Filatov

Institute of Electrophysics, Urals Branch of the Russian Academy of Sciences, Ekaterinburg
(Submitted February 16, 1998)
Pis'ma Zh. Tekh. Fiz. **24**, 35–39 (August 26, 1998)

Results are presented of an experimental investigation of the decomposition of small quantities of acrolein vapor in air irradiated by a pulsed electron beam. It is shown that the reduction in the impurity concentration as a function of the energy deposited in the gas is satisfactorily approximated by an exponential law. An empirical expression is derived to predict the energy consumption for a given initial acrolein concentration and required degree of purification.
 [S1063-7850(98)02308-8]

Many products of organic synthesis and also the manufacture of various articles using plastics are accompanied by the emission of air contaminated with vapor of volatile organic compounds. Technologies based on chemical methods have been developed to purify these emissions from toxic impurities. Recent research has shown that the use of cw electron beams to remove various toxic impurities from air mixtures is extremely efficient (see Refs. 1 and 2). It has also been shown that in some cases, pulsed beams can appreciably reduce the energy required for electrophysical purification compared with cw beams.[3,4] The aim of the present study was to investigate the removal of volatile organic compounds from air using a pulsed electron beam.

Acrolein ($CH_2=CH—CHO$), one of the most widespread and toxic volatile organic compounds, was selected for the investigations. The experiments were carried out using an apparatus based on the RADAN accelerator[5] described in Ref. 4. The accelerator generated an electron beam with an electron energy of 180 keV, beam current of 800 A at a 1 cm^2 exit window, a pulse length of 5 ns, and pulse repetition frequency up to 10 s^{-1}. An energy of 4.2×10^{-3} J was deposited in the gas volume during a single pulse and 90% of the energy was absorbed in a volume of 4 m^3 (the limit of the electron range in the gas was 1 cm). The model mixture was fed into a gas chamber having a total volume of 3 liter in which a built-in fan simulated a gas flow through the irradiated gap. The flow velocity was 0.5 m/s. The irradiated volume of the model mixture was uniformly mixed with the rest of the gas and after the cycle, was recirculated for purification. This system can simulate multistage purification.

For the experiments we used a model mixture of nitrogen and oxygen in the ratio $N_2:O_2=80:20$ at atmospheric pressure and room temperature, in which the concentration of acrolein vapor varied between 100 and 1000 ppm (the number of impurity molecules per 10^6 molecules of the main gas). The mixture was irradiated by a series of 1500 pulses. The impurity concentration was measured before irradiation and at the end of each series of pulses by taking samples of the mixture. The acrolein was then absorbed in an adsorption tube and extracted with hexane, and the finished preparation was analyzed by liquid chromatography using an ultraviolet detector at 208 nm. The acrolein concentration was determined with an error of less than 7% for impurity contents in the range 100–1000 ppm and 15% in the range 10–100 ppm.

It was found experimentally that the impurity concentration $[C]$ clearly decreases exponentially with the number of irradiation pulses N, i.e., the energy deposited in the volume (Fig. 1). These curves were used to determine the energy required to remove a single toxic molecule ε (eV/molecule). This value can be used to determine the energy efficiency of the process of purifying the air from acrolein vapor, and was calculated experimentally as in Ref. 4:

$$\varepsilon = Wn/e\Delta[C]. \tag{1}$$

Here W is the beam energy absorbed by the gas per pulse, $\Delta[C]$ is the change in the concentration of acrolein vapor after a series of irradiation pulses, n is the number of pulses in the irradiation series, and e is the electron charge. It was found that the parameter ε depends on the initial impurity concentration and varies between 3 and 10 eV/molecule when the initial concentration varies between 1100 and 100 ppm.

Figure 2 gives the logarithm of the ratio of the initial $[C_0]$ to the instantaneous $[C]$ acrolein concentration, $\ln([C_0]/[C])$, as a function of the total energy deposited in the gas W for various $[C_0]$. All these dependences have the form of straight lines with slope determined by the initial concentration. It can also be seen from the slope of the curves in Fig. 2 that as the concentration $[C_0]$ decreases, the degree of purification of the gas from impurities defined as $\eta=([C_0]-[C])/[C_0]$, increases for the same energy input.

The experiments showed that an exponential law accurately describes the change in the impurity concentration with increasing degree of purification up to 90%. Taking into account the linear nature of the curves in Fig. 2, we can assume that under our conditions, the process of acrolein removal obeys a first order macrokinetic equation in terms of impurity concentration:

$$d[C]/dN = -K[C], \tag{2}$$

where K is a certain constant having the appropriate dimensions. Since the energy W deposited in the gas is proportional to the number of radiation pulses N, the constant K

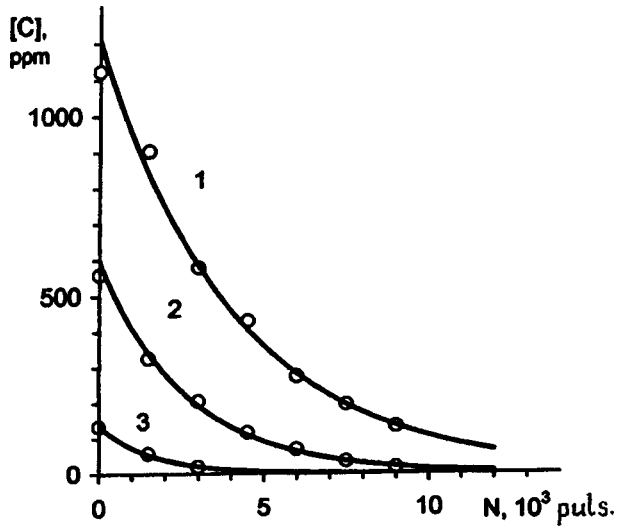

FIG. 1. Acrolein concentration $[C]$ as a function of the number of radiation pulses N for various initial concentrations: *1* — 1100 ppm, *2* — 550, and *3* — 220.

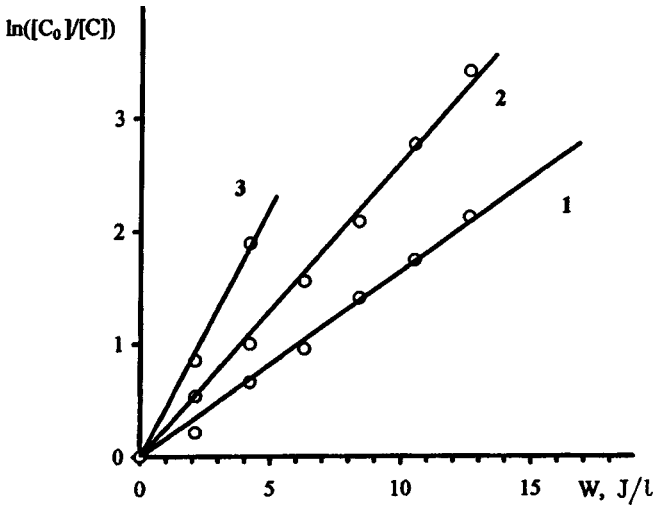

FIG. 2. Dependences of $\ln([C_0]/[C])$ on the specific energy W deposited in the gas for initial concentrations: *1* — 1100 ppm, *2* — 550, and *3* — 220.

can be calculated from the slope of the lines in Fig. 2: $\ln([C_0]/[C])=W/K$. The value of K characterizes the efficiency of acrolein removal from the air and has the physical meaning of the energy which must be deposited per unit volume of the air being treated to reduce the acrolein concentration by the factor $e=2.718\ldots$. For curves *1–3* in Fig. 2 the values of K are 6.1, 3.84, and 2.23 J/l, respectively.

In our case, the energy required to remove a single toxic molecule ε is satisfactorily approximated by an equation derived analytically from the condition that Eq. (2) is a first-order macroscopic process:

$$\varepsilon = AK\ln(1-\eta)^{-1}/[C_0]\eta, \tag{3}$$

where A is a constant supplying appropriate dimensions, equal to 235.5 (eV l ppm)/J. In accordance with Eq. (3) for initial concentrations $[C_0]=1000$, 500, and 100 ppm and a degree of purification of 80% ($\eta=0.8$), the values of ε are 2.9, 3.9, and 10.4 eV/molecule, respectively. The energy consumptions calculated using formula (3) only differ from those determined experimentally using formula (1) by 10–15%. Thus, these results can be used to predict the energy consumption for a given initial acrolein concentration and a required degree of a purification, which is important for the design and development of real purification systems.

The reduction of the acrolein concentration in ionized air is caused by the generation of various active particles by the electron beam, including atomic oxygen and ozone. The real mechanism for the decomposition of acrolein and the specific plasma-chemical reactions resulting in its decomposition require special investigation. Attention is drawn to the fact that the process of acrolein removal depends on its initial concentration. This is possibly because intermediate products of the impurity decomposition participate in the process.

[1] A. A. Valuev, A. S. Kaklyugin, G. É. Norman *et al.*, Teplofiz. Vys. Temp. **28**, 996 (1990).
[2] E. L. Neau, IEEE Trans. Plasma Sci. **22**, 2 (1994).
[3] D. L. Kusnetsov, G. A. Mesyats, and Yu. N. Novoselov, in *Proceedings of Conference on Novel Applications of Lasers and Pulsed Power*, San Jose, CA, 1995, pp. 142–146.
[4] D. L. Kuznetsov, G. A. Mesyats, and Yu. N. Novoselov, Teplofiz. Vys. Temp. **34**, 845 (1996).
[5] A. S. El'chaninov, A. S. Kotov, V. G. Shpak *et al.*, Élektron. Tekh. Ser. 4 **2**, 33 (1987).

Translated by R. M. Durham

Integrated sensor array for analysis of multicomponent gas mixtures

V. I. Anisimkin, É. Verona, V. E. Zemlyakov, R. G. Kryshtal', and A. V. Medved'

Institute of Radio Engineering and Electronics, Russian Academy of Sciences, Moscow;
O. M. Corbino Institute of Acoustics, National Research Council of Italy, Rome
(Submitted January 29, 1998)
Pis'ma Zh. Tekh. Fiz. **24**, 40–45 (August 26, 1998)

A new device has been proposed and tested experimentally for the discrimination of gases in ''electronic nose'' systems. The device consists of an array of surface-acoustic wave (SAW) sensors positioned on a single anisotropic substrate with a common gas-sensitive coating for each sensor. The specificity of the sensors is provided entirely by the elastic anisotropy of the single-crystal substrate: changes in the direction of propagation of the wave through the gas-sensitive film deposited on the anisotropic substrate are accompanied by changes in the partial components of the mechanical displacement of the wave and corresponding contributions to the resultant SAW ''response.'' © *1998 American Institute of Physics.*
[S1063-7850(98)02408-2]

Since the beginning of the eighties, the most promising approach to the quantitative and qualitative analysis of multicomponent gas mixtures has involved using ''electronic nose'' systems consisting of an array of several nonselective sensors whose combined responses to individual components of the mixture are subjected to special mathematical treatment.[1] This approach requires the reproducible fabrication of gas-sensitive coatings that age little, which must differ from each other to ensure the specificity of each sensor. Even if the physical properties of only one coating vary with time or from one batch to another, this impairs the initial calibration of the entire device, invalidates the mathematical treatment specific to this device, and results in an erroneous analysis of the mixture being tested.[2,3] In this context, there is an urgent need to search for alternative solutions to achieve better stability for this type of device.

Here we show that the capacity of surface-acoustic waves (SAWs) to change their gas ''response'' as a result of changes in the wave polarization[4] can be utilized to ensure the specificity of each sensor without using different gas-sensitive coatings, i.e., the problem of the long-term stability of the device, and thus its reliability, can be simplified.

The proposed device is shown schematically in Fig. 1. It consists of a piezoelectric acoustic line *1*, several pairs of interdigital transducers *2* distributed around a circle, to excite and detect SAWs, and a gas-sensitive coating *3* located at the center between the transducers. Each pair of transducers *2* together with the film *3* is an individual SAW sensor (channel) forming part of an integrated system (in Fig. 1 there are four such channels). When the film *3* adsorbs some particular gas, its physical properties undergo quite specific changes. The contributions of these changes to the resultant response of the SAW are determined by the structure of the mechanical displacements (polarization) of the wave which in turn depend on the direction of the SAW propagation.[4] Since the acoustic line is elastically anisotropic, the polarization of the SAW and thus the individual components of the SAW response to a particular gas differ in the different channels, although the gas-sensitive coating is common to all of them.

The integrated device was tested experimentally using an acoustic line made of *ST*-cut single-crystal quartz. The interdigital transducers *2* having a 3 mm aperture, were made of 200 nm thick aluminum. The distance between the centers of the transducers was 14.92 mm and their period (the length of the acoustic SAW wave) was $\lambda = 32\ \mu$m. The input transducers in all channels contained 50 pairs of fingers and the output transducers contained 70 pairs so that the nearest side lobes of the amplitude–frequency characteristic of all the channels could be suppressed by at least 30 dB, the relative pass band was ~1%, and the fluctuations in the pass band were less than 0.4 dB. The insertion losses in all the channels did not exceed 2 dB without matching the transducers with the external 50 Ω electrical circuits.

In order to ensure that the gas responses of the SAWs differed substantially in the different channels and at the same time, the efficiency of excitation (detection) of the SAWs remained high, the orientation of the channels was selected so that the structure of the mechanical displacements of the SAWs differed appreciably, while the coefficient of electromechanical coupling was high and the deviation of the energy flux was small for the different directions of wave propagation. As a result of numerical calculations,[5] the direction along the *X* crystallographic axis was selected for channel *d* and the directions at angles of $-40°$, $+30°$, and 90° to this axis were selected for channels *a*, *b*, and *c*. A three-component Rayleigh-type wave propagated in channels *a*, *b*, and *d* and a purely shear surface bulk acoustic wave propagated in channel *c*. The central frequencies of the channels were 102, 102, 98, and 156.5 MHz, respectively. A similar structure with two channels *c* and *d* was used earlier in Ref. 6.

The gas-sensitive film *3* positioned at the center of each channel (Fig. 1) was fabricated of pure palladium

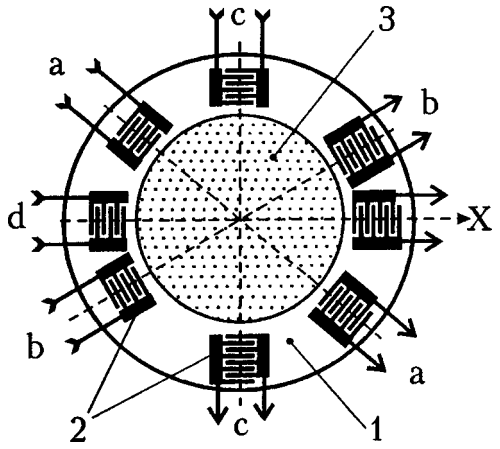

FIG. 1. Configuration of device: *1* – anisotropic piezoelectric substrate, *2* — interdigital transducers, and *3* — gas-sensitive film.

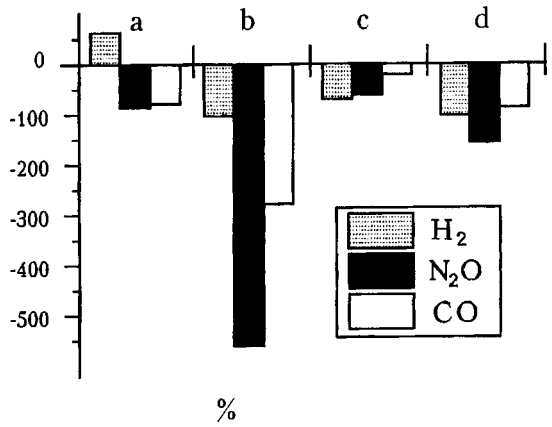

FIG. 2. Gas responses of integrated device: channel *d* — along the *X* axis, channels *a*, *b*, and *c* — at angles of $-40°$, $+30°$, and 90° to this axis. The SAW response to hydrogen in channel *d* is taken as 100% ($\Delta V/V = -13.3\times10^{-6}$).

(99.9999%) by thermal deposition in vacuum (10^{-6} Pa) at a substrate temperature of 40 °C. The film had a polycrystalline structure with a typical crystallite size of ~30 nm, thickness $h=100$ nm, and diameter 9 mm.

The measurements were made at room temperature and normal pressure using a phase method described in Ref. 4. The gas mixtures tested were $1\%H_2+N_2$, $1\%N_2O+N_2$, and $1\%CO+N_2$. Dry air was initially supplied to the measuring chamber (250 cm^3) at a constant velocity (50 m^3/min). The air was then shut off, the first gas mixture to be tested ($1\%H_2+N_2$) was fed in, and the SAW hydrogen response was measured for one channel. After shutting off the hydrogen, dry air was again supplied to the chamber and the gas–film system was restored to its initial state. Similarly, the SAW responses to the second ($1\%N_2O+N_2$) and third ($1\%CO+N_2$) gases were measured for the same channel. In order to monitor the state of the film, the SAW response to hydrogen was additionally measured before each new gas and compared with that for the fresh film: purification of the Pd film with dry air for 30 min completely restored it to the initial state.

As in Ref. 7, in the device being tested the interaction between the Pd film and the $1\%H_2+N_2$, $1\%N_2O+N_2$, and $1\%CO+N_2$ gases was mainly chemical and was caused by the presence of gaseous impurities (mainly oxygen) adsorbed from the atmosphere on the Pd crystallites before the beginning of the measurements. This interaction led to changes in the density ρ and elastic moduli C_{11} and C_{44} of the film, which in turn produced changes in the velocity V and phase φ of the wave propagation between the transducers ($\Delta V/V = -\Delta\varphi/\varphi$). The relative changes in the density $\Delta\rho/\rho$ and elastic moduli $\Delta C_{11}/C_{11}$ and $\Delta C_{44}/C_{44}$ of the film depended on the chemical activity of the tested gas relative to gaseous impurities in the film and differed for different gases. For a particular gas (fixed $\Delta\rho/\rho$, $\Delta C_{11}/C_{11}$, and $\Delta C_{44}/C_{44}$) the relative change in the SAW velocity $\Delta V/V$ (SAW response) is given by[4]

$$\frac{\Delta V}{V}=\left(\frac{\pi h}{2\lambda}\right)\times\left[-\frac{\Delta\rho}{\rho}A+\frac{\Delta C_{44}}{C_{44}}B+\left(\frac{\left(1+\dfrac{\Delta C_{44}}{C_{44}}\right)^2}{1-\dfrac{\Delta C_{11}}{C_{11}}}-1\right)D\right], \tag{1}$$

where h is the thickness of the film, λ is the acoustic wavelength, A, B, and D are coefficients which depend on the SAW polarization in a particular direction of propagation.

Switching the channels in Fig. 1, i.e., varying the direction of propagation of the SAW through the gas-sensitive film *3*, caused the coefficients A, B, and D and thus the values of the three terms in expression (1) to change. As a result, for the same film and a particular gas the SAW responses in the different channels differed appreciably.

The results of the measurements (Fig. 2) were normalized to the SAW response to hydrogen in channel *d*. It can be seen that for the same Pd film, the responses in the different channels differ in magnitude and sign. For instance, in channel *a* the response to hydrogen is positive, whereas in all the other channels it is negative. The maximum (minimum) sensitivity to hydrogen is observed in channel *d* (*c*) and that to N_2O and CO is observed in channel *b* (*c*).

Thus, changes in the polarization of an SAW as it propagates in different directions in the same crystallographic plane of an anisotropic single crystal mean that the same gas-sensitive coating can be used to produce integrated sensor arrays with different sensitivity to the same gases. Unlike known analogs (such as arrays of spatially separated field transistors with switches made of materials having different chemical compositions), the long-term stability and reproducibility of this integrated device depends only on the stability and reproducibility of one gas-sensitive film. In addition, since there is no need to use different films, the

gas-sensitive coating may be fabricated using a single, chemically pure material, which is more efficient.

Here the operation of this integrated array was demonstrated in the phased mode but it can also be operated in an active mode, as is usually the case in practice.

This work was carried out with the State support of Leading Science Schools in the Russian Federation, Grant No. 96-15-96397.

The authors are grateful to V. I. Fedosov for numerous calculations of SAW propagation characteristics in quartz.

[1] Yu. C. Vlasov, in *Proceedings of the Third NEXUSPAN Workshop on Microsystems in Environmental Monitoring*, Moscow, 1996, pp. 1–10.

[2] M. Holmberg, F. Winquist, I. Lundstrom, F. Davide, C. Natale, and A. D'Amico, Sens. Actuators B **35–36**, 528 (1996).

[3] D. Vlachos and J. Avarisiotis, Sens. Actuators B **33**, 77 (1996).

[4] V. I. Anisimkin, I. M. Kotelyanskii, V. I. Fedosov, C. Caliendo, P. Verardi, and E. Verona, in *Proceedings of the IEEE Ultrasonics Symposium*, Seattle, 1995, Vol. 1, pp. 515–518.

[5] V. I. Fedosov, V. I. Anisimkin, I. M. Kotelyanskii, C. Calendo, P. Verardi, and E. Verona, in *Proceedings of the IEEE Ultrasonics Symposium*, San Antonio, 1996, Vol. 1, pp. 207–212.

[6] V. I. Anisimkin, E. Verona, and A. D'Amico, Lett. Nuovo Cimento **11**, 503 (1989).

[7] V. I. Anisimkin, I. M. Kotelyanskiĭ, and E. Verona, Poverkhnost' No. 10, 20 (1996).

Translated by R. M. Durham

Resonant absorption of energy accompanying phase transitions in $NaKC_4H_4O_6 \cdot 4H_2O$

P. F. Zil'berman, I. N. Pavlenko, O. P. Zil'berman, and A. L. Belinskiĭ

Kabardino-Balkarskaya State Agricultural Academy, Nal'chik
(Submitted August 28, 1997; resubmitted January 11, 1998)
Pis'ma Zh. Tekh. Fiz. **24**, 46–49 (August 26, 1998)

Resonant absorption of external electric field energy was detected experimentally in the presence of phase transitions in Rochelle salt. An external alternating electric field leads to the appearance of an anomalous increase in the signal intensity at frequencies typical of those of the pulsed electric signal induced by a phase transition in the material. © *1998 American Institute of Physics.* [S1063-7850(98)02508-7]

The appearance of a pulsed electric potential in the presence of phase transitions or chemical conversions in ionic systems has recently been widely investigated. For instance, it was shown in Refs. 1 and 2 that this signal has a characteristic spectrum, specific to the material and process taking place in it. It was found that at the phase transition temperature $NaKC_4H_4O_6 \cdot 4H_2O$ reveals a pulsed electrical signal whose spectrum contains peaks at frequencies of 5.5, 11, 14, and 15 MHz (Ref. 3). It is known that at normal pressure this substance has two second-order phase transitions and two orthorhombic paraelectric phases below -255 K and above 297 K. The monoclinic ferroelectric phase is stable in the interval between these temperatures.[4]

However, it is known that external influences, particularly electric fields, have a directional effect on phase transitions and chemical conversions. For static electric fields the rate of contact melting, which is a first-order phase transition, reveals a nonlinear dependence on the external field strength.[5,6] For sinusoidal electric fields, frequency ranges are observed where the rate of this process increases abruptly[7] and finally, for pulsed fields the rate of this process reveals a minimum caused by changes in the ion diffusion mechanism.[8]

The appearance of these effects suggests that resonant absorption of the energy of an alternating electric field may be observed at the phase transition temperature in $NaKC_4H_4O_6 \cdot 4H_2O$.

To record the signal and its spectrum we used pulse and spectrum analyzers with a high input impedance rf pulse preamplifier. Cylindrical polycrystalline samples 8 mm in diameter and 5 mm high were prepared by pressing from ''KhCh'' grade material. The samples were placed in a thermostat with a controlled rate of heating. Each sample had four platinum electrodes, two being used to supply the external electric field and two to record the signal. The investigations were carried out using a pulsed electric field whose pulse length varied between 0.01 and 100 μs at a repetition frequency of 1–30 000 Hz and a sinusoidal frequency of 0.1–100 MHz. The generators could vary the electric field in the range 0–200 V/cm.

A study of the temperature dependence of the pulsed electric signal intensity for Rochelle salt, $NaKC_4H_4O_6 \cdot 4H_2O$, showed that this signal had a maximum of 1000 pulses/s at a temperature of 295 ± 3 K. An investigation of the spectral composition of this signal using the spectrum analyzer revealed peaks at frequencies of 5, 11.5, 13.2, and 16 MHz, in fairly good agreement with our previous results.

The application of an external pulsed electric field with pulse length between 0.01 and 100 μs and pulse repetition frequency 1–30 000 Hz at 200 V/cm, is accompanied by an appreciable increase in the signal intensity initiated at the phase transition temperature. The signal intensity in the absence of a phase transition (the background obtained for the temperature range 270–290 K) was 1–200 pulses/s. For this temperature range the sample exhibits regions of spontaneous polarization. An abrupt increase in the intensity of the recorded signal was observed at 295 ± 3 K and reached 4700 pulses/s for an external field with pulse repetition frequency 200 Hz and pulse length 250 μs.

An investigation of the influence of an external sinusoidal electric field on the intensity of the pulsed electric signal induced in the phase transition process showed that

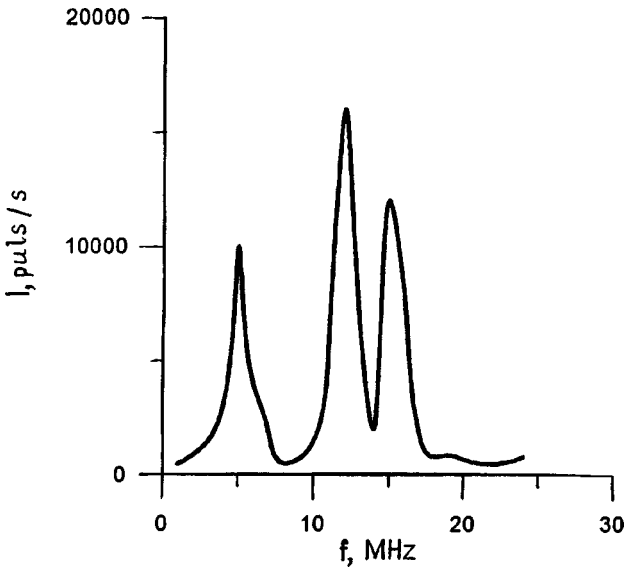

FIG. 1. Spectrum of the signal induced at the phase transition temperature in Rochelle salt (295 K) obtained when an external sinusoidal electric field was applied.

the increase in the intensity of the recorded signal is also only observed at 295 ± 3 K, which corresponds to the upper Curie point of Rochelle salt. A signal intensity of 9000–12 000 pulses/s was observed at frequencies of 4–6 and 15 MHz (see Fig. 1) and an increase in the intensity to 1600 pulses/s was observed in the range 10–13 MHz. The background intensity recorded at lower temperatures and the specified amplifier sensitivity did not exceed 500 pulses/s. This result indicates that resonant absorption of the external field energy may take place at these frequencies.

A comparison between our signal spectra obtained with and without an external field showed that both spectra contain peaks typical of each of these signals, but the peaks in the self-induced radiation spectrum have an integrated intensity far lower than that obtained with an applied external sinusoidal field. Assuming that the spectrum of the natural signal induced by the phase transition is determined by a quantity which characterizes the dynamics of ion transfer from one stable state to another, we can easily estimate the order of magnitude of the rate of ion displacement for the recorded frequency range. Calculations showed that this value is characteristic of diffusion processes taking place in a solid. Thus, the application of an external sinusoidal field selectively intensifies those ion displacements which characterize the phase transitions taking place in the material.

To sum up, resonant absorption of the energy of an external electric field has been detected experimentally in the presence of phase transitions in Rochelle salt. When an external alternating electric field was applied, an anomalous increase in the signal intensity was observed at frequencies characteristic of those of the pulsed electric signal induced by the phase transition in the material.

This work was performed with support from the Russian Fund for Fundamental Research.

[1] P. F. Zil'berman and P. A. Savintsev, Pis'ma Zh. Tekh. Fiz. **14**, 145 (1988) [Sov. Tech. Phys. Lett. **14**, 64 (1988)].
[2] P. F. Zilberman, *The Lars Onsager Symposium: Coupled Transport Processes and Phase Transitions*, Trondheim, Norway, 1993, p. 127.
[3] P. F. Zil'berman, P. A. Savintsev, and A. L. Belinskiĭ, Fiz. Tverd. Tela. (Leningrad) **30**, 1495 (1988) [Sov. Phys. Solid State **30**, 862 (1988)].
[4] E. Yu. Tonkov, *Phase Diagrams of Compounds at High Pressure* [in Russian], Nauka, Moscow (1983), 280 pp.
[5] P. F. Zil'berman, P. A. Savintsev, and Zh. A. Isakov, Fiz. Khim. Obrab. Mater. No. **5**, 86 (1981).
[6] P. A. Savintsev, P. F. Zil'berman, and S. P. Savintsev, *Physics of Contact Melting* [in Russian], Kabardino-Balkarskaya State University Press, Nal'chik (1987), p. 78.
[7] P. F. Zil'berman, P. A. Savintsev, and Zh. A. Isakov, Zh. Fiz. Khim. **55**, 783 (1981).
[8] P. F. Zil'berman and P. A. Savintsev, Zh. Fiz. Khim. **60**, 1248 (1986).

Translated by R. M. Durham

Dynamic characteristics of the plastic deformation kinetics of polycrystals

V. V. Ostashev and O. D. Shevchenko

Pskov Polytechnic Institute
(Submitted January 23, 1998)
Pis'ma Zh. Tekh. Fiz. **24**, 50–53 (August 26, 1998)

Methods of spectral analysis of local plastic deformations in polycrystalline copper on three structural levels are used to show that the tendency to synchronization is a general dynamic characteristic of the plastic deformation kinetics, and is a measure of the self-organization, evolution, stability, and decay of the dissipative structures in deformable polycrystals. The synchronization effect is directly related to the strength and plasticity characteristics.
 [S1063-7850(98)02608-1]

In general, a deformable polycrystalline material is considered to be a multilevel hierarchical dissipative system, which determines the wave nature of the evolution of deformations in polycrystals by means of the self-organization of relaxation fluxes of deformation defects and as a result of the appearance of translational–rotational vortices. Moreover, the evolution of dissipative structures contains general indicators, such as synchronization, stochasticity, and self-organization, which are observed as the form of organization of the mechanical properties and as the form of control of the mechanical properties.[1]

The method of investigation described in Ref. 2 is based on the grid subdivision and allows

– automated measurements of the displacement fields along the X and Y coordinates to within at least 2%;

– computer calculations of the components of the deformation and rotation tensor, the spectral characteristics of local plastic deformations, calculations of dissipative structures, phase and bifurcation diagrams, and statistical multilevel interactions.

The plastic deformation process is a physical model in which the size of the dividing mesh cell being analyzed is an image of the deformation defect at this structural level. An analysis is made of:

1. The macrolevel—the level of averaged description embracing the sample as a whole.

2. Cooperative processes at the level of an ensemble of grains—the dividing mesh has a cell size of 120 μm.

3. Intergranular plastic deformations—60 μm cell.

4. Effects determined by intragranular deformation—20 μm cell.

The characteristics of the evolution of plastic deformation when MO polycrystalline copper was subjected to static tension were investigated as a factor experiment. Depending on the values of the factors—strain rate $(1-5)\times 10^{-3}$ s^{-1}, elastic compliance constant of loading system 0.1–0.05 mm/kg, working length of sample 20–60 mm, and grain size 50–350 μm—we obtained various combinations of strength and plasticity characteristics which differed almost by a factor of two. The most important feature of the kinetics of plastic deformations at local structural levels is their oscillating nature, which depends on the deformation conditions. The internal structure of the buildup of linear, shear, and rotational deformation modes at three structural levels is described by a set of periodograms. Figure 1 gives an example of periodograms calculated using 400 points per window for periods 200–6000 μm of the linear strain $\varepsilon_{xx}=4.8\%$. Each periodogram characterizes the number of harmonic components of a specific wavelength, amplitude, and phase in the spectrum of the relevant deformation.

An analysis of the periodograms shows that as the degree of deformation increases, the number of harmonics in the spectrum increases, the entire spectrum shifts in the long-wavelength direction, and the frequencies become synchronized in time and space (levels 4–3–2). As in Ref. 3, we understand by synchronization the most general case when specific frequency relations are established as a result of the interaction of objects considered to be of equal importance The synchronization intensity is characterized by the coefficient of synchronization which is equal to the ratio of the number of tuned frequencies to the total number of spectrum harmonics being analyzed. In all cases, we determine the

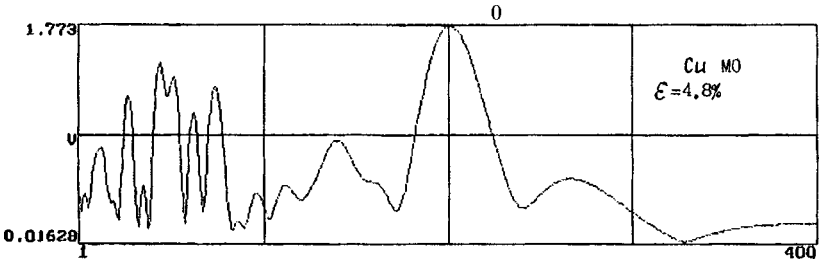

FIG. 1. Example of a spectral analysis of the local plastic deformations of Cu MO for $\varepsilon=4.8\%$.

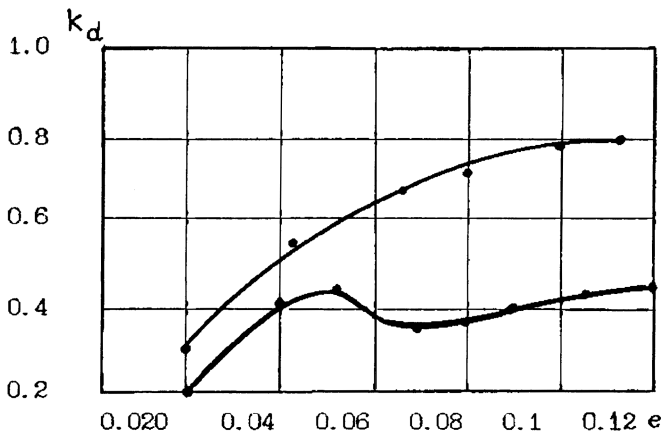

FIG. 2. Coefficient of synchronization versus degree of deformation: *1* — sample with maximum plasticity; *2* — sample with maximum strength.

frequency synchronization of the preceding deformations relative to the final deformation. Synchronization is generally initiated in the short-wavelength region and gradually shifts toward longer wavelengths. The maximum synchronization for all deformation modes, which increases monotonically with increasing degree of deformation, is observed for samples possessing maximum plasticity. The form of the dependence for samples with maximum strength is not well-defined (Fig. 2).

The relationship between the synchronization processes and the mechanical characteristics yields the following conclusions:

– assuming that each peak on the periodogram corresponds to a specific structural channel of stress relaxation, the synchronization of the spectrum harmonics may be determined as stability in the interacting subsystems at each structural level;

– under specific loading conditions synchronous clusters form in the material, these being a combination of synchronously operating deformation defects. As the number of harmonics involved in the operation of this cluster and the number of scale levels embraced by it increase, the relaxation processes at the mesolevel become more efficient and the overall plasticity of the material increases;

– synchronization is clearly one form of the self-organization, evolution, stability, and decay of dissipative structures in deformable polycrystals.

[1] V. E. Panin, Yu. V. Grinyaev, and V. I. Danilov, *Structural Levels of Plastic Deformation and Damage* [in Russian], Nauka, Novosibirsk (1990), 255 pp.
[2] V. V. Ostashev, A. D. Samarkin, and O. D. Shevchenko, in *BGPU Scientific Gazette* [in Russian], Belgorod (1996), pp. 72–76.
[3] I. I. Blekhman, *Synchronization in Science and Technology*, ASME Press, New York (1988); Nauka, Moscow (1981), 351 pp.

Translated by R. M. Durham

Mappings leading to randomization of an envelope of high-intensity spin waves

V. E. Demidov and N. G. Kovshikov

St. Petersburg State Electrotechnical University
(Submitted November 6, 1997)
Pis'ma Zh. Tekh. Fiz. **24**, 54–59 (August 26, 1998)

An experimental investigation was made of the transition to chaos in the self-modulation of high-intensity surface spin waves in magnetic films with nonlinearity caused by a three-magnon interaction. One-dimensional mappings leading to randomization of the envelope are constructed. It is shown that these mappings are universal and do not depend on the scenario for the transition to chaos. © *1998 American Institute of Physics.* [S1063-7850(98)02708-6]

The randomization of a spin-wave envelope under conditions of three-magnon decay has been investigated in detail for bulk magnetic samples (see Refs. 1 and 2). In this case, a wide range of scenarios was observed for the transition to chaos depending on the static magnetic field strength and the characteristics of the parametrically excited spin waves. In magnetic films this effect clearly has not been sufficiently well studied. We are only familiar with a few studies of deterministic chaos of spin waves in magnetic films under conditions of three-magnon interaction.[3,4] At the same time, films possess an important characteristic compared with bulk samples. As a result of the discrete property of the spectrum over a wide range of excitation intensity of the spin system, the number of interacting spin waves is bounded. This gives rise to stochastic dynamics characterized by few degrees of freedom which can be effectively investigated using point mapping theory.

In Ref. 4 we made a detailed study of the transition to chaos via period-doubling bifurcations in the self-modulation of spin waves in film samples. However, it has not yet been clarified how randomization takes place in the general case and which point mappings lead to such a wide range of scenarios. The aim of the present study was to identify the general laws governing the transition to chaos of an envelope for high-intensity spin waves under conditions of three-magnon decay in magnetic films.

The experiment was carried out using an apparatus in the form of a ''ring'' consisting of a spin-wave delay line with a microwave amplifier in a feedback circuit. This system can provide temporal amplification of the spin wave which is limited by nonlinear effects in the magnetic film. In order to vary the gain γ in the ring, a controlled attenuator was connected in series with the amplifier. A prototype of the delay line was placed in a static magnetic field tangential to the surface of the magnetic film, whose strength H_0 varied in the range 400–500 Oe. For the experiments we used yttrium iron garnet films 17 μm thick with saturation magnetization 1750 Cs and a linear dissipation parameter of 0.5 Oe. A surface spin wave was excited and detected using microstrip transducers 30 μm wide, positioned at a distance of 5 mm. The spin wave intensity was determined by detecting the signal at the exit transducer. After being amplified, the signal from the detector was fed to a computer fitted with a high-speed analog-to-digital converter.

As the gain in the ring increased, self-modulation of the spin wave was observed followed by randomization of its envelope. The scenario for the transition to chaos was very sensitive to the external magnetizing field H_0 and the wave number k of the spin wave. A series of measurements was made of the time series of the spin wave intensity. Oscilloscope traces of the envelope recorded at $H_0 = 496$ and 472 Oe, respectively are shown in the right-hand columns of Figs. 1 and 2. The carrier frequencies of the spin waves were 3200 and 3100 MHz and their wave numbers were 85 and 77 cm^{-1}, respectively. Traces a–e were recorded with the gain γ in the ring gradually increased. In the first case, the transition to chaos took place via a series of period-doubling bifurcations. Two- and four-period oscillations were observed after which the envelope become clearly stochastic. In the second case, the transition to chaos was not described by any known model scenarios.

These time series were used to construct dependences of the absolute value of the next peak on the trace as a function of the previous one. This construct determines the sequence function of the points where the attractor trajectories penetrate the secant of the Poincaré surface parameterized by the condition that this coordinate is maximized in phase space—a point mapping.[5] These mappings are plotted in the left-hand columns in Figs. 1 and 2. It can be seen that in both cases, the mappings are qualitatively the same, comprising curves with two, near-parabolic extrema but having substantially different curvature (Figs. 1e and 2e). However, quantitative differences between the mappings lead to significantly different dynamics of the spin wave envelope.

For convenience of analysis we divide the mapping into three regions: I — the branch before the first extremum, II — the branch between the extrema, and III — the branch after the second extremum.

In the first case, the mapping point moves on branches I and II of the parabola of the first extremum in regions of the curve where its derivative is greater than unity (stretching mapping). In accordance with the Feigenbaum theory,[6] these conditions are sufficient for the oscillations of the envelope

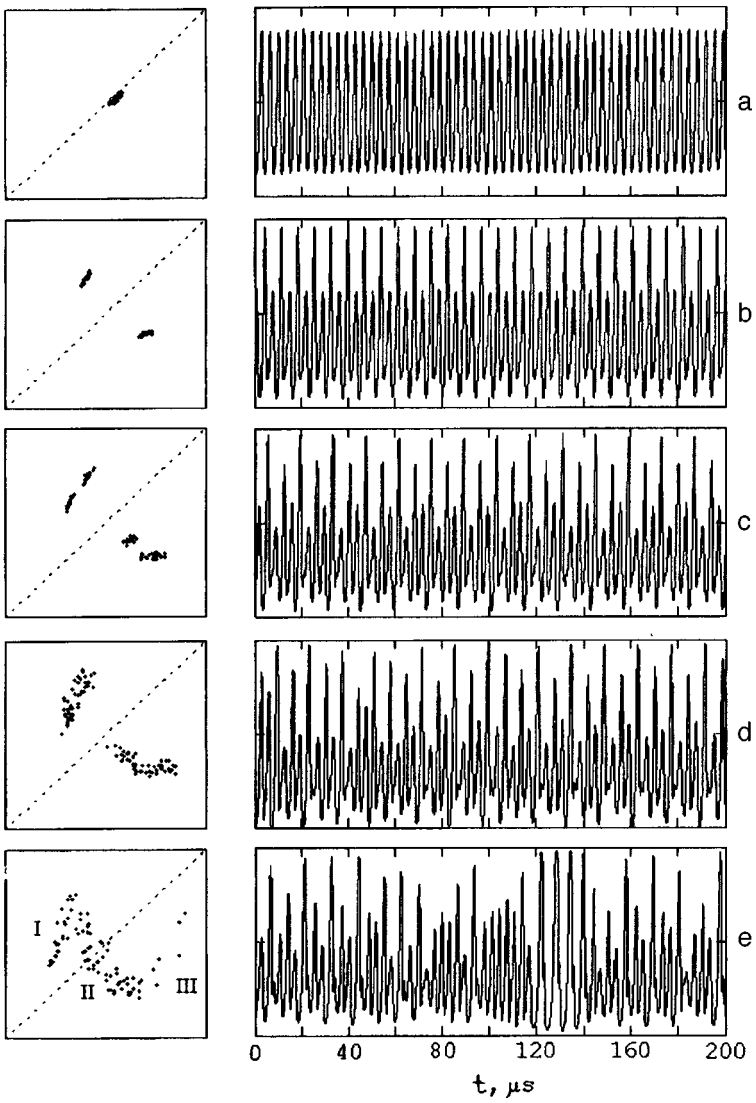

FIG. 1. Point mappings and oscilloscope traces of an envelope for $H_0=496$ Oe and $\gamma=0.4-0.7\ \mu s^{-1}$.

to undergo a cascade of period-doubling bifurcations. It can be seen from the first three mappings in Fig. 1 that this is what happens. However, as the gain in the ring increases, the mapping changes. In this case, the regions visited by the mapping point move toward the second extremum where the derivative of the curve becomes less than unity (compressive mapping). As a result, the doublings cease and the motion extends to the entire mapping. Thus, a pure scenario for the transition to chaos via period doubling is not achieved in the system because the mapping deviates from parabolic. However, the presence of parabolic sections leads to the possible existence of a doubling series.

In the second case, the motion of the mapping point is initially localized on branch II. This is evidently because the working part of the mapping is shifted toward the second extremum, i.e., the working parts are branches II and III. However, these branches have significantly different derivatives: branch II is stretching and branch III is compressive. Consequently, as the gain increases, the motion of the mapping point extends from branch II to branch III as its derivative increases. In this case, the oscillations of the envelope are initially randomized and they evolve in the direction of increasing the depth of the jumps of the spin-wave intensity peaks. Thus, this mapping allows both soft and hard transitions to stochasticity.

It should be noted that the observed scenarios for the transition of the spin wave envelope to chaos in ferromagnetic films are not completely covered by the two variants shown. They are described here to show that even such—at first glance—different randomization paths are generated by qualitatively similar mappings.

The transition of the spin wave envelop to chaos was investigated for magnetizing fields of 400–500 Oe and wave numbers between 30 and 150 cm^{-1}. All the mapping points obtained were similar to those described above. It can thus be stated that the transition of a spin wave envelope has common features for different values of H_0 and k despite the abundance of scenarios observed for this transition.

These results confirm that the stochastic dynamics of high-intensity spin waves established under conditions of

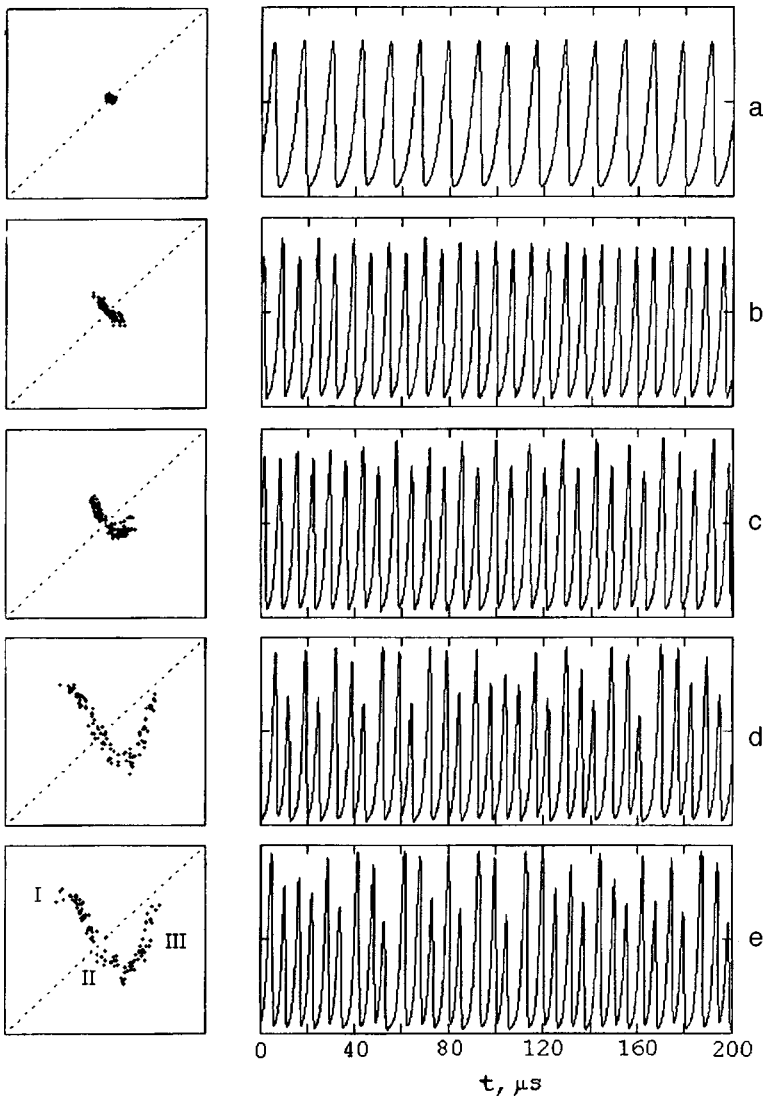

FIG. 2. Point mappings and oscilloscope traces of an envelope for $H_0=472$ Oe and $\gamma=0.1-0.3\ \mu s^{-1}$.

three-magnon interaction in magnetic films, are described by comparatively simple one-dimensional point mappings. These are universal over a wide range of external magnetic fields and spin wave numbers.

The authors are deeply grateful to B. A. Kalinikos for discussions of the results.

This work was financed by the Russian Fund for Fundamental Research (Grant No. 96-02-19515) and by the Ministry for General and Professional Education of the Russian Federation (Grant No. 97-8.3-13).

[1] H. Benner, R. Henn, F. Roedelsperger *et al.*, Izv. Vyssh. Uchebn. Zaved. IND **3**(1), 32 (1995).
[2] A. I. Smirnov, Zh. Éksp. Teor. Fiz. **90**, 385 (1986) [Sov. Phys. JETP **63**, 222 (1986)].
[3] A. M. Mednikov, Fiz. Tverd. Tela (Leningrad) **23**, 242 (1981) [Sov. Phys. JETP **23**, 136 (1981)].
[4] V. E. Demidov and N. G. Kovshikov, JETP Lett. **66**, 261 (1997).
[5] M. I. Rabinovich and D. I. Trubetskov, *Introduction to the Theory of Oscillations and Waves* [in Russian], Nauka, Moscow (1992), 454 pp.
[6] M. J. Feigenbaum, J. Stat. Phys. **19**, 25 (1978).

Translated by R. M. Durham

Phase optical bistability in structures with surface plasmons

V. F. Nazvanov and D. I. Kovalenko

Saratov State University
(Submitted January 28, 1997; resubmitted February 25, 1998)
Pis'ma Zh. Tekh. Fiz. **24**, 60–65 (August 26, 1998)

A theoretical analysis is made of the phenomenon of phase optical bistability in structures with surface plasmons. It is shown that in an optical waveguide with a nonlinear layer, not only amplitude but also phase bistability may occur when p-polarized radiation is reflected from the nonlinear waveguide. © *1998 American Institute of Physics.* [S1063-7850(98)02808-0]

Methods of creating spatial phase bistability and multistability are of fundamental importance for the physics and engineering of the next generation of optical computers. The development of these systems will allow us to construct systems for parallel processing of phase information.[1] Optical media with cubic nonlinearity offer particularly extensive possibilities here since they can produce ''hysteresis'' phase bistability of the same type as the well-known amplitude bistability.[2]

Of particular interest is the type of phase bistability caused by the reflection of radiation from the interface of a linear medium with cubic optical nonlinearity. Since in this case, the permittivity depends on the intensity of the incident wave, the changes in the reflected wave are determined by the initial intensity. As a result, under certain conditions jumps in intensity and in phase may occur in the reflected wave.

The history of this topic is described in Refs. 3 and 4. Bistability and hysteresis accompanying the reflection of electromagnetic radiation from the interface of a nonlinear medium were predicted by Silin.[5] With reference to optics, the problem of bistability accompanying the reflection of a plane wave from the interface of a medium with Kerr nonlinearity was then posed in Refs. 6 and 7 and a systematic solution was given in Refs. 8 and 9. A similar problem for an optical waveguide with a nonlinear layer was also examined in the plane wave approximation for amplitude bistability in Refs. 10 and 11 and for phase bistability in Ref. 12 (for s-polarized radiation). Finally, in Ref. 13 a theoretical analysis was made of the possibility of optical bistability in the coefficient of reflection of p-polarized radiation from an interface with a nonlinear Kerr medium (CS_2) with the excitation of surface plasmons.

Optical bistability accompanying the reflection of radiation from a glass–Kerr medium (CS_2) interface was observed experimentally by the authors of Ref. 14 and they obtained a value of order 8×10^9 W/cm^2 for the critical power. In Ref. 15 optical bistability was demonstrated using the effect of frustrated total internal reflection in a nonlinear light filter with a liquid crystal used as the nonlinear material. Optical bistability with the excitation of surface plasmons was observed in structures containing either CS_2 (Ref. 16) or a liquid crystal[17–20] as the nonlinear medium.

The aim of the present study is to make a theoretical analysis of the possibility of achieving phase optical bistability in the reflection of p-polarized radiation from the waveguide considered in Ref. 13.

As in Ref. 13, we used the plane wave approximation. A matrix method[21] was used for the calculations. In order to use the matrix method, we need to know the properties of all the layers contained in the structure. The properties of the nonlinear medium depend on the intensity of the radiation transmitted by the structure $\varepsilon_t=\varepsilon_{t0}+\alpha|E_t|^2$, where ε_{t0} is the permittivity of the nonlinear medium at zero radiation intensity and α is the coefficient of nonlinearity of the medium, which is related to the Kerr coefficient n_2 by[22] $n_2=(1/(2\sqrt{\varepsilon_{t0}}))\alpha$, where E_t is the amplitude of the radiation transmitted by the medium. Thus, a system of nonlinear equations must be solved for the problem as formulated. The solution can be simplified if we assume that the coefficients of reflection and transmission, and the amplitude of the incident radiation are functions of the transmitted radiation intensity. In Ref. 13 the authors succeeded in obtaining this function in analytic form when analyzing a structure with the Kretschmann configuration (glass–metal–nonlinear insulator). This approach to solving the problem cannot be used to obtain the phase characteristics of the reflected/transmitted radiation.

We used the Newton–Raphson method[23] to solve this problem. This method gives an accuracy of order 10^{-12} after three or four iterations.

For the calculations we used the following structural parameters (in a Kretschmann geometry): glass ($\varepsilon=3.6$), metal ($\varepsilon=-57.8+i0.6$, $d=625$ Å), and nonlinear medium ($\varepsilon_{t0}=2.25$, $n_2=3\times10^{-8}$ cm^2/W) at $\lambda=10\,600$ Å. The results are plotted in Figs. 1 and 2.

Figure 1 gives the coefficient of energy reflection as a function of the dimensionless radiation intensity incident on the structure at various angles. As was to be expected, curve *3* in Fig. 1 is the same as the curve from Ref. 13. It can be seen that bistability begins to appear at angles of incidence greater than 53°52′ (the resonant angle is 53°45′41.53″). As the angle of incidence increases, both the amplitude of the hysteresis and the incident radiation power required for its occurrence increase. For instance, for curve *3* the critical radiation power for switching corresponds to 3×10^8 W/cm^2, as in Ref. 13.

Figure 2 gives an important result of our study: the de-

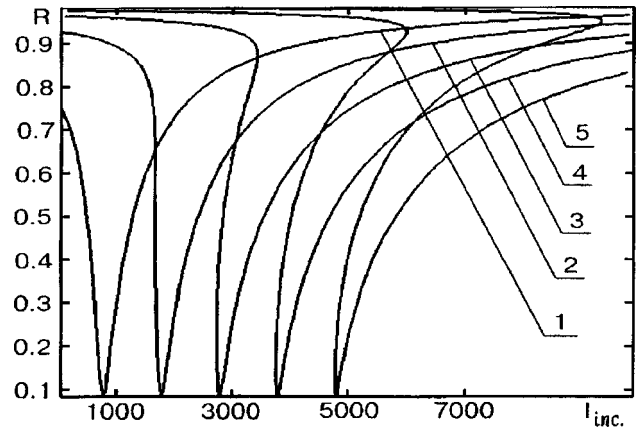

FIG. 1. Coefficient of energy reflection versus dimensionless intensity of the radiation incident on structure. The curves are plotted for various angles of incidence: *1* —53°48′, *2* — 53°51′, *3* — 53°54′, *4* — 53°57′, *5* — 54°. The reflection minimum is achieved at 53°45′41.53″.

pendence of the phase shift between the *p*- and *s*-polarized components of the reflected radiation on the dimensionless radiation intensity incident on the structure at various angles. As we reported earlier,[24] the phase is far more sensitive to changes in the properties of the structure than is the amplitude. It can be seen that phase bistability appears from angles of incidence greater than 53°50′.

Thus, we have made a theoretical analysis of phase optical bistability in structures with surface plasmons. We have shown that both amplitude and phase bistability may occur in an optical waveguide with a nonlinear layer when *p*-polarized radiation is reflected from the nonlinear waveguide.

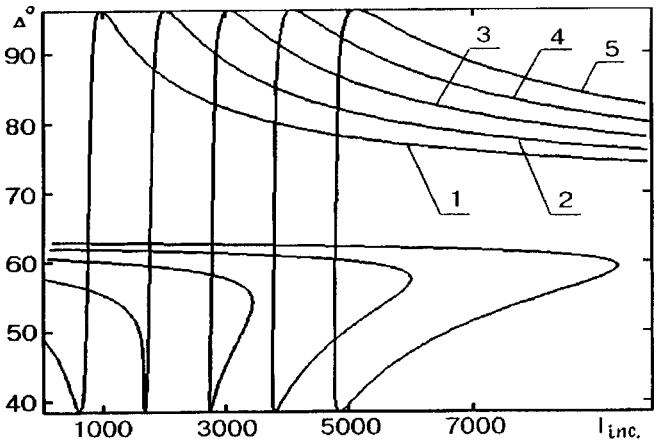

FIG. 2. Phase shift between the *p*- and *s*-polarized components of the reflected radiation versus dimensionless intensity of the radiation incident on the structure: The curves are plotted for various angles of incidence: *1* — 53°48′, *2* — 53°51′, *3* — 53°54′, *4* — 53°57′, *5* — 54°. The reflection minimum is achieved at 53°45′41.53″.

We used the plane wave approximation whose validity for optical beams of finite width may pose problems (see Ref. 3) for local Kerr nonlinearity when the beam splits into separate filaments. Nevertheless, many of the experiments using prism coupling mentioned earlier revealed bistability in reflection where the experimental results showed good agreement with the plane wave model,[12,15] which may be attributed to the nonlocal nature of the nonlinear processes.[25,26] This effect may be observed particularly clearly for nonlinear materials such as liquid crystals or semiconductors since the observed effects include diffusion processes such as heat or carrier transport. These processes may be important in studies of optical bistability under conditions where surface plasmons are excited (see Refs. 17–20).

The authors are extremely grateful to the referee for many useful comments on this work.

[1] S. A. Akhmanov, N. N. Akhmedov, A. V. Belinskiĭ *et al.*, in *New Physical Principles of Optical Information Processing*, edited by S. A. Akhmanov and M. A. Vorontsov [in Russian], Nauka (Problems in Science and Technical Progress), Moscow (1990), p. 83.
[2] H. M. Gibbs, *Optical Bistability: Controlling Light with Light* (Academic Press, Orlando, 1985; Mir, Moscow, 1988).
[3] N. N. Rozanov, *Optical Bistability and Hysteresis in Distributed Nonlinear Systems* [in Russian], Nauka, Moscow (1997).
[4] B. B. Boĭko and N. S. Petrov, *Reflection of Light from Amplifying and Nonlinear Media* [in Russian], Nauka i Tekhnika, Minsk (1988).
[5] V. P. Silin, Zh. Éksp. Teor. Fiz. **53**, 1662 (1968) [Sov. Phys. JETP **26**, 955 (1968)].
[6] B. B. Boĭko, I. Z. Dzhilavdari, and N. S. Petrov, Zh. Prikl. Spektrosk. **23**, 888 (1975).
[7] A. E. Kaplan, JETP Lett. **24**, 114 (1976)]; Zh. Éksp. Teor. Fiz. **72**, 1710 (1977) [Sov. Phys. JETP **45**, 896 (1977)].
[8] A. A. Kolokalov and A. I. Sukov, Izv. Vyssh. Uchebn. Zaved. Radiofiz. **21**, 1309 (1978).
[9] N. N. Rozanov, Pis'ma Zh. Tekh. Fiz. **4**, 74 (1978) [Sov. Tech. Phys. Lett. **4**, 30 (1978)].
[10] B. Bosacchi and L. M. Narducci, Opt. Lett. **8**, 324 (1983).
[11] V. J. Montemayer and R. T. Deck, J. Opt. Soc. Am. B **2**, 1010 (1985).
[12] M. Haelterman, Opt. Lett. **13**, 791 (1988).
[13] G. M. Wysin, H. J. Simon, and R. T. Deck, Opt. Lett. **6**, 30 (1981).
[14] P. W. Smith, J. P. Herman, W. J. Tomlinson, and P. J. Maloney, Appl. Phys. Lett. **35**, 846 (1979).
[15] M. Haelterman and C. Waelbroeck, Appl. Phys. Lett. **56**, 512 (1990).
[16] P. Martinot, A. Koster, and S. Laval, IEEE J. Quantum Electron. **QE-21**, 1140 (1985).
[17] S. M. Arakelyan, L. S. Aslanyan, G. L. Grigoryan *et al.*, Izv. Akad. Nauk SSSR, Ser. Fiz. **49**, 795 (1985).
[18] R. A. Innes and J. R. Sambles, Opt. Commun. **64**, 288 (1987).
[19] R. A. Innes, S. P. Ashworth, and J. R. Sambles, Phys. Lett. A **135**, 357 (1989).
[20] R. A. Innes and J. R. Sambles, J. Phys.: Condens. Matter **1**, 6231 (1989).
[21] G. J. Sprokel, Mol. Cryst. Liq. Cryst. **68**, 39 (1981).
[22] N. K. Sidorov, *Introduction to Wave Nonlinear Optics* [in Russian], Saratov University Press, Saratov (1991), p. 12.
[23] V. P. D'yakonov, *Handbook of Algorithms and Programs in BASIC for Personal Computers* [in Russian], Nauka, Moscow (1989), 240 pp.
[24] V. F. Nazvanov and D. I. Kovalenko, Pis'ma Zh. Tekh. Fiz. **21**(14), 60 (1995) [Tech. Phys. Lett. **21**, 565 (1995)].
[25] G. Vitrant and P. Arlot, J. Appl. Phys. **61**, 4744 (1987).
[26] G. Vitrant *et al.*, Opt. Lett. **14**, 898 (1989).

Translated by R. M. Durham

Application of the particle-in-cell method to calculate the parameters of molecular beams from gasdynamic sources

G. B. Krygin, V. F. Ezhov, V. L. Ryabov, and V. V. Yashchuk

St. Petersburg B. P. Konstantinov Institute of Nuclear Physics, Gatchina
(Submitted October 9, 1997; resubmitted March 16, 1998)
Pis'ma Zh. Tekh. Fiz. **24**, 66–72 (August 26, 1998)

The particle-in-cell method is used to calculate the flow fields of gases formed by supersonic nozzles of different shapes under flow conditions typical of gasdynamic sources of molecular beams. The proposed calculation scheme is tested by comparing the calculated flow fields from an acoustic nozzle with the semiempirical calculations made by Ashkenas and Sherman. For a nozzle with a conical supersonic section the calculations are compared with the results of time-of-flight measurements made using the molecular beam generator at the St. Petersburg Institute of Nuclear Physics of the Russian Academy of Sciences. Prospects for the further use of these calculation methods to develop and optimize gasdynamic sources of molecular beams are discussed. [S1063-7850(98)02908-5]

The development and fabrication of new types of gasdynamic sources requires the corresponding development of theoretical methods designed to optimize the beam formation conditions and parameters. However, the complexity of the processes accompanying the supersonic expansion of a gas, which undergoes a gradual transition from continuous to free-molecular flow, and the complete dependence of the flow parameters on the nozzle design, skimmer geometry, and the vacuum conditions explain the absence of a general theoretical approach to describe gasdynamic sources.

Practical calculations of molecular beam sources are generally made in two stages. At the first stage, the gasdynamics of continuous media are used to solve the problem of the formation of a supersonic flow by a nozzle for given initial and boundary conditions. The transition to the next stage, at which free molecular flow takes place, is made using concepts of constant (frozen) flow parameters beginning from a certain time in the supersonic expansion. This simplified calculation scheme for gasdynamic sources, which neglects the transition region of the low-density gas dynamics, is justified by the fact that it is adequate for practical purposes, since the beam parameters depend so strongly on uncontrollable conditions of formation determined, for example by skimmer interactions, that absolutely accurate calculations become meaningless.

A characteristic feature of an underexpanded supersonic jet formed in a gasdynamic source is the very high nonuniformity of the stream. In this and similar cases, it is natural to use so-called uniform shock-capturing methods at the first stage, one of which is the well-known particle-in-cell method[1] which can be used to analyze a wide range of many-dimensional steady-state and nonsteady-state problems in gasdynamics using a standard numerical approach and can yield three-dimensional flow fields over a wide range of velocities between subsonic and hypersonic.

Here we do not attempt to give an exhaustive description of the processes accompanying the formation of molecular beams in gasdynamic sources. The basic idea was to obtain a fairly simple, reliable numerical method of determining the flow parameters which have a major influence on the operation of this type of source.

Back in the seventies, the wealth of calculated and experimental data accumulated was used by Ashkenas and Sherman to produce a semiempirical description of the flow field from an acoustic nozzle.[2] Their proposed analytic expressions can be used to find the spatial distributions of the flow parameters and to determine the position of its structural characteristics.

In accordance with Ref. 2, the expression for the Mach number M in the downstream direction has a simple form, reflecting almost pure radial expansion:

$$M = A\left(\frac{Z-Z_0}{D}\right)^{\gamma-1} - \frac{1}{2}\left(\frac{\gamma+1}{\gamma-1}\right)\left(A\left(\frac{Z-Z_0}{D}\right)^{\gamma-1}\right)^{-1}, \quad (1)$$

where γ is the ratio of C_p to C_v for the expanding gas, and the values of A and Z_0 are constants which depend on γ and are calculated or determined experimentally.

Under the gasdynamic conditions of continuous media, for a given value of γ the shape and size of the dependent shock wave and the Mach disk are exclusively determined by the given ratio of the pressures in the nozzle receiver P_0 and the expansion chamber P_1. The axial distance between the nozzle and the Mach disk Z_M for ratios P_0/P_1 between 15 and 17 000 also does not depend on γ (Ref. 2):

$$\frac{Z_M}{D} = 0.67\left(\frac{P_0}{P_1}\right)^{1/2}. \quad (2)$$

This type of analytic expression obtained by Ashkenas and Sherman is very convenient for testing gasdynamic calculation methods and programs.

The results of our calculations using the particle-in-cell method essentially coincide with the Mach number distributions along the axis calculated using Eq. (1) and reasonably well reproduce the dependences (2), as can be seen from

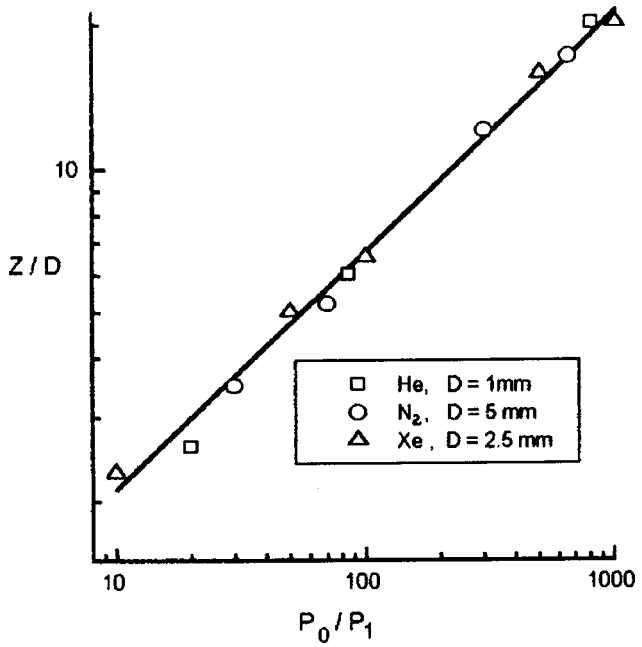

FIG. 1. Position of the Mach disk in a stream formed by an acoustic nozzle as a function of the pressure ratio P_0/P_1. The solid curve gives the results of the calculations using formula (2).

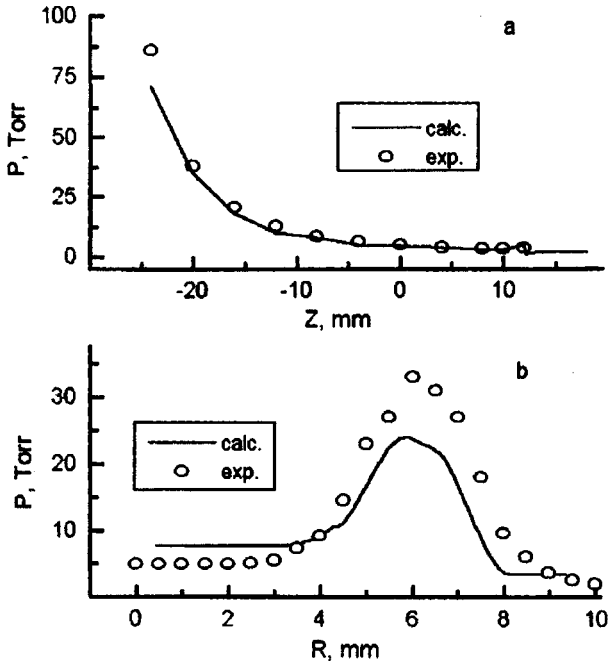

FIG. 2. Distributions of total pressure in supersonic nitrogen stream formed by a conical nozzle ($D=1.1$ mm, $\alpha_1=80°$, $\alpha_2=41°$, $P_0=760$ Torr, $T_0=300$ K, $Q=100$ l/s): a — axial distribution, b — transverse distribution at nozzle edge for $Z=0$.

Fig. 1. The calculations were made in a cylindrical coordinate system using a spatially fixed calculation mesh consisting of rectangular cells (800 along the r axis and 400 along the z axis). Note that these results depend weakly (of the order of a few percent) on the size of the calculation mesh.

Relations (1) and (2), and similar ones show good agreement with the experiment provided that the flow remains isentropic and continuous in the region being described. In the transition to nonisentropic free-molecular flow, a reduction in the collision frequency of the gas molecules leads to freezing of the static translational temperature in the stream and with this, the Mach numbers. Regardless of the geometry of the specific problem, the transition to free molecular flow (second calculation stage) may be described in terms of the competition between the rate of change in the static temperature in the stream and the collision frequency:[3]

$$\frac{1}{T}\left|\frac{dT}{dt}\right| = U\frac{1}{T}\left|\frac{dT}{dZ}\right| = \left(\frac{8kT}{\pi m}\right)^{1/2}\sqrt{2}n\sigma, \qquad (3)$$

where U is the average mass velocity of the flow particles, k is the Boltzmann constant, m is the molar mass of the gas, n is the particle number density, and σ is the collision cross section calculated in terms of viscosity. Freezing occurs when the collision frequency falls below the rate of change in the static temperature. In this case, the Mach number on the axis of the stream will be M_F.

Our calculations and experiments have shown that this approach can be used to find the limiting parameters of flows formed by nozzles of varying configuration with sufficient accuracy for practical purposes.

The experiments described were carried out using the molecular beam generator at the St. Petersburg Institute of Nuclear Physics.[4] Figure 2 shows the distributions of the total pressure in a supersonic nitrogen stream formed by a conical nozzle whose geometry is defined by the throat diameter $D=1.1$ mm and cone expansion angles in the subsonic and supersonic sections $\alpha_1=80°$ and $\alpha_2=41°$. The initial conditions in the nozzle receiver ($P_0=760$ Torr, $T_0=300$ K) together with the low pumping speed in the source chamber ($Q=100$ l/s) provided a flow regime typical of a dense gas over almost the entire region of the measurements. It can be seen that these calculations reproduce the

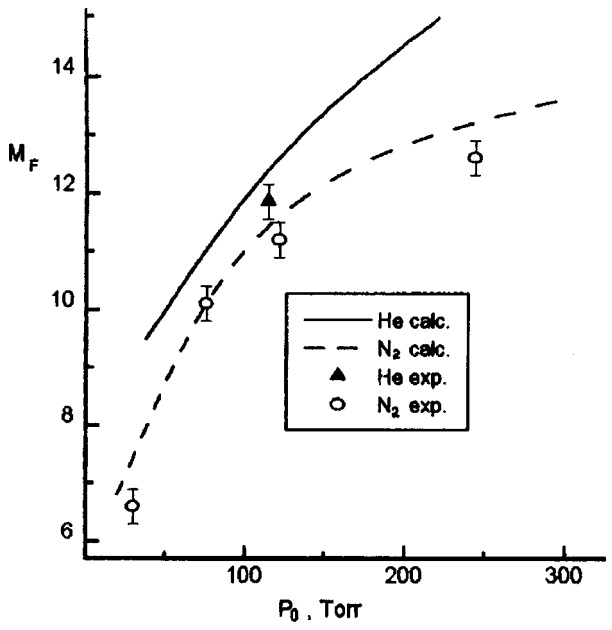

FIG. 3. Maximum attainable Mach number M_F versus P_0 ($D=1.1$ mm, $\alpha_1=80°$, $\alpha_2=40°$, $T_0=300$ K, $Q=4\times10^4$ l/s) for nitrogen and helium.

longitudinal distribution of the total pressure and the structure of the jet in the transverse cross section.

Figure 3 gives calculated dependences of the maximum attainable Mach number M_F as a function of P_0 for the stream of nitrogen and helium flowing from a nozzle ($D=1$ mm, $\alpha_1=80°$, $\alpha_2=40°$) into the vacuum chamber of the molecular beam generator ($Q=4\times10^4$ l/s). It can be seen that agreement between the calculations and the experiment is satisfactory for our purposes.

The approach developed here has been successfully used to describe a multinozzle molecular beam source.[5] The calculations of the gas jet–carrier parameters (Mach number, velocity, and temperature) based on this approach show reasonable agreement with our experimental data. These calculations were used to develop a fundamentally new source configuration which could substantially improve the beam parameters.

The main conclusion to be drawn from these investigations is that the agreement between the experimentally measured and calculated parameters of flows formed by nozzles of various configurations is quite satisfactory for practical purposes under conditions typical of gasdynamic molecular beam sources.

This method is now being actively used for numerical simulations to optimize the source in the molecular beam generator at the St. Petersburg Institute of Nuclear Research. Optimization of the shaper geometry is aimed at reducing the total consumption of carrier gas, increasing the Mach number attainable on the axis, and reducing the beam temperature.

This work was carried out in preparation for an experiment to search for loss of T-invariance effects in molecules, supported by Grant No. 97-02-16908 from the Russian Fund for Fundamental Research.

[1] O. M. Belotserkovskiĭ and Yu. M. Davydov, *Particle-in-Cell Method in Gasdynamics* [in Russian], Nauka, Moscow (1982), 392 pp.
[2] H. Ashkenas and F. S. Sherman, in *Rarefied Gas Dynamics IV*, edited by J. H. de Leeuw (Academic Press, New York (1966), pp. 84–105.
[3] J. B. Anderson, in *Molecular Beams and Low Density Gasdynamics*, edited by P. P. Wegener (New York, 1974), pp. 1–91.
[4] V. F. Ezhov, M. N. Groshev *et al.*, Preprint No. PIYaF-2179 [in Russian], St. Petersburg Institute of Nuclear Physics, Gatchina (1997).
[5] V. V. Yashchuk, V. F. Ezhov, G. B. Krygin, and V. L. Ryabov, Pis'ma Zh. Tekh. Fiz. **23**(20), 47 (1997) [Tech. Phys. Lett. **23**, 795 (1997)].

Translated by R. M. Durham

Influence of cobalt ions on magnetoelastic interaction in polycrystalline partially substituted yttrium iron garnets

V. M. Sarnatskiĭ, T. S. Kasatkina, and A. M. Ulyashev

Physics Research Institute, St. Petersburg State University, Petrodvorets
(Submitted January 15, 1998)
Pis'ma Zh. Tekh. Fiz. **24**, 73–78 (August 26, 1998)

An appreciable increase in the dynamic magnetostriction was observed in polycrystalline partially aluminum-substituted yttrium iron garnets with small quantities (up to 0.01 mol.%) of implanted divalent cobalt ions. The nonmonotonic behavior of the concentration dependence of the magnetoelastic interaction as a function of the cobalt ion content is explained with allowance for changes in the anisotropy fields and the profile of the magnetization curve in doped samples. [S1063-7850(98)03008-0]

Investigations of the influence of various types of impurities and defects on the physical properties of ferromagnetic substances are of considerable fundamental interest to identify the mechanisms responsible for the interaction between the lattice vibrations and the domain structure and its impairment when impurities are introduced. They are also of interest for practical applications to develop magnetic elements with predefined characteristics. In Refs. 1 and 2 we studied the influence of nonmagnetic aluminum ions on the magnetoelastic interaction which is observed as changes in the elastic moduli and ultrasound damping factor and also show up in the dynamic magnetostriction of polycrystalline yttrium iron garnets (YIG). The observed changes in the magnetoelastic characteristics of YIG ($\sim$10% increase in the ultrasound velocity, $\sim$50% decrease in the damping factor, and 30% variation in the dynamic magnetostriction) were achieved at fairly high concentrations of aluminum impurity ions, $\sim$1.5 mol.%.

It is of considerable interest to find those impurities which, when introduced in small quantities, would substantially alter the magnetic, acoustic, and magnetoelastic properties. An analysis of the electronic structure of various ions shows that such impurities may include divalent cobalt ions for which the spin–orbit interaction mechanism plays a decisive role in the formation of the magnetoelastic coupling because of the incomplete freezing of the orbital moment.[3] The authors of Refs. 4–6 reported results of theoretical calculations of the changes in the magnetostriction constants and the coefficient of magnetic anisotropy of YIG when cobalt ions were introduced in various valence states. These studies suggest that divalent cobalt ions make a considerable contribution to the formation of the magnetoelastic coupling compared with trivalent and tetravalent cobalt and this contribution is also determined by the position of the cobalt ions in the YIG lattice.

Here we present results of experimental investigations of the magnetoelastic interaction in partially substituted yttrium aluminum iron garnets with cobalt impurities. In order to maintain electrical neutrality and also to achieve divalent cobalt ions, germanium ions were also implanted in the samples, which were prepared using conventional ceramic technology and had the composition $Y_3Fe_{4.7-x}A_{0.3}Co_{x/2}Ge_{x/2}O_{12}$, where x varied between 0.005 and 0.1 mol.%. The cobalt ion content was monitored using the magnetic anisotropy constant, which is known[6,7] to depend linearly on cobalt ion content, passing through zero at a concentration of 0.008 mol.% near room temperature. The magnetoelastic interaction was estimated from the change in the ultrasound damping in a magnetic field and from the dynamic magnetostriction which was studied by a method developed by us using the amplitude of the ultrasound pulsed excited by a ferrite powder sample placed in combined variable and static magnetic fields.[8] The measurements were made at ultrasound frequencies of 5–50 MHz at temperatures between room temperature and liquid-nitrogen temperature. The external magnetic field varied between 0 and 1000 Oe.

Figure 1 gives the amplitude of the excited ultrasound A as a function of the magnetic field in four samples of aluminum yttrium iron garnet containing 0.000, 0.005, 0.012, and 0.1 mol.% divalent cobalt ions, respectively. The behavior of A as a function of the magnetic field is consistent with the dependence we studied earlier in undoped polycrystalline yttrium ion garnets.[8] An appreciable increase in the dynamic magnetostriction constant with increasing cobalt ion content is observed at low concentrations (up to 0.01 mol.%), whereas in the sample with the highest cobalt ion content, this constant is lower than that in the undoped sample. It should also be noted that as the cobalt ion content increases, the magnetic field in which maximum A is observed increases.

These results show good agreement with the theoretical calculations made by Slonzewski[4] who predicted a linear increase in the coefficient of static magnetostriction and the magnetic anisotropy at low cobalt ion concentrations. The value of A observed for the sample with a cobalt ion concentration of 0.1 mol.% may be lower because A is proportional to the dynamic magnetostriction, which in turn is determined

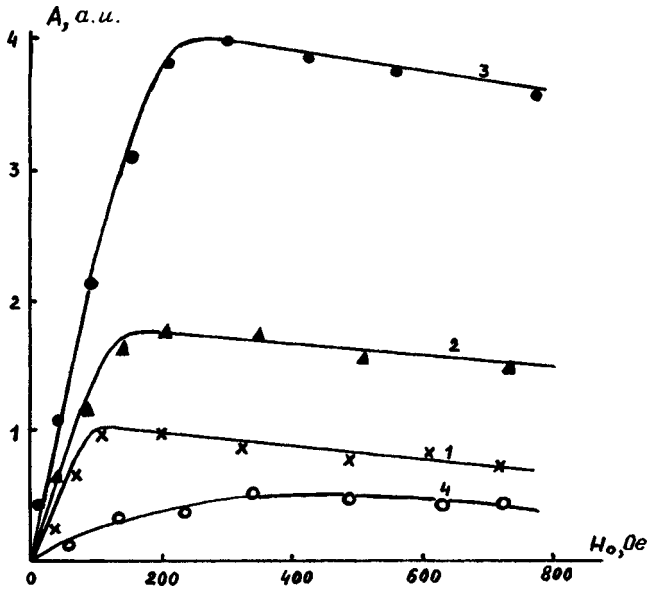

FIG. 1. Amplitude A of ultrasound excited by yttrium aluminum iron garnets as a function of the magnetic field: *1* — undoped sample, *2* — sample containing 0.005 mol.% Co, *3* — sample containing 0.012 mol.% Co, and *4* — sample containing 0.1 mol.% Co.

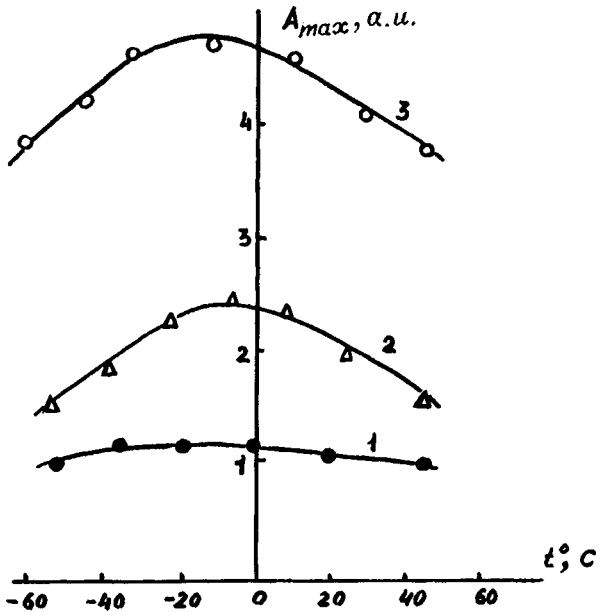

FIG. 2. Temperature dependence of the maximum ultrasound amplitude A_{max} excited by yttrium aluminum iron garnets: *1* — undoped sample, *2* — sample containing 0.005 mol.% Co, and *3* — sample containing 0.012 mol.% Co.

by the derivative of the static magnetostriction with respect to the magnetic field.

On the basis of the experimental studies[6,9] we calculated the changes in the anisotropy field and thus the form of the magnetization curve caused by the impurity ions. For the sample having the highest cobalt ion content the magnetization curve becomes appreciably broader (which reduces the dynamic magnetostriction) and shifts toward higher magnetic fields compared with the undoped sample. The calculated maxima of the derivative of the magnetization curve with respect to the magnetic field determine the fields for which maximum excited ultrasound is observed and these show good agreement with the experimentally measured values.

Figure 2 gives the temperature dependence of maximum A for samples having cobalt ion impurity concentrations of 0, 0.005, and 0.012 mol.%. It should be noted that compared with the undoped samples, the behavior of A_{max} for doped samples has a maximum with varying temperature, which shifts toward higher temperatures as the cobalt ion content increases. This behavior can be attributed to the magnetic anisotropy constant being zero in the doped samples in this temperature range,[6] i.e., a spin-reorientational phase transition induced by the impurity ions takes place. In this case, the domain motion shows appreciable fluctuations which increase the amplitude of the ultrasonic oscillations.[1]

The behavior of the damping factor of the shear ultrasonic waves as a function of the magnetic field was also investigated for these samples. The absolute values of the ultrasound damping factor and its behavior in a magnetic field depend on the relative orientation of the magnetic field and the displacement vector in the ultrasonic wave, although the most common feature in the behavior of the ultrasound damping is its dependence on the cobalt ion content, which is manifested as a decrease in the damping factor at low concentrations and an increase at the highest concentration of impurity ions. In addition, in the sample having the highest cobalt ion concentration the ultrasound damping factor does not depend on the magnetic field. This dependence of the ultrasound damping factor on the impurity ion content is caused by the anchoring of domain walls by cobalt ions at low concentrations and by appreciable changes in the domain structure at a concentration of 0.1 mol.% because the coefficient of magnetic anisotropy increases more than tenfold.[6]

These investigations have shown that acoustic methods of studying the magnetic and magnetoelastic characteristics of doped ferromagnetics are informative and can be used to develop optimum conditions (to select the operating temperature range and the cobalt ion content) for the use of yttrium aluminum iron garnets as ultrasound emitters.

[1] V. M. Sarnatskiĭ and T. V. Bakhanova, Pis'ma Zh. Tekh. Fiz. **19**(20), 51 (1994) [Tech. Phys. Lett. **19**, 788 (1994)].
[2] V. M. Sarnatskiĭ, Kh. Mirzoakhmedov, and S. Tavarov, in *Proceedings of the All-Union Acoustics Conference*, Moscow, 1991 [in Russian], pp. 230–232.
[3] K. P. Belov, *Magnetostrictive Effects and Their Technical Applications* [in Russian], Nauka, Moscow (1987), 159 pp.
[4] G. S. Slonzewski, J. Phys. Chem. Solids **15**, 335 (1960).
[5] E. Callen and H. Callen, Phys. Rev. **139**, 455 (1965).
[6] P. Hansen, W. Tolksdorf, and R. Krishnan, Phys. Rev. B **16**, 3973 (1977).
[7] G. A. Petrakovskiĭ, L. M. Protopopova, and E. M. Smokitin, Fiz. Tverd. Tela. (Leningrad) **10**, 2544 (1968) [Sov. Phys. Solid State **10**, 2005 (1968)].
[8] V. M. Sarnatskiĭ, A. A. Kuleshov, and A. A. Shono, Pis'ma Zh. Tekh. Fiz. **18**(7), 37 (1992) [Sov. Tech. Phys. Lett. **18**, 220 (1992)].
[9] M. D. Sturge, R. C. Le Craw, and J. P. Remeika, Phys. Rev. **180**, 413 (1969).

Translated by R. M. Durham

Influence of thermomagnetic treatment on the propagation velocity of magnetoelastic oscillations and the ΔE effect in disordered ferromagnetics

A. A. Gavrilyuk, N. P. Kovaleva, and A. V. Gavrilyuk

Irkutsk State University
(Submitted January 9, 1998)
Pis'ma Zh. Tekh. Fiz. **24**, 79–83 (August 26, 1998)

An investigation was made of the propagation velocity of magnetoelastic oscillations and the ΔE effect as a function of the magnetic annealing temperature and the external magnetic field in iron-based amorphous metal alloys. It is shown that this dependence is nonmonotonic. The extreme values of the propagation velocity of the magnetoelastic oscillations and the ΔE effect only coincide in a specific range of annealing temperatures. As the annealing temperature increases, the extreme values of the magnetoelastic characteristics shift toward larger magnetic fields. [S1063-7850(98)03108-5]

Annealing in a magnetic field is used to improve the magnetoelastic characteristics of iron-based amorphous metal alloys. The aim of the present study is to investigate the influence of the annealing temperature on the propagation velocity V of the magnetoelastic oscillations and the magnitude of the ΔE effect ($\Delta E/E_0=(E_0-E_H)/E_0$, where E_0 is the elastic modulus of the sample in the demagnetized state and E_H is the elastic modulus in the magnetic field) in the amorphous metal alloy $Fe_{81.5}-B_{13.5}-Si_3-Cr_2$ (the Russian analog of Metglas 2605 SC) (Refs. 1 and 2).

Samples in the form of narrow strips measuring $0.05\times0.002\times3\cdot10^{-5}$ m were annealed for 20 min at temperatures between 330 and 440 °C in a magnetic field of 160 kA/m applied transversely to the sample length. The purpose of the annealing was to remove internal stresses formed during the fabrication of the alloys and also to produce a periodic domain structure with the axis of easy magnetization oriented perpendicular to the sample length. The rearrangement of the domain structure under the influence of a magnetic field directed along the sample length should involve uniform rotation of the magnetization. The propagation velocity of the magnetoelastic oscillations and the magnitude of the ΔE effect were varied by a resonance–antiresonance method.[3] A static magnetic field and a weak, varying magnetic field (1 A/m) required to excite magnetoelastic oscillations were applied along the length of the samples.

Figures 1 and 2 give the experimental dependence of the propagation velocity of the magnetoelastic oscillations and the ΔE effect on the external magnetic field for samples annealed at temperatures between 330 and 440 °C. An analysis of these results yields the following conclusions:

1. At all annealing temperatures the dependence $V(H)$ has a characteristic minimum (Fig. 1).

2. At annealing temperatures between 370 and 430 °C the minimum propagation velocity of the magnetoelastic oscillations and the maximum ΔE effect are obtained for the same external magnetic field.

3. At annealing temperatures between 330 and 360 °C no agreement was observed between the fields corresponding to the maximum ΔE effect and the minimum propagation velocity of the magnetoelastic oscillations. Annealing at 440 °C also results in a difference between the fields corresponding to the extreme values of V and the ΔE effect.

4. As the annealing temperature increases, the minimum of V and the maximum of the ΔE effect shift toward larger magnetic fields.

5. The inset to Fig. 1 gives the propagation velocity of the magnetoelastic oscillations as a function of the sample annealing temperature in a magnetic field $H=80$ A/m. Similar curves are also obtained for other values of the applied magnetic field H. It can be seen from this graph that the value of V has a minimum at an annealing temperature of 400 °C.

These results may be explained as follows.

At fairly low annealing temperatures the domain structure of the samples is inhomogeneous because of the presence of internal stresses.[4,5] Thus, the rearrangement of the domain structure is a complex combined process involving rotation of the magnetization and displacement of the domain walls. The displacement of non-180° domain walls has a different influence on the ΔE effect and the propagation velocity of the magnetoelastic oscillations. Thus, the field corresponding to the maximum ΔE effect differs from that corresponding to minimum V. As the annealing temperature increases and the internal stresses relax, the domain structure becomes more homogeneous. In this case, the dominant rearrangement process involves the uniform rotation of the magnetization. Thus, the field corresponding to the maximum ΔE effect coincides with the field corresponding to the minimum propagation velocity of the magnetoelastic oscillations. At higher annealing temperatures the amorphous metal alloy begins to crystallize, giving rise to internal stresses in the sample. This should result in a difference between the fields corresponding to the extrema of the ΔE effect and the propagation velocity of the oscillations, as is observed experimentally.

It was shown in Ref. 6 that the minimum of the elastic

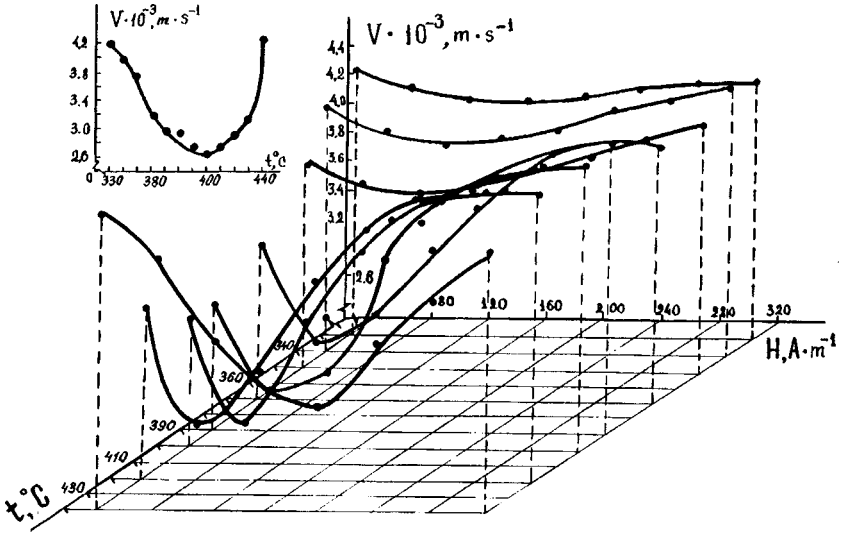

FIG. 1. Propagation velocity of magnetoelastic oscillations as a function of the external magnetic field at various annealing temperatures.

modulus in a magnetic field and the maximum of the ΔE effect in alloys with a band domain structure are determined by the field at which the domain wall structure undergoes a Bloch–Néel transition. As the magnetic annealing temperature increases, the induced anisotropy field increases, increasing the field at which the domain wall structure changes and this has the result that the minima of the elastic moduli, the propagation velocity of the magnetoelastic waves, and also the maximum of the ΔE effect are shifted toward larger fields.

The propagation velocity of the magnetoelastic oscillations in the magnetic field $H=80$ A/m at temperatures between 330 and 400 °C decreases with increasing annealing temperature because of the reduced anisotropy caused by the internal stresses. As a result of the incipient crystallization of the amorphous material at 400 °C and with further increase in the annealing temperature, the anisotropy field increases; under these conditions the increase is caused by atomic ordering.

From Ref. 7, the expression for the elastic modulus in the magnetic field E_H may be expressed as a function of the anisotropy constant K in the form

$$E_H=E_0[2K-3\lambda_s\sigma]^3/\{[2K-3\lambda_s\sigma]^3+9\lambda_s^2M_s^2H^2E_0\}, \tag{1}$$

where λ_s is the saturation magnetostriction, M_s is the saturation magnetization, σ are the external elastic stresses, and E_0 is the elastic modulus in the absence of a magnetic field. Assuming that the relation between the propagation velocity of the magnetoelastic oscillations and the elastic modulus can be written as

$$V=(E_H/\rho)^{1/2}, \tag{2}$$

where ρ is the density of the sample, we obtain the following expression for the propagation velocity of the magnetoelastic oscillations:

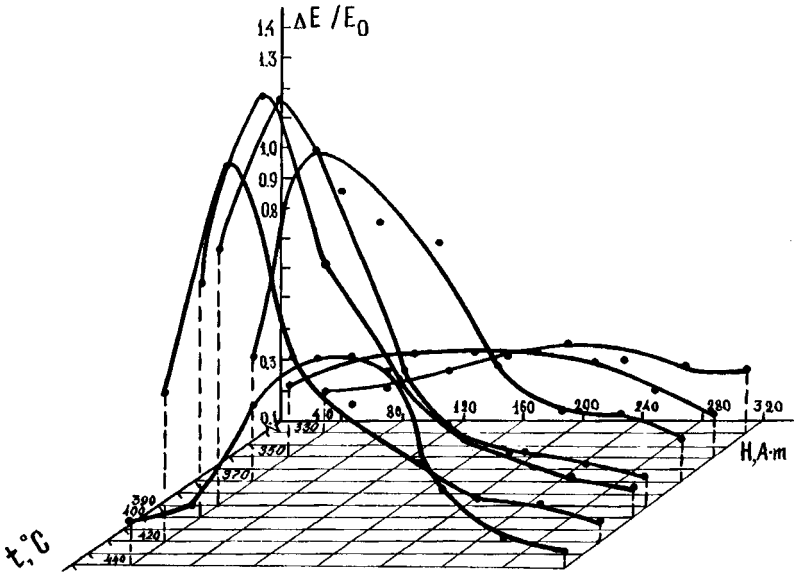

FIG. 2. Dependence of the ΔE effect on the external magnetic field at various annealing temperatures.

$$V=\{(E_0/\rho)[2K-3\lambda_s\sigma]^3/([2K-3\lambda_s\sigma]^3 + 9\lambda_s^2 M_s^2 H^2 E_0)\}^{1/2}. \quad (3)$$

Thus, the propagation velocity of the magnetoelastic oscillations increases as the anisotropy constant increases.

[1] M. L. Spano, K. B. Hathaway, and H. T. Savage, J. Appl. Phys. **53**, 2667 (1982).
[2] J. B. Restorff, M. Wun-Fogle, K. B. Hathaway, and A. E. Clark, J. Appl. Phys. **69**, 4668 (1991).
[3] T. O'Dell, Phys. Solid State **74**, 2667 (1982).
[4] J. D. Livingston, Phys. Solid State **56**, 637 (1979).
[5] W. Fernengel, Phys. Solid State **64**, 538 (1981).
[6] A. L. Petrov, A. A. Gavrilyuk, and S. M. Zubritskiĭ, Fiz. Met. Metalloved. **80**(6), 47 (1995).
[7] J. D. Livingston, Phys. Solid State **70**, 591 (1982).

Translated by R. M. Durham

Modulation of the polarization of semiconductor laser radiation at constant output power

G. S. Sokolovskiĭ, A. G. Deryagin, and V. I. Kuchinskiĭ

A. F. Ioffe Physicotechnical Institute, Russian Academy of Sciences, St. Petersburg
(Submitted February 25, 1998)
Pis'ma Zh. Tekh. Fiz. **24**, 84–90 (August 26, 1998)

The degree of polarization of ''doubly''-modulated (by the pump current and the optical confinement factor) laser radiation is analyzed by applying a method of analyzing the stability of the solutions of systems of Lyapunov differential equations to a system of rate equations. An analysis of the system of rate equations yielded its eigenvalues, also called stability coefficients, which are the characteristic time for a transition of the system from one state to another. The behavior of a doubly modulated laser was modeled mathematically and it was demonstrated that the polarization of the laser output radiation can be controlled with almost constant output power. © *1998 American Institute of Physics.* [S1063-7850(98)03208-X]

The switching, coexistence, and bistability of the TE/TM polarizations of strained-layer semiconductor laser radiation was observed in Refs. 1–4. A phenomenological model to explain the polarization switching effect and polarization bistability was developed in Refs. 5 and 6. Then, in Ref. 7 we derived analytic expressions for the polarization switching time for semiconductor laser radiation which can be used to estimate the influence of the laser diode parameters on the polarization of the output radiation.

Modulation of the polarization state of the radiation in fiber-optic communication lines (FOCLs) suppresses the anisotropic saturation of the gain (polarization hole burning) in erbium fiber-optic amplifiers, which can cause appreciable deterioration of the optical signal-to-noise ratio in extralong-range FOCLs with optical regeneration of the transmitted signal.[8] Modern FOCLs use expensive high-speed polarization scramblers to depolarize the optical signal. Thus, semiconductor lasers with depolarized radiation are very promising radiation sources for FOCLs because they can easily be integrated with optical modulators in a single compact monolithic device.

Here we examine the possibility of double modulation (by the pump current and by the optical confinement factor) of a semiconductor laser to directly control the polarization and in particular, to obtained depolarized laser radiation.

The basic idea of double modulation is as follows. The watt–ampere characteristic of a laser with polarization-switched output radiation has a region where the degree of polarization and the output power depend linearly on the pump current.[7] The position of the polarization switching region on the watt–ampere characteristic depends in particular on the optical confinement factor. Thus, by modulating the optical confinement factor, it is possible to alter the degree of polarization and by modulating the pump current, it is possible to keep the output power constant.

The optical confinement factor can be modulated by applying voltage to additional side contacts on the laser diode deposited on each side of the stripe.[9]

The system of rate equations[7] allowing for the optical confinement factor $\Gamma_{\mathrm{TE/TM}}$ of the TE/TM modes has the form

$$\begin{cases} \dfrac{dN}{dt} = \dfrac{1}{qV} - g_{\mathrm{TE}}(N-N_{\mathrm{TE}})(1-\varepsilon_{\mathrm{EE}}S_{\mathrm{TE}}-\varepsilon_{\mathrm{EM}}S_{\mathrm{TM}})S_{\mathrm{TE}} \\ \qquad - g_{\mathrm{TM}}(N-N_{\mathrm{TM}})(1-\varepsilon_{\mathrm{ME}}S_{\mathrm{TE}}-\varepsilon_{\mathrm{MM}}S_{\mathrm{TM}})S_{\mathrm{TM}} - \dfrac{N}{\tau}, \\ \dfrac{dS_{\mathrm{TE}}}{dt} = \Gamma_{\mathrm{TE}} g_{\mathrm{TE}}(N-N_{\mathrm{TE}})(1-\varepsilon_{\mathrm{EE}}S_{\mathrm{TE}}-\varepsilon_{\mathrm{EM}}S_{\mathrm{TM}})S_{\mathrm{TE}} \\ \qquad + \Gamma_{\mathrm{TE}}\beta\dfrac{N}{\tau} - \dfrac{S_{\mathrm{TE}}}{\tau_{\mathrm{TE}}}, \\ \dfrac{dS_{\mathrm{TM}}}{dt} = \Gamma_{\mathrm{TM}} g_{\mathrm{TM}}(N-N_{\mathrm{TM}})(1-\varepsilon_{\mathrm{ME}}S_{\mathrm{TE}}-\varepsilon_{\mathrm{MM}}S_{\mathrm{TM}})S_{\mathrm{TM}} \\ \qquad + \Gamma_{\mathrm{TM}}\beta\dfrac{N}{\tau} - \dfrac{S_{\mathrm{TM}}}{\tau_{\mathrm{TM}}}, \end{cases} \tag{1}$$

where N is the carrier concentration, $S_{\mathrm{TE/TM}}$ is the density of TE/TM polarized photons, $g_{\mathrm{TE/TM}}$ is the linear gain for the TE/TM-polarized light, $\tau_{\mathrm{TE/TM}}$ is the lifetime of the TE/TM-polarized photons, $N_{\mathrm{TE/TM}}$ is the transparency concentration for the TE/TM-polarized light, τ is the carrier lifetime, ε_{ij} are the nonlinear gains, β is the coefficient of spontaneous emission, q is the elementary charge, and V is the volume of the active region.

Systems of rate equations are usually analyzed by numerical integration, which unfortunately cannot provide an explicit description of the dynamics of the polarization switching process for heterolaser radiation. In Ref. 7, however, we suggested that a method[10] of analyzing the stability of systems of Lyapunov differential equations could be applied to a system of rate equations. As a result of analyzing the stability of the system of rate equations, we obtained its

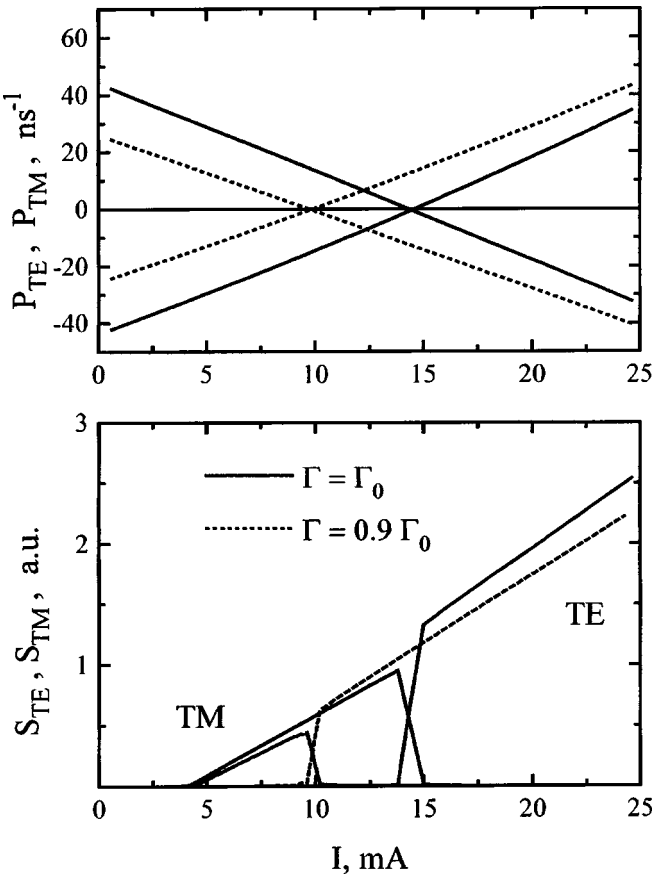

FIG. 1. Watt–ampere characteristics and stability coefficients for various optical confinement factors for a laser having the following parameters: $g_{TE}=1.45\times10^{-6}$ cm^3/s, $g_{TM}=1.40\times10^{-6}$ cm^3/s, $\tau_{TE}=2.0$ ps, $\tau_{TM}=1.6$ ps, $N_{TE}=4.5\times10^{17}$ cm^{-3}, $N_{TM}=3.29\times10^{17}$ cm^{-3}, $\tau=3$ ns, $\varepsilon_{EM}=2.0\times10^{-17}$ cm^3, $\varepsilon_{EE}=1.0\times10^{-17}$cm^3, $\varepsilon_{ME}=4.5\times10^{-17}$ cm^3, and $\varepsilon_{MM}=6.0\times10^{-17}$ cm^3.

eigenvalues which are the characteristic time taken for transition of the system from one state to the other.

The stability of the system (1) was analyzed using the approximation of a constant carrier concentration, $dN/dt=0$. Using this condition, we can perform the very convenient transformation:

$$\begin{cases} \dfrac{dS_{TE}}{dt}=\Gamma_{TE}g_{TE}\tau\left(\dfrac{1}{qV}-\dfrac{S_{TE}}{\Gamma_{TE}\tau_{TE}}-\dfrac{S_{TM}}{\Gamma_{TM}\tau_{TM}}-\dfrac{N_{TE}}{\tau}\right) \\ \qquad\times(1-\varepsilon_{EE}S_{TE}-\varepsilon_{EM}S_{TM})S_{TE}-\dfrac{S_{TE}}{\tau_{TE}}, \\ \dfrac{dS_{TM}}{dt}=\Gamma_{TM}g_{TM}\tau\left(\dfrac{1}{qV}-\dfrac{S_{TE}}{\Gamma_{TE}\tau_{TM}}-\dfrac{S_{TM}}{\Gamma_{TM}\tau_{TM}}-\dfrac{N_{NM}}{\tau}\right) \\ \qquad\times(1-\varepsilon_{ME}S_{TE}-\varepsilon_{MM}S_{TM})S_{TM}-\dfrac{S_{TM}}{\tau_{TM}}. \end{cases} \tag{2}$$

After linearizing the modified system of rate equations (2), we obtain its eigenvalues which, according to Ref. 10, are also called the (in)stability coefficients:

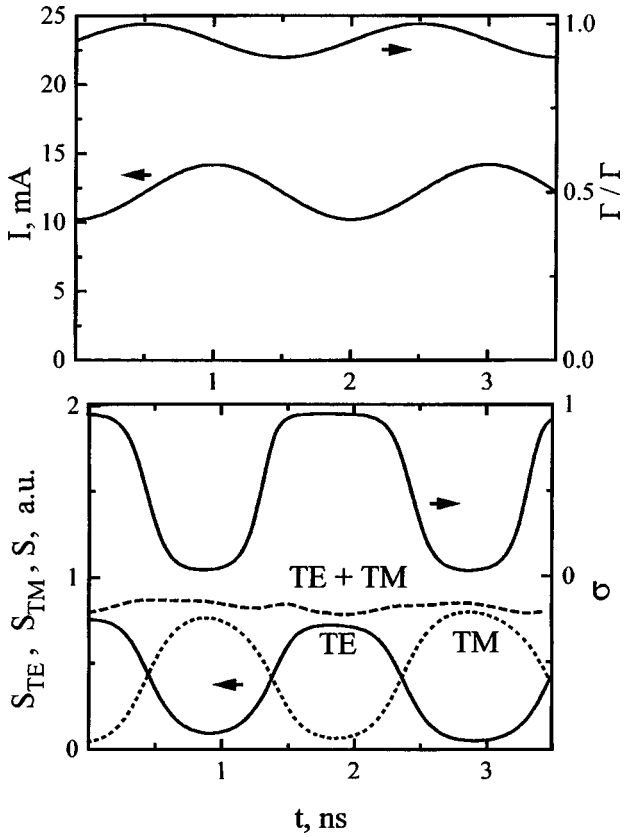

FIG. 2. Degree of polarization $\sigma=S_{TE}/(S_{TE}+S_{TM})$ and density of Te/TM-polarized photons $S_{TE/TM}$ as a function of time with double modulation.

$$P_{TE/TM}=\Gamma_{TE/TM}g_{TE/TM}\tau\left(\frac{1}{qV}-\frac{s_{TM/TE}}{\Gamma_{TM/TE}\tau_{TM/TE}}-\frac{N_{TE/TM}}{\tau}\right)\times(1-\varepsilon_{EM/ME}s_{TM/TE})-\frac{1}{\tau_{TE/TM}}, \tag{3}$$

where $s_{TE/TM}$ is the density of TE/TM-polarized photons in the absence of light of the opposite polarization:

$$s_{TE/TM}=\frac{1}{2}\left(\frac{1}{\varepsilon_{EE/MM}}+\Gamma_{TE/TM}\tau_{TE/TM}\left(\frac{1}{qV}-\frac{N_{TE/TM}}{\tau}\right)\right) - \sqrt{\frac{1}{4}\left(\frac{1}{\varepsilon_{EE/MM}}+\Gamma_{TE/TM}\tau_{TE/TM}\left(\frac{1}{qV}-\frac{N_{TE/TM}}{\tau}\right)\right)^2 - \frac{\Gamma_{TE/TM}\tau_{TE/TM}}{\varepsilon_{EE/MM}}\left(\frac{1}{qV}-\frac{N_{TE/TM}}{\tau}-\frac{1}{\Gamma_{TE/TM}s_{TE/TM}\tau_{TE/TM}\tau}\right)}. \tag{4}$$

It was shown in Ref. 7 that three combinations of stability coefficients $P_{TE/TM}$ are possible: both coefficients are positive—TE and TM modes coexist; both coefficients are negative—state of bistability; and lastly, the stability coefficients have different signs—the laser emits radiation of that particular polarization for which the eigenvalue is negative.

Figure 1 gives the watt–ampere characteristics of a laser for the TE- and TM-polarized emission plotted for two different values of the optical confinement factor Γ. It can be seen that changes in the optical confinement factors $\Gamma_{TE/TM}$ can alter the position of the polarization switching point on the laser watt–ampere characteristic (Fig. 1). For the laser

parameters used in the simulation, a 10% change in the optical confinement factor can alter the polarization switching current almost by a factor of 1.5. However, a change in the optical confinement also leads to changes in the laser external differential efficiency, i.e., variation of the output power for the same pump current. Thus, by modulating the optical confinement factor and keeping the output power constant by suitably varying the pump current, we can continuously tune the degree of polarization of the laser radiation (Fig. 2). The relaxation oscillations observed as a result of changes in the optical confinement factor, can be almost completely eliminated by a phase shift of the pump current modulation relative to the phase of the $\Gamma_{\mathrm{TE/TM}}$ modulation.[9]

Using Eq. (2), to simplify the calculations of the modulation amplitude of $\Gamma_{\mathrm{Te/TM}}$, we can also determine the polarization switching I_{sw}, i.e., the pump current corresponding to the unpolarized laser output radiation. Its accurate value can be calculated if in Eq. (2) we assume $S_{\mathrm{TE}}=S_{\mathrm{TM}}=S_{\mathrm{sw}}$, $dS_{\mathrm{TE}}/dt=dS_{\mathrm{TM}}/dt=0$:

$$I_m=\frac{I}{\Gamma_{\mathrm{TE}}g_{\mathrm{TE}}\tau_{\mathrm{TE}}\tau(1-\varepsilon_{\mathrm{E}}S_{\mathrm{sw}})}+\left(\frac{1}{\tau_{\mathrm{TE}}}+\frac{1}{\tau_{\mathrm{TM}}}\right)S_{\mathrm{sw}}+\frac{N_{\mathrm{TE}}}{\tau},$$

$$S_{\mathrm{sw}}=B-\sqrt{B^2-C},$$

$$B=\frac{1}{2}\left(\frac{1}{\varepsilon_{\mathrm{E}}}+\frac{1}{\varepsilon_{\mathrm{M}}}+\frac{1}{\Gamma_{\mathrm{TE}}g_{\mathrm{TE}}\tau_{\mathrm{TE}}\varepsilon_{\mathrm{E}}\Delta N}-\frac{1}{\Gamma_{\mathrm{TM}}g_{\mathrm{TM}}\tau_{\mathrm{TM}}\varepsilon_{\mathrm{M}}\Delta N}\right),$$

$$C=\frac{1}{\varepsilon_{\mathrm{E}}\varepsilon_{\mathrm{M}}}\left(1+\left(\frac{1}{\Gamma_{\mathrm{TE}}g_{\mathrm{TE}}\tau_{\mathrm{TE}}}-\frac{1}{\Gamma_{\mathrm{TM}}g_{\mathrm{TM}}\tau_{\mathrm{TM}}}\right)\Delta N\right), \qquad (5)$$

$$\varepsilon_{\mathrm{E}}=\varepsilon_{\mathrm{EE}}+\varepsilon_{\mathrm{EM}}, \quad \varepsilon_{\mathrm{M}}=\varepsilon_{\mathrm{MM}}+\varepsilon_{\mathrm{ME}},$$

$$\Delta N=N_{\mathrm{TE}}-N_{\mathrm{NM}}.$$

The polarization switching region for modulation of $\Gamma_{\mathrm{TE/TM}}$ is limited by the switching currents at maximum and minimum Γ. Note that the existence of hysteresis on the laser watt–ampere characteristic[7] can substantially reduce the polarization switching region determined from Ref. 5.

To sum up, we have examined the possibility of double modulation (by the pump current and the optical confinement factor) of a semiconductor laser to control the polarization of the laser radiation. The behavior of a doubly modulated laser was modeled numerically, and this showed that the polarization of the laser output radiation can be controlled with almost constant output power.

In conclusion, the authors are grateful to F. N. Timofeev for fruitful discussions which provided the stimulus for this work.

This work was supported financially by the Russian Fund for Fundamental Research (Project No. 96-02-17864a).

[1] D. Akhmedov, N. P. Bezhan, N. A. Bert, S. G. Konnikov, V. I. Kuchinskiĭ, V. A. Mishurnyĭ, and E. L. Portnoĭ, Pis'ma Zh. Tekh. Fiz. **6**, 705 (1980) [Sov. Tech. Phys. Lett. **6**, 304 (1980)].
[2] V. A. Elyukhin, V. R. Kocharyan, E. L. Portnoĭ, and B. S. Ryvkin, Pis'ma Zh. Tekh. Fiz. **6**, 712 (1980) [Sov. Tech. Phys. Lett. **6**, 307 (1980)].
[3] K. G. Kalandarishvili, S. Yu. Karpov, V. I. Kuchinskiĭ, M. N. Mizerov, E. L. Portnoĭ, and V. B. Smirnitskiĭ, Zh. Tekh. Fiz. **53**, 1560 (1983) [Sov. Phys. Tech. Phys. **28**, 959 (1983)].
[4] A. G. Deryagin, D. V. Kuksenkov, V. I. Kuchinskii, E. L. Portnoi, and V. B. Smirnitskii, IEE Proc.: Optoelectron. **142**, 51 (1995).
[5] Y. C. Chen and J. M. Liu, Opt. Quantum Electron. **19**, S93 (1987).
[6] G. Ropas, A. Le Floch, G. Jezequel, R. Le Naour, Y. C. Chen, and J. M. Liu, Int. J. Quantum Chem. **QE-23**, 1027 (1987).
[7] G. S. Sokolovskiĭ, A. G. Deryagin, and V. I. Kuchinskiĭ, Pis'ma Zh. Tekh. Fiz. **23**(9), 87 (1997) [Tech. Phys. Lett. **23**, 373 (1997)].
[8] M. G. Taylor, IEEE Photonics Technol. Lett. **5**, 1244 (1993).
[9] S. A. Gurevich, M. S. Shatalov, and G. S. Simin, Int. J. High-Speed Electron. Systems **8**, 547 (1997).
[10] A. M. Lyapunov, *The General Problem of the Stability of Motion*, Taylor & Francis, London (1992); Russ. orig. Gostekhizdat, Moscow (1950).

Translated by R. M. Durham

Silicon switching structures with fluorides of rare-earth elements

V. A. Rozhkov and M. B. Shalimova

Samara State University
(Submitted March 6, 1998)
Pis'ma Zh. Tekh. Fiz. **24**, 91–95 (August 26, 1998)

Results are presented of an investigation of the photoelectric characteristics of silicon metal–insulator–metal switching structures with a thin-film insulating layer of rare-earth fluoride. Studies of the steady-state and kinetic characteristics of the photocurrent revealed that in the low-resistivity state the metal–tunnel insulator–semiconductor model can be applied to the structures. © *1998 American Institute of Physics.* [S1063-7850(98)03308-4]

The fundamental laws governing the electrical switching of conductance with memory, observed in film structures with fluorides of rare-earth elements, were described in Refs. 1–3. Characteristic features of this effect are the high rate of change of the resistivity in the high- and low-resistivity states (10^6–10^7), short switching times (fractions of a microsecond), and low switching energy ($\sim 10^{-8}$ J). Investigations[2,3] have shown that in the low-resistivity state a channel of radius between 1 and 5 μm forms in the insulator film, possessing enhanced electrical conductivity and a positive temperature coefficient of resistance, characteristic of the metal phase. Here we describe the photoelectric properties of silicon metal–insulator–semiconductor (MIS) switching structures with fluorides of rare-earth elements.

Insulating films of cerium, dysprosium, and erbium fluorides were prepared by thermal deposition of powdered fluorides of rare-earth elements in vacuum. The substrates for the MIS structures were n- or p-type single-crystal silicon wafers of the type KÉF-5(111) or KDB-4,5(100), respectively. The photoelectric characteristics of the silicon MIS structures with rare-earth fluorides were investigated under cw illumination and when the structures were exposed to monochromatic radiation pulses of different duration. For the measurements we used structures with upper aluminum contacts of area $A = 2.45 \times 10^{-3}$ cm^2. The intensity of the incident radiation was between $I = 4.8 \times 10^{15}$ and 4.8×10^{18} quanta/(cm$^2 \cdot$ s) at $\lambda = 0.63$ μm. The source of pulsed monochromatic radiation at $\lambda = 0.93$ μm was an AL 106A gallium arsenide light-emitting diode.

It has been established that the current–voltage characteristics of MIS structures in the high-resistivity state are almost symmetric and are described by the Poole–Frenkel mechanism. After switching to the low-resistivity state, the current–voltage characteristics of MIS structures are unipolar with a rectification factor of 10–10^4. An analysis shows that the unipolarity of the current–voltage characteristics of structures in the low-resistivity state is attributable to the properties of the interface between the low-resistivity conduction channel and the semiconductor. The spread of values of the forward and reverse currents and the rectification factor observed for different samples can be explained by the presence of a layer of tunnel-thin insulator at the interface with the semiconductor. This layer is formed in the small-radius conduction channel after the MIS structures have been switched to the low-resistivity state. Its thickness is estimated to be 10–40 Å.

The investigations showed that the photoelectric characteristics of MIS structures change appreciably after switching to the low-resistivity state. It was established that in the high-resistivity state when the leakage current through the insulator is small, the steady-state photocurrent flowing through the MIS structure is also negligible. In this particular case, the kinetics of the photoresponse of MIS structures is alternating and is characterized by purely capacitive initial and final current surges.

After the MIS structures have switched to the low-resistivity state, their photoelectric characteristics change appreciably and become similar to the behavior typical of metal–tunnel-thin insulator–semiconductor (MTIS) structures. Figure 1 gives the reverse branches of the current–voltage characteristics of Al–CeF_3–Si MIS structures in the low-resistivity state, measured with a low load resistance under cw illumination. It can be seen that in the initial section $V < V^{cr}$ the measured photocurrent is negligible and is limited by the leakage current through the insulator. For $V > V^{cr}$ the photocurrent saturates and the applied voltage is

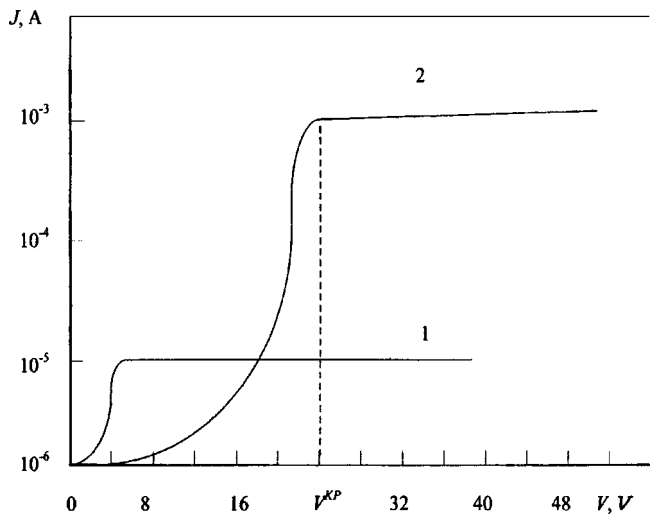

FIG. 1.

incident on the space charge region. Estimates show that changes in V^{cr} are mainly caused by variation of the voltage drop at the insulator, which was $V_d \approx 1.5-12.2$ V.

Thus, under the experimental conditions a situation is achieved where an appreciable fraction of the voltage applied to the MTIS structure enters the insulator and photocurrent amplification may occur. This case is typified by an increase in the current of majority carriers tunneling from the metal to the semiconductor as the reverse bias of the illumination intensity increases. The majority carrier photocurrent becomes comparable with or greater than the current of minority carriers, which implies amplification.[4,5]

The kinetic characteristics of the photocurrent in the low-resistivity state with a reverse bias $V=-32$ V applied to the structure are accurately approximated by a hyperbolic dependence of the following type:

$$j_p(t)=I^*M_p\begin{cases}1-\dfrac{1}{\left(1+\dfrac{t}{\tau_d}\right)^2}\\[2ex] \dfrac{1}{\left(1+\dfrac{t}{\tau_d}\right)^2}\end{cases}, \qquad (1)$$

where the first equation corresponds to the illumination being switched on at time $t=0$ and the second corresponds to it being switched off at $t=0$; $M_p=(J_n+J_p)/J_p$ is the photocurrent gain for structures with an n-type substrate, I^* is the flux of electron–hole pairs generated by the light per unit time, τ_d is the characteristic relaxation time, and J_n and J_p are the photocurrents of majority (electrons) and minority (holes) carriers, respectively.

An investigation of the kinetic characteristics of the photocurrent using the oscilloscope traces of the photoresponse reveals sections of capacitive current when the illumination is switched off and on. Figure 2a shows a complete trace of the photocurrent of an Al–CeF_3–pSi structure in the low-resistivity state, illuminated by a rectangular light pulse with a dc voltage $V=-32$ V applied to the structure. Figure 2b gives this characteristic for shorter pulse durations which allows the initial and final purely capacitive current surges to be examined in greater detail. This current is given by the expression $J_p(0)=qAI^*=1.3\ \mu$A and is equal to the photogeneration current of minority carriers. This current is established within a time much shorter than τ_d and is determined by the greater of either the carrier transit times through the space charge region or RC. The saturation photocurrent exceeds $J_p(0)$, which implies photocurrent amplification.[6] The maximum photocurrent gain was $M=49$ and $M_p=34$ for p- and n-type silicon structures, respectively. The tunnel transmission characteristics of the insulator layer determined from

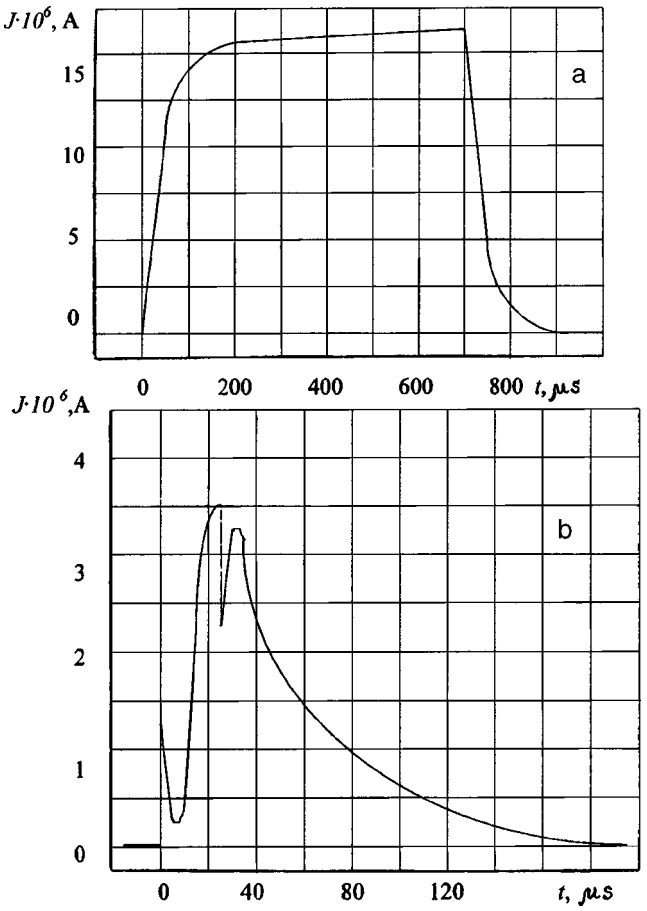

FIG. 2.

the kinetic characteristics were in the ranges $\overline{D}_n$ between 2.7×10^{-11} and 2.2×10^{-8} and $\overline{D}_p$ between 1.7×10^{-10} and 4.7×10^{-8}.

To conclude, these investigations have shown that it is promising to use silicon MIS structures with rare-earth fluorides as electrical switches and photodetectors exhibiting internal photocurrent amplification.

[1] V. A. Rozhkov and M. B. Shalimova, Pis'ma Zh. Tekh. Fiz. **18**(5), 74 (1992) [Sov. Tech. Phys. Lett. **18**, 157 (1992)].
[2] V. A. Rozhkov and M. B. Shalimova, Fiz. Tekh. Poluprovodn. **27**, 438 (1993) [Phys. Solid State **27**, 245 (1993)].
[3] V. A. Rozhkov and N. N. Romanenko, Pis'ma Zh. Tekh. Fiz. **19**(22), 6 (1993) [Tech. Phys. Lett. **19**, 704 (1993)].
[4] A. Ya. Vul', S. V. Kozyrev, and V. I. Fedorov, Fiz. Tekh. Poluprovodn. **15**, 142 (1981) [Sov. Phys. Semicond. **15**, 83 (1981)].
[5] A. Ya. Vul', V. I. Fedorov, Yu. F. Biryulin *et al.*, Fiz. Tekh. Poluprovodn. **15**, 525 (1981) [Sov. Phys. Semicond. **15**, 297 (1981)].
[6] A. Ya. Vul', A. T. Dideĭkin, Yu. S. Zinchik *et al.*, Fiz. Tekh. Poluprovodn. **17**, 1471 (1983) [Sov. Phys. Semicond. **17**, 933 (1983)].

Translated by R. M. Durham